EXPLORING NANOSCALE SPIN PHYSICS USING SINGLE SPINS IN DIAMOND

by

Kai Zhang

BS, Nanjing University, 2010

MS, University of Pittsburgh, 2012

Submitted to the Graduate Faculty of

the Dietrich School of Arts and Sciences in partial fulfillment

of the requirements for the degree of

Doctor of Philosophy

University of Pittsburgh

2018

UNIVERSITY OF PITTSBURGH

THE DIETRICH SCHOOL OF ARTS AND SCIENCES

DEPARTMENT OF PHYSICS AND ASTRONOMY

This dissertation was presented

by

Kai Zhang

It was defended on

February 9th, 2018

and approved by

Gurudev Dutt, PhD, Department of Physics and Astronomy

Jeremy Levy, PhD, Department of Physics and Astronomy

Eric Swanson, PhD, Department of Physics and Astronomy

Sunil Saxena, PhD, Department of Chemistry

Andrew Daley, PhD, Department of Physics, University of Strathclyde

Dissertation Advisor: Gurudev Dutt, PhD, Department of Physics and Astronomy

EXPLORING NANOSCALE SPIN PHYSICS USING SINGLE SPINS IN DIAMOND

Kai Zhang, PhD

University of Pittsburgh, 2018

Understanding spin physics and controlling solid-state spins at nanometer length scales is of crucial importance in modern physics research. Because of the atomic-scale dimensions, long coherence time, and optical readout, Nitrogen-Vacancy centers (NV centers) in diamond have become prominent for exploring topics in nanoscale spin physics. In this thesis, two questions are investigated using single NV centers: what mechanisms limit the control and measurement of geometric phase of a single solid-state spin qubit, and whether it is feasible to detect electron spin resonance in submicron volumes from copper-ion-labeled molecules. We have obtained limits on the fidelity of geometric phase gates, and showed using newly developed quantum sensing techniques that we are indeed able to detect such extremely weak signals, down to the single spin limit. Our results with NV centers in measuring single electron spins opens the door to a variety of applications of NV center magnetometry in interdisciplinary topics such as research on the dynamics of protein molecules with copper ion labels.

TABLE OF CONTENTS

LIST OF TABLES

LIST OF FIGURES

ACKNOWLEDGEMENT

I want to thank my advisor, Dr. Gurudev Dutt, for guiding me through my whole PhD program, starting in 2010 as my academic advisor and my research advisor a year later. He trained me and turned me from an inexperienced undergraduate student majored in physics into a competent experimentalist in condensed matter physics.

I would also like to thank my lab mates during all these years, including Nusran, Peng, Chenxu, Bradley and Jonathan, for stimulating discussion, productive teamwork and friendly supports from each other. And I want to thank all the staff in our university, especially Leyla, for taking care of most of my non-academic concerns so I can focus on my research. I give my greatest acknowledgement to University of Pittsburgh, for providing me the chance to be a PhD student here, meeting all these great people and working on my research projects with them. It is my honor to graduate from Pitt.

Last but not the least, I thank Department of Energy, National Science Foundation, Alfred P. Sloan Foundation, Charles E. Kaufman Foundation and University of Pittsburgh for financial support during my PhD life.

感谢我的父母、家人。感谢国家。

Hail to Pitt!

伟大祖国繁荣昌盛！

1.0 INTRODUCTION

This chapter introduces the Nitrogen Vacancy center, a widely used defect in diamond. The applications of this defect as a magnetic sensor used in a variety of fields are also reviewed in brief.

1.1 NITROGEN VACANCY CENTERS IN DIAMOND

Nitrogen Vacancy centers (NV centers) are point defects in diamond lattice, consisting of a substitutional nitrogen atom and an adjacent vacancy [1]. Optical detection of single NV centers and optical initialization and readout of spin states of NV centers was first reported in 1997 [2]. Since then, NV centers became one of the most popular quantum devices with a variety of potential applications in quantum information processing (QIP) [3-5], quantum optics [6-9], hybrid quantum systems [10, 11], fundamental quantum mechanics [12-14], and nanoscale measurements [15-17].

NV centers are unique atom-like quantum systems in condensed matter material. Compared to other condensed matter quantum systems, NV centers are defects in diamond, the most stable material on earth. Diamond is highly resistive to physical abrasion and chemical corrosion. The wide band gap in its electronic band structure restricts the interaction between the NV centers and the band electrons and keep the charge state stable. Diamond is an excellent insulator and an outstanding thermal conductor, capable of handling large optical and electronic power. Single NV centers in diamond hold the record for the longest coherence time measured among electronic spins in solid state at room temperature of greater than 1.8 ms [18, 19]. Compared to atomic and molecular quantum systems, NV centers are easily accessible under room temperature and stable.

Among all applications, using NV centers as a nanoscale sensor is one of the most popular, because of its ability to work at room temperature, resilience to chemicals and nontoxicity to living cells. NV centers are capable of measuring electric field [20], magnetic field [17], and local temperature [21-23] with nanoscale spatial resolution. The applications of electric field sensing and thermal sensing with NV centers have limitations due to the relatively low sensitivity. On the other hand, the magnetic field sensitivity of NV centers benefits from the long coherence time and the magnetic field sensing with NV centers is incredibly competitive among all magnetometry techniques [24, 25].

1.2 MAGNETOMETRY WITH NITROGEN-VACANCY CENTERS

Magnetic sensing and imaging in nanometer scale is of critical importance in nanoscience and nanotechnology, with a variety of potential applications to material science and biophysics [26]. The magnetic sensitivity of NV centers is dominantly limited by the photon shot noise in the optical readout [17]. The sensitivity can be expressed as:

$$\eta \propto \frac{1}{C\sqrt{\alpha_0}} \times \frac{1}{\sqrt{T_x}} \tag{1.1}$$

where C is the percentage contrast between quantum states, α_0 is the photon counts per optical measurement shot, and T_x refers to either T_2^* or T_2, depending on whether the magnetic field is DC (direct current) or AC (alternating current), respectively. The SI unit of magnetic sensitivity η is $\mathrm{T}/\sqrt{\mathrm{Hz}}$. The smaller the value of η, the better the sensitivity. After the first demonstration of magnetic field sensing with NV centers in 2008 [15], efforts have been made to improve the magnetic field sensitivity by increasing coherence time and detection efficiency, including designing increasingly better dynamical decoupling sequences [27-29], fabricating high purity diamond samples with extremely low level of spin bath [19, 30], and engineering the photon collection optics for higher efficiency [31-35].

In addition to single NV centers in high purity diamond, ensemble NV centers in high-NV-density diamond samples are being explored for magnetometry applications as well as single NV centers [36]. Despite the lower readout contrast C, the sensitivity of ensemble NV centers could be even better than single NV centers due to much higher fluorescence intensity α_0. The $N-V$

axes can lie equally among the four possible ⟨111⟩ direction of diamond lattice, which offers us the capability to measure magnetic field projection onto four directions simultaneously, or in other words, vector magnetometry [36, 37]. Ensemble NV centers in diamond nanocrystals can be implanted into living cells as a nanoscale sensor used in biophysics [38]. Although the fluorescence intensity is higher due to more NV centers as photon emitters, the gain in magnetic sensitivity is compensated by the decrease in contrast of spin readout. On the other hand, besides limitation in spatial resolution, another disadvantage of ensemble NV centers is the complexities in coherent manipulation and dynamic decoupling. To use NV centers as a qubit or a quantum sensor, single NV centers are preferred. This thesis will focus on single NV centers in diamond.

In terms of magnetic field sensitivity, NV center is not the best compared to other modern techniques in magnetometry. For example, atomic vapor magnetometers have a much higher magnetic field sensitivity on the order of $0.1\ \mathrm{fT}/\sqrt{\mathrm{Hz}}$, with the detector in macroscopic size [39, 40]. But the spatial resolution potentially in sub-nanometers that NV center can provide is the best of all. To make use of the spatial resolution of NV centers, scanning diamond probe microscope (SDPM) has been realized experimentally and magnetic imaging in nanoscale has been achieved. [41-43] However, the diamond probe fabrication process is extremely complex and difficult, which limits the future development of SDPM for "real-life" applications.

Besides magnetic imaging, magnetic sensing techniques are also used for sensing single electrons or nuclei. A comparison among different techniques in nuclear spin sensing in [25]. Atomic vapor magnetometers suffer from the size of the detector chamber and can only detect nuclear spin ensemble in macroscopic dimensions. With the help of nanometer scale fabrication, the superconducting quantum interference device (SQUID) magnetometer can detect a single electron, or 10^3 small ensemble of nuclear spins from a sub-micron sensing volume. The magnetic resonance force microscope (MRFM) technique can achieve nanometer scale resolution, with the help of scanning probe microscope (SPM). The NV center is the only magnetic sensor capable of detecting a single nuclear spin, by indirect sensing via a reporter electronic spin. The typical range for each technique, and the best results reported for each technique [44-48], are compared in Figure 1 in [25]. The dipolar magnetic field due to the target spin being measured decays as the third inverse power of distance between the target spin and the magnetic sensor,

$$B \propto \frac{1}{r^3} \tag{1.2}$$

When the number of target spins is small, and the signal magnetic field is weak, it is necessary to use NV centers very close to diamond surface. Because of the fluctuating field from paramagnetic impurities on diamond surface, surface NV centers have relatively short coherence time. Unlike the nearly spinless environment in the diamond lattice, there are many kinds of spins on the surface of diamond including electron spins from dangling bonds, proton spins from hydrogen passivation, or moisture absorbed by the surface etc. If our purpose is to sense the existence of target spins, rather than non-invasive magnetic field measurement, driving the target spins actively is usually the way of distinguishing the target spins from the spin bath. This is called electron-nuclear double resonance (ENDOR) or double electron-electron resonance (DEER) for nuclear spins and electron spins sensing respectively [49]. The terms DEER and ENDOR are borrowed from pulsed electron paramagnetic resonance (EPR) experiments, and the word *electron* in DEER and ENDOR means the electronic spin of the NV center ground state.

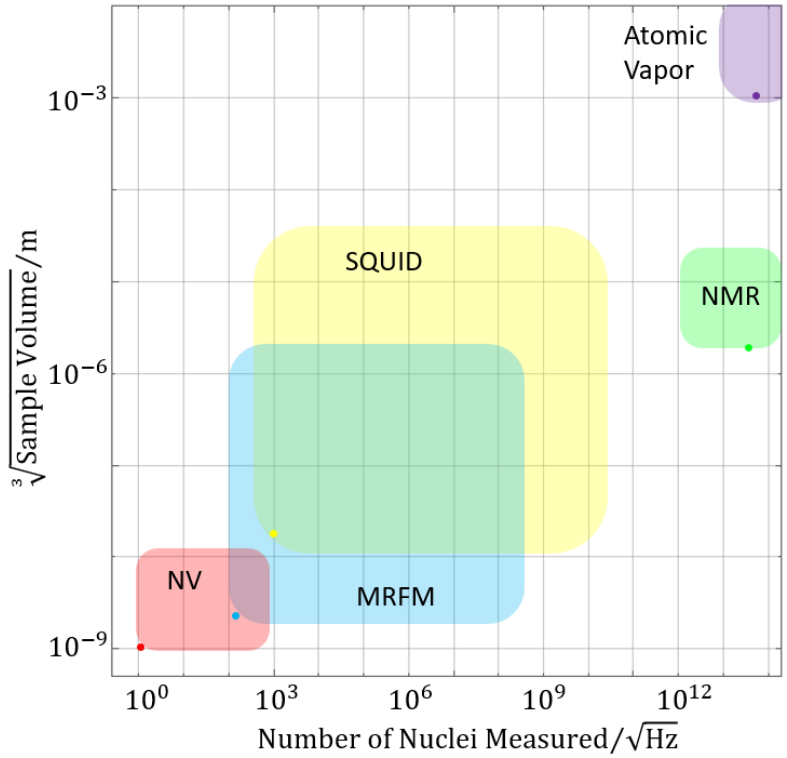

Figure 1.1 Nuclear spin sensitivity for different sensing techniques. The rectangles mark the typical range for each technique, and the dots marks the best results reported [44-48]. Atomic vapor magnetometers suffer from the size of the detector chamber and can only detect nuclear spin ensemble in macroscopic dimensions. With the help of nanometer scale fabrication, the SQUID can detect a single electron, or 10^3 small ensemble of nuclear spins from a sub-micron sensing volume. MRFM can achieve nanometer scale resolution, with the help of SPM. The NV center is the only magnetic sensor capable of detecting a single nuclear spin, by indirect sensing via a reporter electronic spin.

Engineering surface NV centers in diamond for magnetometry remains a field under improvement. The most common technique to create NV centers close to the surface is ion implantation and subsequent annealing [50, 51]. The ion straggling puts a large uncertainty on the exact depth of implanted nitrogen ions, and accurate measurement of the depth of NV centers is still a challenging work [51, 52]. The transmission yield from nitrogen ions to NV centers is low under low implantation energy [53]. Surface NV centers behave much worse in coherence time and optical stability compared to their deep-in-lattice counterparts [54]. Efforts has been made in solving these issues, including δ-doping technique for creating high-quality surface NV centers [55], and special annealing processes to improve coherence time [56, 57]. Although the coherence time of surface NV centers is still shorter than typical coherence time of NV centers in bulk diamond, it is capable of sensing individual external electron spins with the help of DEER.

As mentioned above, NV centers can also be used in thermal sensing due to its temperature-dependent zero-field splitting [21-23, 58]. On the other hand, being sensitive to temperature is a disadvantage for magnetometry applications. It is estimated that even a $0.01\ ^{\circ}\mathrm{C}$ change around room temperature will result in a $30\ \mathrm{nT}$ shift of magnetic field measurement. This effect sets a limit in DC magnetometry under room temperature without accurate temperature control.

1.3 THESIS OVERVIEW

In this dissertation, two aspects of spin physics, the Berry phase of a spin in time-dependent magnetic field, and detection of external spins are explored with single NV centers in diamond. We explored the possibility of using the geometric phase for magnetometry to improve our magnetic sensitivity. And we tried detecting magnetic resonance signal from electron spins of copper ions. The rest of the thesis is organized as follows:

chapter 2 introduces some necessary background knowledge about NV centers in diamond, including optical properties of NV centers, confocal microscopy for addressing NV centers, and coherent manipulation of spin state of NV centers.

chapter 3 demonstrates measurement of Berry phase using NV center. The Berry phase is accumulated with coherent control of the NV center, and measured via state tomography. The

properties of geometric phase, including the noise resilience, are explored, and potential applications of geometric phase is discussed.

chapter 4 shows the efforts towards a scanning diamond probe microscope, including the design of microscope and fabrication on diamond.

chapter 5 presents results in external electron spin sensing using NV center. The DEER technique is used for sensing the dipolar magnetic field due to the external electron spin while actively driving the target spin. These results open a way to further exploration of external electron spin sensing and its potential interdisciplinary applications in physical chemistry.

chapter 6 summarizes the thesis and provides a brief outlook to future directions.

2.0 BACKGROUND

This chapter introduce the necessary background knowledge of Nitrogen Vacancy centers in diamond. Some of the experiments chosen from the literature for illustrative purpose are performed in my experimental setup as well and are shown in the Appendix C.1.

2.1 NITROGEN VACANCY CENTERS IN DIAMOND

Nitrogen Vacancy centers (NV centers) are atomic scale defects in diamond lattice, consisting of one substitutional nitrogen atom and one adjacent vacancy. The crystalline structure of a single NV center in diamond lattice is shown in Figure 2.1.

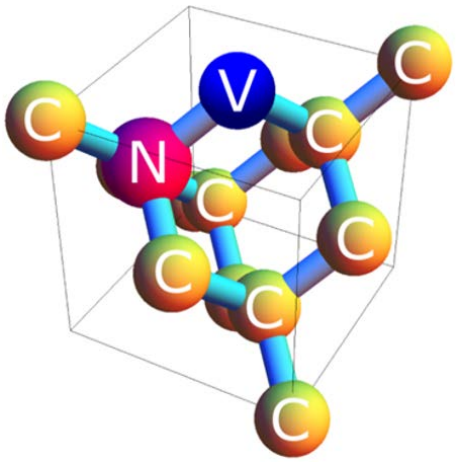

Figure 2.1 Reproduced with permission from [59]. Nitrogen Vacancy center in diamond lattice. The NV center consists of one substitutional nitrogen atom and one vacancy site adjacent to the substitutional nitrogen atom.

NV centers have two major charge states, NV^0 and NV^-. Since optical readout of spin state was reported at NV^- charge state [60], NV^- became one of the most popular quantum systems we can explore in condensed matter physics. Researches on charge state NV^0 and transitions between

charge states provide better understanding of NV centers as defect in condensed matter, and improvement of maximizing NV^- population [61-63]. Applications such as charge state memory are proposed and experimentally realized [64]. For exploration of spin physics, NV^- is more suitable because no optical readout of spin states is reported on NV^0. My thesis will focus on NV^- charge state only. Unless mentioned specifically, the terminology *NV centers* in the rest of my thesis refers to NV^- charge state.

Previous research has shown that the electronic orbitals of the NV center are highly localized at the vacancy site and its nearest neighbors [65]. The electronic system around the vacancy follows the Hamiltonian with C_{3V} symmetry (trigonal pyramidal symmetry). For NV^- state, there are 6 electrons in these orbitals, consisting of 3 unpaired electrons from the nearest carbon atom, 2 unpaired electrons from the nitrogen atom, and 1 additional electron captured by the NV center. Because of the high degree of localization, molecular model, which is initially constructed for molecules with sp^3-hybridized carbon atom, is often used to describe these defect states with four orthogonal molecular orbitals (MOs), $\{a_1', a_1, e_x, e_y\}$ [66]. One of the four MOs (a_1') lies in the valence band and will always be occupied by two paired electrons. The occupancy of the rest 4 electrons in 3 MOs forms the collective electronic states of the NV center. The electron clouds for MOs a_1, e_x, e_y can be found in [66] and the energy levels of these electronic states in diamond band structure is schematically shown in Figure 2.2. The MOs e_x and e_y form a two-fold degenerate subspace with energy higher than a_1. The exact locations of these MOs in diamond band structure depend on the occupation of each MO and the charge state of NV center.

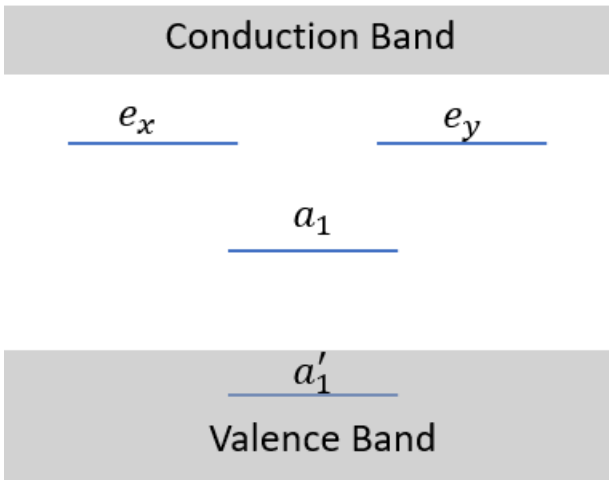

Figure 2.2 The energy levels of localized defect states in the band structure of diamond. The names of the states are borrowed from molecular orbitals with sp^3-hybridization.

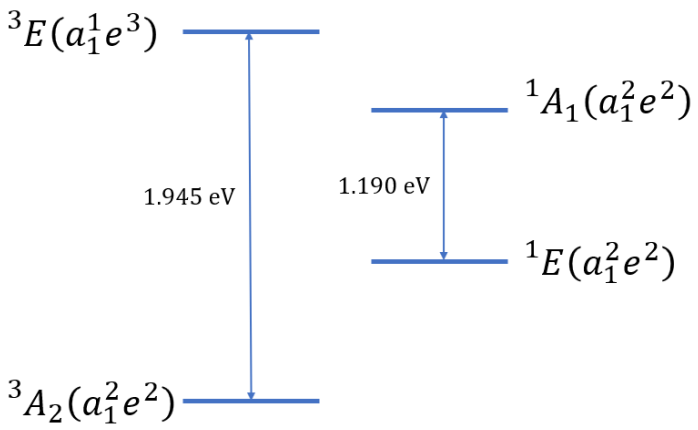

Figure 2.3 Collective electronic states of NV centers, including the ground state, the first excited state and two metastable states. The energy differences between the ground state and the first excited state, and between the two metastable states are measured via optical transitions.

The lowest collective electronic states of the NV center, including the ground state, two metastable states and the first excited state is shown in Figure 2.3. The ground state of NV center is a $^3A_2$ spin triplet ($S = 1$), where a_1 is occupied by a pair of electrons and there is one unpaired electron in e_x and one in e_y. Similar to Hund's Rule in atomic physics, the unpaired electrons in e_x and e_y have spins in the same direction, and thus forms a spin-1 system. Different occupations in e_x and e_y will form singlet ($S = 0$) metastable states (^1E, $^1A_1$). The first excited state is realized when one electron in a_1 is excited to e_x or e_y orbital. Because there are two unpaired electrons in a_1 and e orbitals respectively, the first excited state ^3E is also spin triplet ($S = 1$). More details of wave functions of these collective electronic states are in Appendix A.1 [66].

Furthermore, the ground state triplet of NV center is split in energy into $|m_s = 0\rangle$ state and $|m_s = \pm 1\rangle$ degenerate doublet states without external magnetic field due to spin-spin interaction. This zero-field splitting between $|m_s = 0\rangle$ state and $|m_s = \pm 1\rangle$ states is 2.87 GHz at room temperature. The Hamiltonian in spin subspace of the orbital ground state of NV center can be written as $H_{NV} = \frac{1}{\hbar} \cdot DS_z^2$, where $D = 2.87$ GHz and S_z is spin matrix for spin-1.[1]

The energy differences between ground state $^3A_2$ and first excited state ^3E, and between metastable states ^1E, $^1A_1$ are measured by observed optical transitions and shown in Figure 2.3.

[1] For consistency in this thesis, the unit Hz is defined as 1 Hz $= 2\pi$ rad/s. The energy is always calculated using $E = \hbar\omega$, not $E = h\nu$, and frequencies in Hz must be converted to angular frequencies in rad/s first. The spin matrices contain the factor $\hbar$.

The energy difference between the ground state and metastable states, however, cannot be measured because there are no radiative transitions. The exact location of metastable states in the energy diagram remains unknown.

2.2 CONFOCAL MICROSCOPY: OPTICAL ADDRESSING NV CENTERS

2.2.1 Optical Properties of NV Centers

The optical properties of NV centers are crucial to all applications of NV centers. NV centers have an optical absorption peak near $532\ \text{nm}$ and have fluorescence or photoluminescence[2] when exposed to $532\ \text{nm}$ green light. As shown in Figure 2.4, the NV center is pumped by the excitation light from the ground state to the absorption phonon side band of the first excited state and quickly relaxes to the first excited state ${}^3E$. The fluorescence is produced by the optical transition from the first excited state ${}^3E$ to either the ground state directly or the emission phonon side band of the ground state. The direct optical transition from the first excited state ${}^3E$ to the ground state ${}^3A_2$ corresponds to the zero-phonon line (ZPL) in the fluorescence spectrum of NV center.

The fluorescence spectrum shown in Figure 2.5 is taken with $532\ \text{nm}$ laser illumination. It includes the ZPL at $575\ \text{nm}$ and $637\ \text{nm}$, and widely spread phonon side bands at longer wavelengths for both NV^0 and NV^- respectively. Because we are only interested in NV^-, a $650\ \text{nm}$ long-pass filter is used to filter out fluorescence from NV^0.

One essential optical property of NV center is that the fluorescence level depends on its spin state, i.e. $|m_s = 0\rangle$ state gives more fluorescence photons and $|m_s = \pm 1\rangle$ state gives less. This is what we called optical readout of spin states. The spin-dependent fluorescence is due to the non-radiative decay from first excited state to metastable states is spin-dependent, as shown in Figure 2.6. $|m_s = \pm 1\rangle$ spin state of the first excited state is easier to fall into metastable state and

[2] The word *fluorescence* is usually used when the illumination light is ultraviolet, while *photoluminescence* (PL) is for visible illumination light. Strictly speaking, photoluminescence is the proper word for NV centers. Both words are used in different publications and the word fluorescence is chosen for the rest of the thesis following the convention of our group.

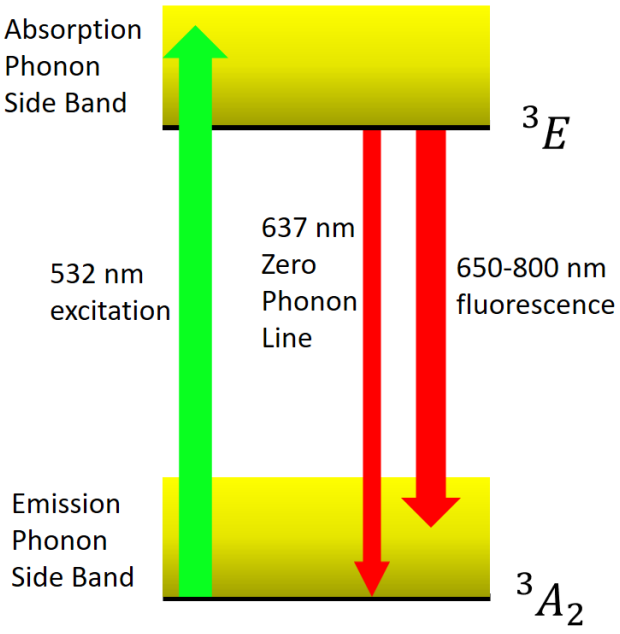

Figure 2.4 Absorption and emission phonon side band of NV centers. During one optical cycle, the illumination laser excites the NV center from ground state to the phonon side band of the first excited state, and the NV center relaxes back to the first excited state in a short time via phonon relaxation. Then the NV center relaxes to either the ground state or the phonon side band of ground state via optical transition and emits a fluorescence photon.

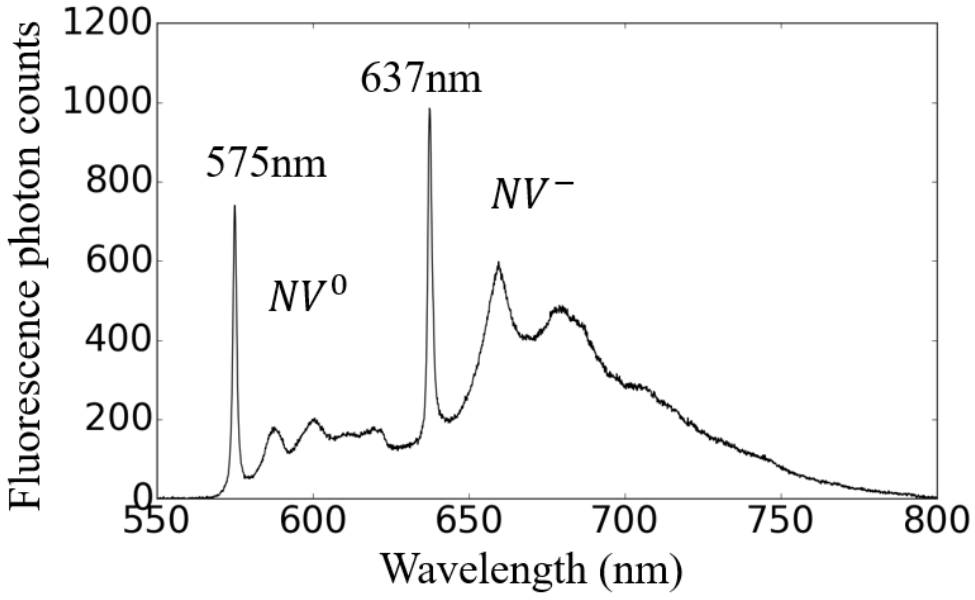

Figure 2.5 Reproduced with permission from [67]. Optical Emission Spectrum of NV Centers. The spectrum is taken with 100 nm diamond nanocrystals at 14 K. The exposure time is 30 s. The peaks at 575 nm and 637 nm are zero-phonon lines (ZPL) for NV^0 and NV^- respectively. The broad emission photon side bands are shown at longer wavelengths to the ZPL.

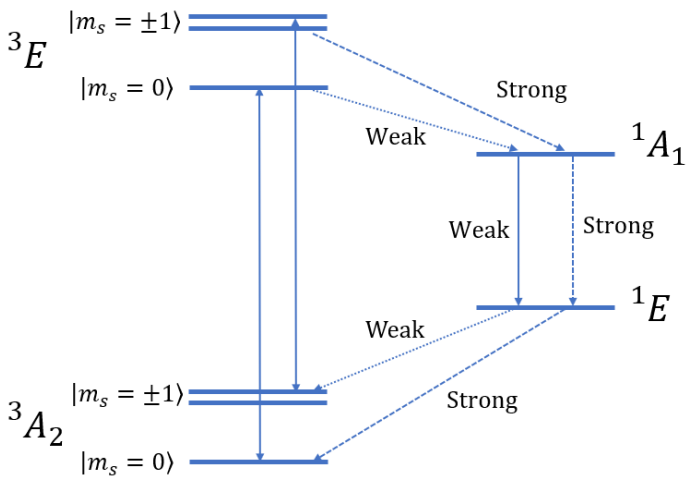

Figure 2.6 Spin-conserving optical transitions (solid arrows) and spin-dependent non-radiative decays (dashed arrows). The spin-dependent transitions are used in optical initialization and readout.

stop producing photons[3] until relaxing back to ground state while $|m_s = 0\rangle$ spin state keeps producing photons within the optical pumping cycle. The lifetime of the metastable state ^1E is $\sim 3 \times 10^{-7}$ s, much longer than the lifetime of the first excited state ^3E, being $\sim 1 \times 10^{-8}$ s [18].

Besides the optical readout, the spin-dependent non-radiative decay leads to a net flow from $|m_s = \pm 1\rangle$ state to $|m_s = 0\rangle$ state. Optical pumping is spin-preserving under dipole approximation as the Hamiltonian commutes with spins. After a period of green light exposure, the spin state of NV center can be initialized into $|m_s = 0\rangle$. This is called optical initialization of spin state. However, the fidelity of optical initialization is not reported consistently in the literature, ranging from 42 % to 96 % [18].

The optical initialization, however, put a time limit to the optical readout. As shown in Figure 2.7, when illuminated with high intensity of green light, the fluorescence intensity levels of $|m_s = 0\rangle$ state and $|m_s = \pm 1\rangle$ states are different in the first few hundred nanoseconds, and then become the same after optical initialization pumping the NV center to $|m_s = 0\rangle$ state. The time scale of optical initialization under high intensity of green illumination is $\sim 3 \times 10^{-7}$ s , same as the lifetime of ^1E metastable state. This is reasonable because the lifetime of ^1E metastable state is the time the NV center being shelved from the optical pumping cycle, while the other metastable state, $^3A_2$, has much shorter lifetime of $\sim 10^{-9}$ s [18].

[3] The radiative transition from $^1A_1$ state to ^1E state does produce photons in 1042 nm. However, the yield of radiative transition is extremely low from $^1A_1$ state to ^1E state, and our detection efficiency for infrared (IR) photons is much lower than visible red photons.

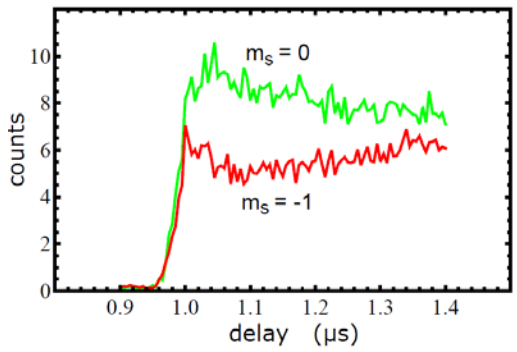

Figure 2.7 Reproduced with permission from [59]. Readout fluorescence photon counts from $|m_s = 0\rangle$ and $|m_s = -1\rangle$ state. The green and red curves are the time-resolved fluorescence photon counts from $|m_s = 0\rangle$ and $|m_s = -1\rangle$ state respectively. The illumination green light is turned on at 1.0 μs. This 1.0 μs delay is due to the rise time of acousto-optic modulator. Under high-intensity illumination, the readout contrast for different spin states decays to 0 after a few hundreds of nanoseconds, because of the optical initialization.

2.2.2 Confocal Microscope

Confocal microscope is used when the observation of single NV centers first reported in 1997 [2], and became a conventional method of addressing single NV centers. The central idea of a confocal microscope is to focus both the collection path and the illumination path on the sample at the same time.

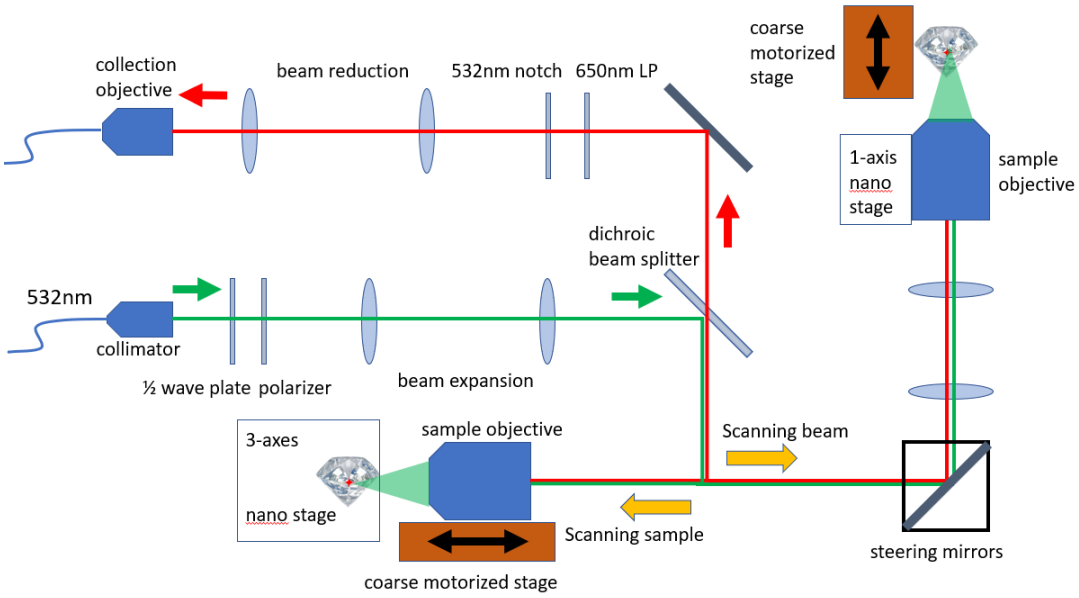

Figure 2.8 Schematic drawing of home-built confocal microscope. The two scanning mechanisms are showed at the same diagram. Scanning beam mechanism is used in chapter 3 and scanning sample mechanism is used in chapter 5.

Figure 2.8 shows the schematic drawing of our home-built confocal microscope for NV centers. The illumination light is a fiber-coupled 532 nm green laser. A collimator couples the illumination laser out to the free space as a Gaussian beam. The $\frac{1}{2}$ wave plate and the polarizer provide a handle to adjust the illumination power conveniently. A telescope lens doublet expands the Gaussian beam to fill the back aperture of our high numerical aperture (NA) sample objective. The dichroic beam splitter then reflects the green illumination beam and combines the illumination path and collection path. After focusing the illumination beam on the diamond sample, the fluorescence light (650 nm and above, red) from the NV center(s) is collimated by the sample objective, passing through the dichroic beam splitter, filtered by a series of wavelength filters, and finally coupled into a fiber with a back-coupling objective. The fluorescence from NV center(s) is typically extremely weak so we use commercial Single Photon Counting Module (SPCM), which is basically an avalanche photo diode (APD) with engineered amplifier circuits and cooling, to measure the fluorescence level. More details of our confocal microscope can be found in Appendix B.2.

There are two scanning mechanism for imaging our sample: one is scanning the sample with a nano-positioning stage while keeping the optical path stable; the other is scanning the confocal beam direction with steering mirrors and the optical focus point while keeping the sample position fixed. Both scanning mechanisms are shown in Figure 2.8. An extra telescope lens pair on the confocal path between the steering mirrors and sample objective images the steering mirrors onto the objective aperture, so the optical beam is kept filling the aperture while scanning the beam direction, as shown in Figure 2.9.

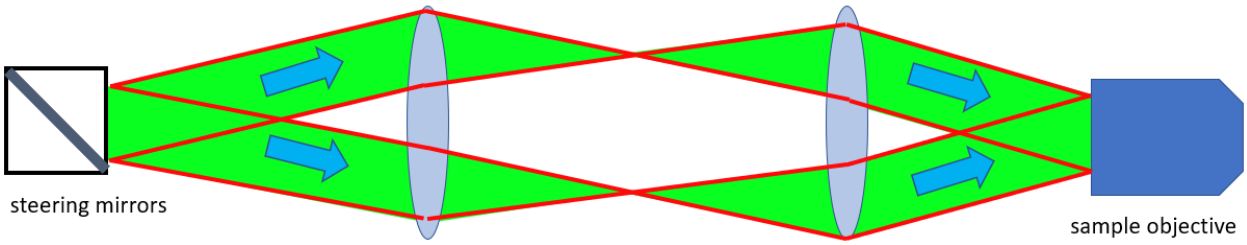

Figure 2.9 Illustration of method used to keep objective aperture filled while scanning the beam direction with steering mirrors.

The scanning sample stage mechanism is more stable, has less focus drifts and higher optical efficiency due to simpler optical design and fewer beam clippings at the edge of optical

elements (lenses, mirrors etc.). The steering mirrors mechanism is more popular because the instruments required don't need nanometer accuracy and are easily accessible commercially. The more popular steering mirrors mechanism is used for Berry phase experiments in chapter 3, and scanning sample stage mechanism for magnetic sensing experiments in chapter 5.

Figure 2.10 shows the scanning images of a single NV center acquired with two different confocal microscopes used in chapter 3 and chapter 5 respectively. The resolution and the photon counting rate for the same single NV center of the confocal microscope used in chapter 5 are observed higher than the one used in chapter 3, mainly because of the higher NA of the oil-immersion sample objective used in chapter 5. The stability of the system with scanning sample stage may also contribute to the high quality of image.

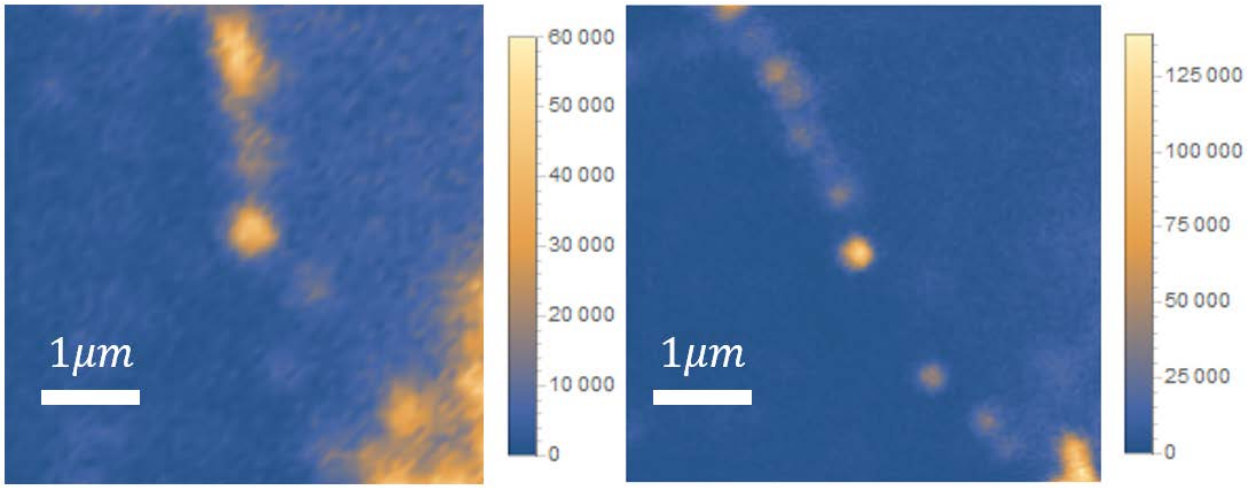

Figure 2.10 Confocal images of the same single NV center on Sumitomo type IIa diamond sample with confocal microscopes used in chapter 3 (left) and chapter 5 (right). The center bright spot with high photon counting rate is the single NV center.

Compared to the commonly used bright field microscope, confocal microscope has two major advantages. First, focused illumination light saves total illumination power when large intensity of illumination is needed, just as NV centers. Second, when aligned properly, the contrast and resolution of confocal microscope is higher because the image is effectively a product of the collection point spread function (PSF) and the illumination PSF [68]. On the other hand, the confocal microscope has two disadvantages compared to bright field microscope: the alignment of the two paths is difficult, and a scanning mechanism is needed for imaging as it can only look at one spot at a time.

2.3 OPTICALLY DETECTED MAGNETIC RESONANCE

Optically Detected Magnetic Resonance (ODMR) is an important property of NV centers for applications in magnetometry, quantum control etc. In fact, ODMR is usually the easiest achievable evidence to confirm a bright spot in our confocal image is indeed NV center, while taking the optical spectrum of a weak fluorescence source is usually time consuming and environment demanding.

2.3.1 Continuous Wave Optically Detected Magnetic Resonance

The simplest ODMR experiment is continuous wave (CW) ODMR. Here the phrase continuous wave means both the green light illumination and the microwave driving field is continuous. CW ODMR experiment was done in the same publication of observing single NV centers [2].

As mentioned in previous section 2.1, without external magnetic field, the ground state of NV center is split in energy by $\hbar \cdot 2.87$ GHz between $|m_s = 0\rangle$ state and $|m_s = \pm 1\rangle$ states. Under continuous green light illumination, the NV center is kept polarized to $|m_s = 0\rangle$ spin state. Now we scan the frequency of the continuous microwave driving field. When the microwave frequency hits 2.87 GHz, the microwave is driving the transition between $|m_s = 0\rangle$ state and $|m_s = \pm 1\rangle$ states resonantly and part of the population in $|m_s = 0\rangle$ state moves to the darker $|m_s = \pm 1\rangle$ states, resulting in a decrease in fluorescence level.

When an external magnetic field applied to the NV center along the $N - V$ axis (conventionally defined as z axis of NV center), $|m_s = \pm 1\rangle$ states are split in energy by Zeeman effect. The Hamiltonian considering a bias magnetic field along the z axis is:

$$H_{NV} = \frac{1}{\hbar} \cdot DS_z^2 - \gamma_e B_0 S_z \tag{2.1}$$

where $\gamma_e = -2.802$ MHz/G is the gyromagnetic ratio of an electron. The fluorescence dip in ODMR signal is split into 2 separate dips at frequencies $\omega_1 = D - \gamma_e B_0$ and $\omega_2 = D + \gamma_e B_0$,

corresponding to $|m_s = 0\rangle \leftrightarrow |m_s = 1\rangle$ and $|m_s = 0\rangle \leftrightarrow |m_s = -1\rangle$ transitions respectively, as shown in Figure 2.11.[4]

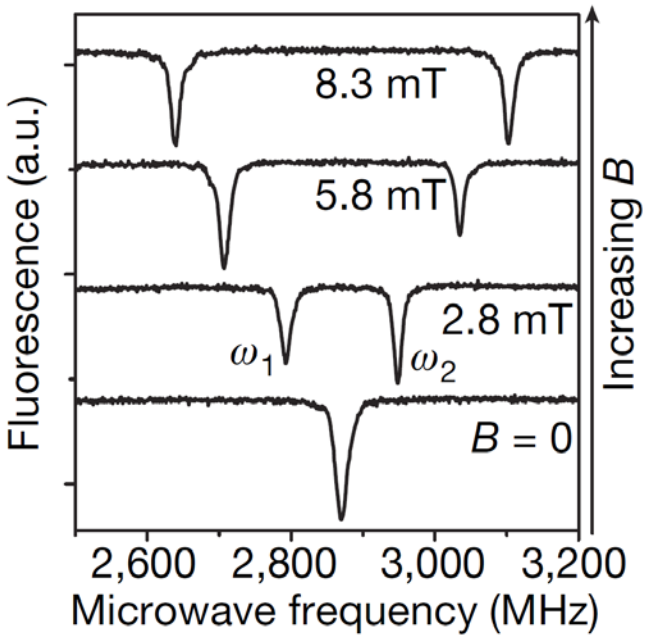

Figure 2.11 Reprinted by permission from Springer Customer Service Centre GmbH: [15], copyright (2008). Continuous wave ODMR under different external magnetic field. These spectra are recorded by monitoring the NV defect fluorescence intensity while sweeping the frequency of the microwave (MW) field. Spectra for different magnetic fields are shifted vertically for clarity.

Continuous wave ODMR experiments require the external magnetic field aligned with the $\mathrm{N-V}$ axis of the single NV center. If the external magnetic field is not along the $\mathrm{N-V}$ axis, the contrast and the fluorescence intensity will decrease significantly due to spin states mixing and NV center $\mathrm{C_{3V}}$ symmetry breaking. The fluorescence decrease due to magnetic field misalignment provides us a way to align the external magnetic field, adjusting the direction of magnetic field while looking for the maximum fluorescence.

The linewidth of CW ODMR is typically close to ~ 10 MHz with reasonable contrast, which prevents us from resolving hyperfine splitting of NV center due to the nitrogen nuclear. Although it is fast and easy to realize, CW ODMR is not the best technique in DC magnetometry in terms of sensitivity. CW ODMR is usually performed for validating NV centers, magnetic field alignment, and rough estimation of external magnetic field. More details of CW ODMR experiments can be found in Appendix A.3.

[4] The vertical axis is PL intensity (photoluminescence intensity), same as fluorescence intensity.

2.3.2 Pulsed Optically Detected Magnetic Resonance

Instead of using continuous illumination and microwave driving field, pulsed ODMR requires green light and microwave pulse in a time sequence. As shown in Figure 2.12, the first green light illumination pulse initializes the NV center to $|m_s = 0\rangle$ state, then microwave pulse is delivered to the NV center, followed by the readout illumination pulse and fluorescence measurement triggering pulse.

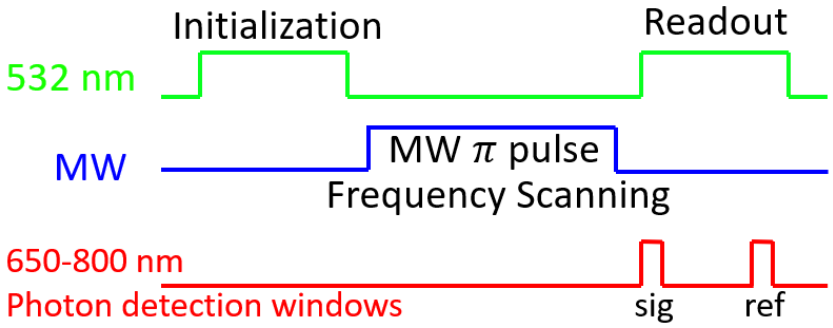

Figure 2.12 Schematic time sequence for pulsed ODMR experiments. The green laser pulses are used to initialize and readout the NV center. The microwave driving field is a π pulse with scanning frequency. Our measurement of fluorescence (signal and reference, see text) happens in the photon detection windows shown in red.

The fluorescence measurement occurs at the first 300 ns of the readout illumination pulse, before the contrast vanishes as mentioned earlier. Another fluorescence measurement is made few microseconds later in another 300 ns window as the reference fluorescence level in CW ODMR. The ratio between the fluorescence levels (signal and reference) is used as measured data in pulsed ODMR experiments. This can reduce the artifacts from sample drifting and optical focus drifting.

Practically, the fluorescence photon count collected from a single NV center is on the order of $10^4 \sim 10^5$ per second, depending on sample objective, illumination intensity and optical efficiency of the confocal microscope. With the help of some advanced fabrication techniques on diamond such as solid immersion lenses (SILs) can improve the photon count from single NV center to 10^6 per second [32]. The average photon count within a 300 ns measurement window is usually on the order of 10^{-2}. The optical measurement of spin state of NV center is not a single shot measurement. The experimental sequence in Figure 2.12 must be repeated for at least $10^4 \sim 10^5$ to accumulate sufficient photon counts for resolving different spin states. Single-shot

optical measurement of electronic spin state of single NV center has been achieved at low temperature by resonant pumping of selected spin state, which requires sharp spectrum resolution of optical transitions at low temperature only [69].

In the pulsed ODMR frequency scan experiment, the microwave driving pulse is close to a π pulse. Calibration of a π pulse with proper pulse length and microwave power will be discussed in the next section 2.4.2. The measured fluorescence ratio will decrease when the microwave π pulse frequency hits resonance.[5]

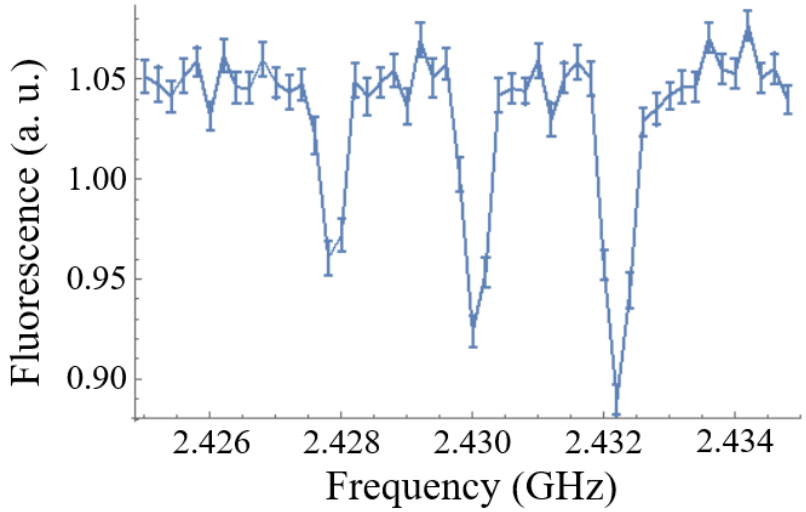

Figure 2.13 Pulsed ODMR frequency scan experiment with 2 μs π pulse on a single NV center. The triplet splitting with 2.2 MHz spacing is due to ^{14}N hyperfine interaction.

Figure 2.13 shows a pulsed ODMR frequency scan data with a 2 μs microwave π pulse. The linewidth is limited by the power broadening. For a 2 μs π pulse, the power broadening is,

$$\Delta\nu \sim \frac{1}{\tau} = 0.5 \text{ MHz}$$

where τ is pulse length. With such narrow linewidth, the hyperfine splitting of 2.2 MHz due to ^{14}N nuclear spin triplet is easily resolved.

Lower microwave driving power and longer pulse length helps narrowing the linewidth at the cost of fluorescence contrast. If the pulse length is much larger than the inhomogeneous dephasing time of the NV center (T_2^*), the contrast drops down to 0 and the ODMR dips will disappear [70]. The typical inhomogeneous dephasing time of the NV center T_2^* is 1~2 μs, but can be up to 100 μs for ultrapure diamond samples [19].

[5] Details of the line shape of pulsed ODMR is discussed in Appendix A.5.

2.4 COHERENT MANIPULATION AND DETECTION OF SPIN STATES

Coherent manipulation of spin qubits is the essential part of quantum information processing (QIP). The Bloch sphere picture of qubits is well-developed and very useful in applications other than QIP such as magnetometry. In this section, the most widely techniques in NV center magnetometry is described in the Bloch sphere picture.

2.4.1 Nitrogen Vacancy Centers as Qubits

As mentioned above, the ground state of NV center is a spin triplet. Ignoring complexities such as hyperfine splitting, strain field splitting and bias magnetic field misalignment,[6] the Hamiltonian of the ground state can be written as

$$H_{NV} = \hbar(D\sigma_z^2 - \gamma_e B_0 \sigma_z) \tag{2.2}$$

where $D = 2.87$ GHz is the zero-field splitting, $\gamma_e = -2.802$ MHz/G is the gyromagnetic ratio of electrons, B_0 is the external magnetic field aligned with $\mathrm{N}-\mathrm{V}$ axis (z axis), and $\sigma_z = S_z/\hbar$ is the Pauli matrix for $S = 1$ spin systems. In matrix form, the Hamiltonian can be written as

$$H_{NV} = \hbar \begin{pmatrix} D + |\gamma_e|B_0 & 0 & 0 \\ 0 & 0 & 0 \\ 0 & 0 & D - |\gamma_e|B_0 \end{pmatrix} \begin{matrix} |m_s = +1\rangle \\ |m_s = 0\rangle \\ |m_s = -1\rangle \end{matrix} \tag{2.3}$$

The Hamiltonian is diagonalized into three discrete energy level due to the zero-field splitting and Zeeman splitting. An external microwave driving field in transverse direction is applied to this system, with frequency close to $D + |\gamma_e|B_0$ or $D - |\gamma_e|B_0$. Assuming the direction of microwave magnetic field is along x axis, the Hamiltonian of the microwave is

$$H_{MW} = -\gamma_e B_{MW} S_x \cos(\omega t + \phi) \tag{2.4}$$

where ω close to, for example, $D - |\gamma_e|B_0$. The standard method to deal with this time-dependent Hamiltonian is switching to the rotating frame,[7] and applying rotating wave approximation [71]. The Hamiltonian in rotating frame can be simplified as,

[6] The full Hamiltonian with details is discussed in Appendix A.2.
[7] The rotating frame is discussed in Appendix A.3.

$$\widetilde{H} = \hbar \begin{pmatrix} \Delta' & \Omega e^{-i\phi}/2 & 0 \\ \Omega e^{i\phi}/2 & 0 & \Omega e^{-i\phi}/2 \\ 0 & \Omega e^{i\phi}/2 & \Delta \end{pmatrix}$$

where $\Delta = D - |\gamma_e| B_0 - \omega$ is small detuning between ω and $D - |\gamma_e| B_0$, $\Omega = \frac{|\gamma_e| B_{MW}}{\sqrt{2}}$ is a parameter describing the strength of microwave driving field. $\Delta' = D + |\gamma_e| B_0 + \omega$, which is much larger than Δ and Ω in magnitude. Because $\Delta' \gg \Delta, \Omega$, secular approximation [71] can be applied to this Hamiltonian and further simplifies it to,

$$\widetilde{H} = \hbar \begin{pmatrix} \Delta' & 0 & 0 \\ 0 & 0 & \Omega e^{-i\phi}/2 \\ 0 & \Omega e^{i\phi}/2 & \Delta \end{pmatrix} \begin{matrix} |m_s = +1\rangle \\ |m_s = 0\rangle \\ |m_s = -1\rangle \end{matrix} \tag{2.5}$$

Note that this Hamiltonian is block-diagonalized. When the initial state is $|m_s = 0\rangle$, the spin dynamics will be limited to $\{|m_s = 0\rangle, |m_s = -1\rangle\}$ subspace with effective Hamiltonian

$$\widetilde{H}_{eff} = \hbar \begin{pmatrix} 0 & \Omega e^{-i\phi}/2 \\ \Omega e^{i\phi}/2 & \Delta \end{pmatrix} \begin{matrix} |0\rangle \\ |1\rangle \end{matrix} \tag{2.6}$$

where the $|0\rangle$ and $|1\rangle$ states are defined as $|m_s = 0\rangle$ and $|m_s = -1\rangle$ states respectively. The $|m_s = +1\rangle$ state is never populated. This Hamiltonian can be expressed using spin matrices

$$\widetilde{H}_{eff} = \left(\Omega \cos\phi \, S_x + \Omega \sin\phi \, S_y - \Delta S_z\right) + const.$$

To make this effective Hamiltonian consistent in signs, we can redefine the phase of microwave driving field $\phi \to \pi + \phi$. This transformation is equivalently changing the initial phase of our rotating frame, without losing any generality. Neglecting the unimportant constant term, the Hamiltonian can be written as

$$\widetilde{H}_{eff} = -\Omega \cos\phi \, S_x - \Omega \sin\phi \, S_y - \Delta S_z \tag{2.7}$$

This is identical to the Hamiltonian of a spin-$\frac{1}{2}$ particle in an effective magnetic field

$$\widetilde{H}_{eff} = -\vec{\mu} \cdot \vec{B}_{eff} = -\gamma \vec{B}_{eff} \cdot \vec{S} \tag{2.8}$$

$$\vec{B}_{eff} = \frac{1}{\gamma} (\Omega \cos\phi \quad \Omega \sin\phi \quad \Delta) \tag{2.9}$$

The rotating wave approximation requires the anti-rotating wave is far from resonance, meaning the difference between the other resonance $D + |\gamma_e| B_0$ and microwave frequency ω must be much larger than Δ and Ω, $|(D + |\gamma_e| B_0) - \omega| \gg \Delta, \Omega$. Therefore, the Zeeman splitting of $|m_s = \pm 1\rangle$ states must be large enough to treat NV center as a two-state quantum system, or a

qubit. In most pulsed ODMR experiments of single NV centers, a bias magnetic field along the z direction ($\mathrm{N}-\mathrm{V}$ axis) is necessary.

2.4.2 Rabi Oscillation in Rotating Frame

When the frequency of microwave driving field is on resonance with the Larmor frequency of the qubit, $D-|\gamma_e|B_0$ for example, $\Delta=0$ and the effective Hamiltonian is,

$$\tilde{H}_{eff}=-\left(\Omega\cos\phi\, S_x+\Omega\sin\phi\, S_y\right) \tag{2.10}$$

This is identical to a spin-$\frac{1}{2}$ particle preceding along a magnetic field in xy plane. The spin projection on to z axis will oscillate between spin-up and spin-down states, corresponding to $|0\rangle$ and $|1\rangle$ states in Bloch sphere picture, and $|m_s=0\rangle$ and $|m_s=-1\rangle$ states of single NV centers.

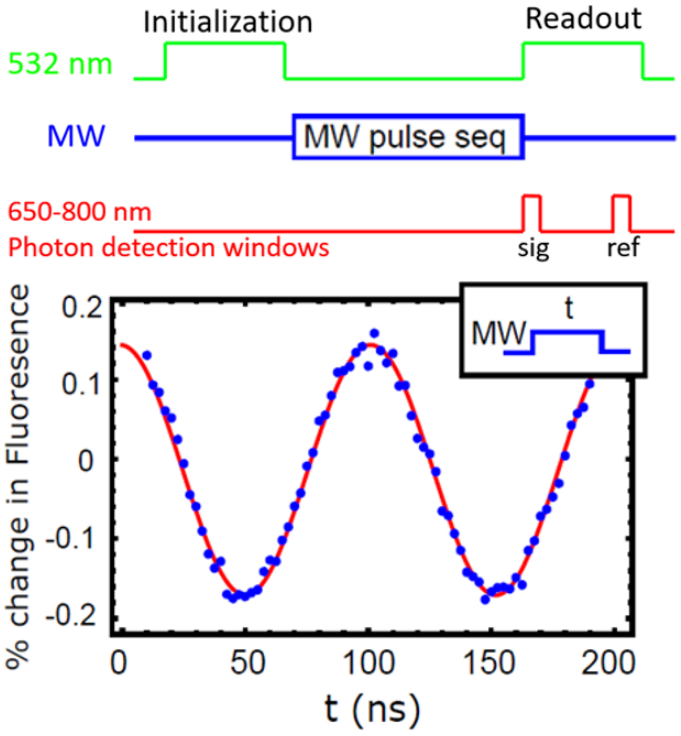

Figure 2.14 Reproduced with permission from [59]. Schematic time sequence for Rabi experiment and observed Rabi oscillation. The percentage change in fluorescence is the difference ratio between fluorescence measured in the signal window and the reference window.

Since the spin state of single NV centers can be optically detected, we can observe this oscillation experimentally. Figure 2.14 shows the schematic experimental sequence and the

observed Rabi oscillation. As we scan the pulse length with fixed microwave power, the fluorescence level oscillates between high and low levels corresponding to the $|m_s = 0\rangle$ and $|m_s = -1\rangle$ states respectively. The y axis of the data is the ratio between the signal fluorescence counts and the reference fluorescence count minus 1. The frequency of the rotation is Ω [71], and this is why the parameter Ω is often referred to as Rabi frequency.

Rabi oscillation is the key step towards coherent manipulation of single NV center as a qubit. The standard fluorescence levels of $|0\rangle$ and $|1\rangle$ states, the proper microwave power and pulse length for π pulses are all calibrates with Rabi oscillation. For example, in Figure 2.14, the π pulse can be realized with microwave pulse of 50 ns under the microwave power used in Rabi experiment. With standard fluorescence levels of $|0\rangle$ and $|1\rangle$ states, the fluorescence signals from following pulsed ODMR experiments can be mapped to probabilities in $|0\rangle$ or $|1\rangle$ states. For example, as shown in the section 2.4.3, the measured fluorescence signal from Ramsey experiment is mapped to probability in $|0\rangle$ state.

2.4.3 DC Magnetometry and Ramsey Sequence

DC magnetometry means measuring static (DC) magnetic field in the z axis ($\mathrm{N}-\mathrm{V}$ axis) of NV center. Besides the pulsed ODMR frequency scan experiment mentioned above, Ramsey sequence involving two separate $\frac{\pi}{2}$ pulses and a free precession time in between ($\frac{\pi}{2} - t - \frac{\pi}{2}$) is also used for DC magnetic field sensing. The schematic microwave sequence is shown in Figure 2.15. The optical initialization and readout protocols are omitted because these protocols remain unchanged for all pulsed ODMR experiments.

In the Ramsey sequence, the first $\frac{\pi}{2}$ pulse brings the spin state from initial $|0\rangle$ state to the superposition state,

$$|\psi(0)\rangle = \frac{1}{\sqrt{2}}(|0\rangle + |1\rangle)$$

With external magnetic field in z axis, the state evolves as a free precession for a time t.

$$|\psi^{-}(t)\rangle = \frac{1}{\sqrt{2}}\left(|0\rangle + e^{-i|\gamma_e|B_1 t}|1\rangle\right)$$

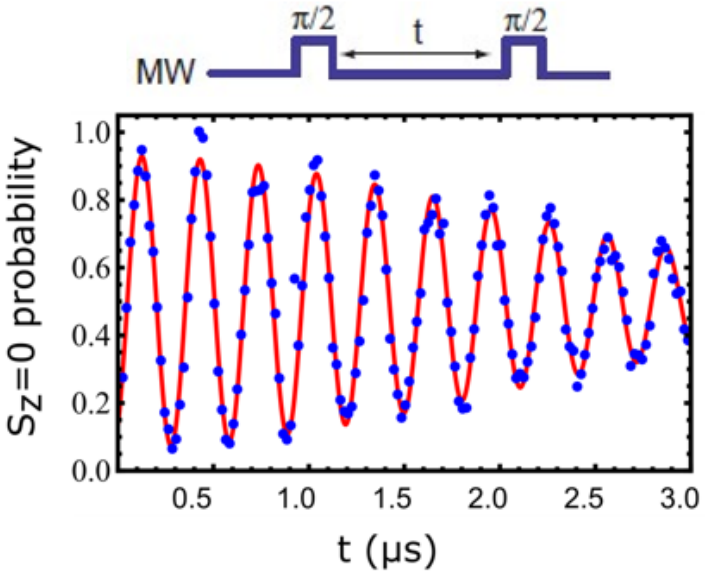

Figure 2.15 Reproduced with permission from [59]. Ramsey sequence of microwave pulses and observed Ramsey oscillation. The optical initialization and readout protocol is not shown. The measured fluorescence is mapped to probability in $|0\rangle$ state using Rabi-calibrated standard fluorescence levels. The red solid curve is the fit function as decaying oscillation.

Here the external magnetic field B_1 is an extra one besides the bias field B_0. And the second $\frac{\pi}{2}$ pulse projects the phase information in xy plane of Bloch sphere back to z axis before the measurement protocol. The expected probability is given by

$$Pr(|0\rangle) = \frac{1 - \cos(|\gamma_e|B_1 t)}{2}$$

As shown in Figure 2.15, the Ramsey oscillation decays as the sequence time increases. This is due to random fluctuations of the external magnetic field. The time scale of this decay is characterized by the inhomogeneous dephasing time, T_2^*, of the NV center.[8]

Taking the inhomogeneous dephasing into account, the probability becomes

$$Pr(|0\rangle) = \frac{1}{2} - \frac{1}{2}\cos(|\gamma_e|B_1 t)\, e^{-\frac{t^2}{T_2^{*2}}} \tag{2.11}$$

The sensitivity of magnetic field is proportional to the partial derivative of the magnetic field

$$\frac{1}{\eta} \propto \frac{\partial Pr(|0\rangle)}{\partial B_1} \propto te^{-\frac{t^2}{T_2^{*2}}} \tag{2.12}$$

[8] See Appendix A.5 for details of Ramsey decay.

and limited by T_2^*.

The 2.2 MHz hyperfine splitting due to interaction between the NV center and the nitrogen nuclear adds complexity to the Ramsey experiment results. Instead of a simple sinusoidal function, a beating behavior with 3 different frequencies is more practical output from a Ramsey experiment. This can be avoided by polarizing the nuclear spin optically. Nuclear spin polarization is usually realized by choosing the bias magnetic field $B_0 \approx 5 \times 10^2$ G.[9]

2.4.4 AC Magnetometry and Spin Echo Sequence

Compared to the sensitivity of DC magnetic field, AC magnetic field sensing can be improved by a technique called dynamical decoupling which doesn't work at DC. The improvement results from the prolongation of coherence time of NV centers. The central idea to achieve this is similar to a lock-in amplifier, decoupling the noise in frequencies different to the clock frequency of the sequence.

Spin echo sequence ($\frac{\pi}{2} - t - \pi - t - \frac{\pi}{2}$) is the simplest dynamical decoupling sequence. Besides the first $\frac{\pi}{2}$ pulse to create superposition state, and the final $\frac{\pi}{2}$ pulse for projection measurement, there is a π pulse right in the middle of the sequence to inverse the phase accumulation direction. For any DC random fluctuation in the external magnetic field, the total phase accumulated will be canceled. Only when the external magnetic field changes from the first half of spin echo sequence to the second half, a non-zero net phase is accumulated and the fluorescence will decrease.

Figure 2.16 shows a typical spin echo data. The probability hardly reaches 1 because the NV center is indeed sensing a signal of AC field due to Larmor precession of ^{13}C nuclei nearby. Every time the half length of spin echo sequence t hits the period of ^{13}C Larmor precession, the sequence becomes insensitive to this AC field and revives the probability in $|0\rangle$ state. This is called ^{13}C revivals. Since ^{13}C nuclei naturally exist in all diamond samples except for isotopically purified ones, AC magnetometry and other spin-echo-based experiments are usually performed on these revivals.

[9] See Appendix B.3 for details of optically induced nuclear spin polarization.

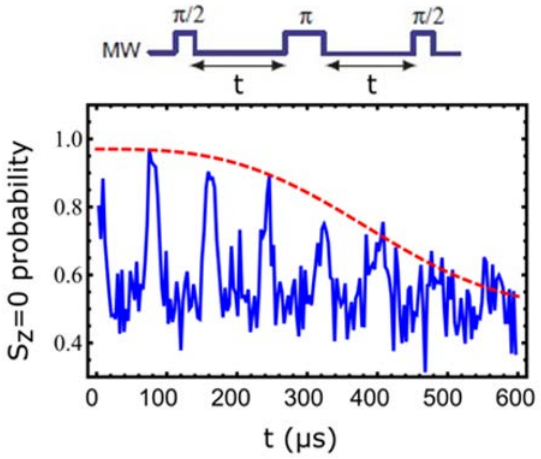

Figure 2.16 Reproduced with permission from [59]. Spin echo sequence of microwave pulses and observed oscillation. The optical initialization and readout protocol is omitted. The measured fluorescence is mapped to probability in $|0\rangle$ state using Rabi-calibrated standard fluorescence levels. The peaks are the ^{13}C revivals and the red dashed envelope shows the decay of signal when the echo time reaches the coherence time T_2.

The red envelope dashed line in Figure 2.16 shows the decay of revivals. The time scale characterizing this decay in signal is T_2, the coherence time of NV center. The coherence time is a key factor of quantum systems and sensors because it put a quantum limit to the coherent manipulation and magnetic field sensitivity.

3.0 MEASUREMENT OF BERRY PHASE ON SINGLE SPIN IN DIAMOND

This chapter demonstrates measurement of Berry phase using NV center. The properties of geometric phase are explored, and potential applications of geometric phase is discussed. Significant portions of the work in this chapter have been published in [72].

3.1 INTRODUCTION: BERRY PHASE AND GEOMETRIC PHASE

In the field of quantum information science, holonomic quantum computation was proposed to take advantage of the robustness of geometric phase against certain types of errors [73]. It was believed that such robustness could potentially be used to improve quantum information processing (QIP) with dynamic phase. Proposals and experiments on quantum gates implemented with adiabatic and non-adiabatic, Abelian and non-Abelian geometric phases [74-80].

Holonomy is often explained using Figure 3.1. When a vector is moving along a closed path on a spherical surface while keeping its direction parallel to its previous direction, the direction of the vector can still be changed after cycling the closed loop. Here the word parallel means the vector is moving under parallel transport on a curved surface, or in other words, moving without rotation about the instantaneous normal of the surface [81]. For example, in Figure 3.1, the vector first moves from the north pole to the equator while keeping its direction pointing south, then moves along the equator keeping its direction, and finally moves back to the north pole keeping its direction pointing south. After the whole cycle, the direction of the vector is changed. Keeping the direction south fulfills the parallel transport as long as the paths are part of great circles of the sphere.

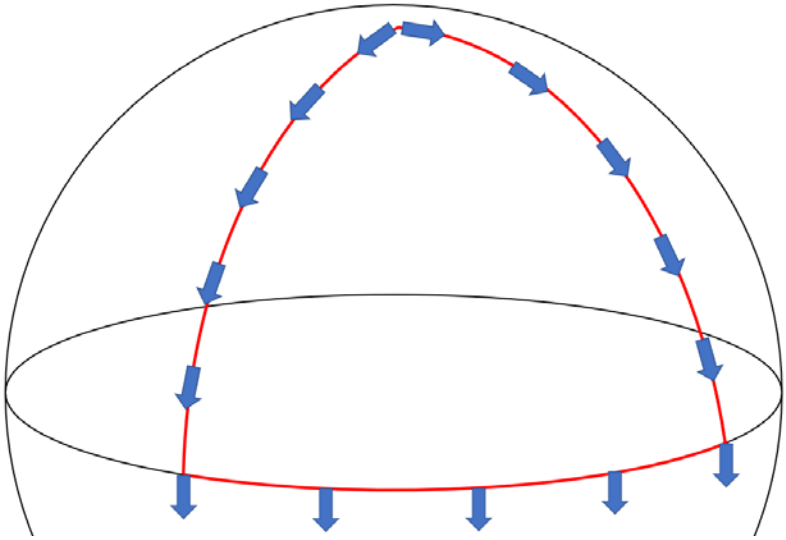

Figure 3.1 Holonomy due to parallel-transport of a vector. After moving along the closed loop (red solid curve) while keeping the direction parallel to the last instant, the direction of the vector is changed when it goes back to the north pole.

Classical parallel transport helps to understand geometric phase, which is the counterpart in quantum mechanics of classical vector holonomy. In quantum mechanics, an adiabatically changing Hamiltonian of a spin-$\frac{1}{2}$ system can be considered as an effective magnetic field varying slowly, as discussed in section 2.4.1. If the initial spin state aligns with the initial effective magnetic field, the spin aligned with this slowly varying effective magnetic field will be kept aligned with the field under adiabatic approximation [82]. Suppose the Hamiltonian is periodic, and the effective magnetic field forms a closed loop in the parameter space. After one period of the Hamiltonian, besides the trivial dynamic phase

$$\beta_D = \gamma_s \int_0^T B(t)dt \tag{3.1}$$

where γ_s is the appropriate gyromagnetic ratio for the spin and $B(t)$ is the instantaneous magnitude of effective magnetic field, an extra phase, β_G, the geometric phase due to holonomy in parameter space, is also accumulated. As a result, the net phase accumulated is $\beta = \beta_D + \beta_G$. Berry proved this in 1984 and calculated the geometric phase as

$$\beta_G = \pm\frac{\Theta}{2} \tag{3.2}$$

where Θ is the solid angle that the varying magnetic field traces out in the parameter space. The $\pm$ sign depends on whether the initial spin state is aligned with or against the effective magnetic field

[82]. The geometric phase induced by adiabatically varying Hamiltonian is thus called Berry phase.[10]

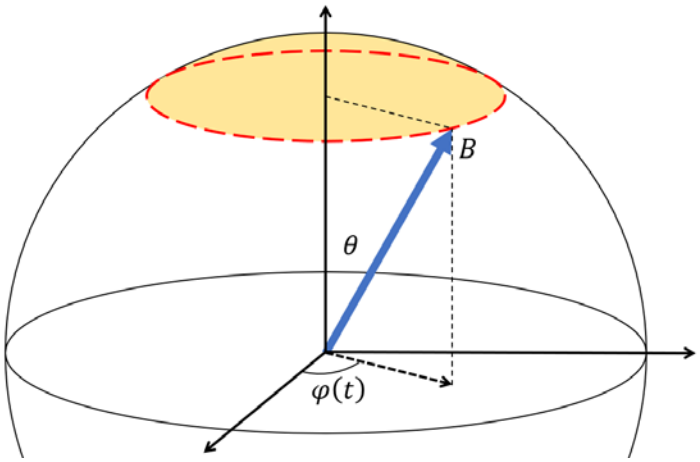

Figure 3.2 Adiabatically rotating magnetic field used in example of Berry phase. The time-dependent magnetic field is rotating in the parameter space along the closed loop (red dashed line). The solid angle of the closed loop towards the origin is marked yellow.

An example of Berry phase commonly demonstrated is a spin-$\frac{1}{2}$ system under a rotating magnetic field, as shown in Figure 3.2. The magnetic field is rotating azimuthally by changing azimuthal angle φ without changing its magnitude B and polar angle θ. The motion of magnetic field forms a closed loop in parameter space and the solid angle of the closed loop (shown in Figure 3.2) can be calculated as,

$$\Theta = 2\pi(1 - \cos\theta) \tag{3.3}$$

where θ is the constant polar angle [82].

Aharonov and Anandan showed that the Berry phase can be extended into non-adiabatic situation [83]. The adiabatically varying Hamiltonian of the quantum system drives the spin state rotating in the Bloch sphere in a well-controlled manner under adiabatic approximation. But this is not the only way to drive the spin state in Bloch sphere. For example, to recover the motion of spin state under Hamiltonian shown in Figure 3.2, an alternative way is the precession of spin state about an external magnetic field along z axis. In fact, as long as the spin state travels through a closed loop in Bloch sphere, a geometric phase will be accumulated. This non-adiabatic geometric phase is sometimes referred to as Aharonov-Anandan phase, or AA phase.

[10] See Appendix A.7 for detailed derivation of Berry phase.

Geometric quantum logic gates were first realized with nuclear spins in liquid solutions of molecules using nuclear magnetic resonance (NMR) techniques [74]. Observation of geometric phase is also reported in trapped ions, semiconductor quantum dots and superconducting qubits [76, 84]. NV centers in diamond are ideal single spin qubits for exploring geometric phase because of the remarkable degree of coherent manipulation [3, 85]. Proposals to measure Berry phase in mechanically rotating diamond crystal and implement gyroscopes can also be found in literature [86]. Experimental results of non-adiabatic geometric gates in single NV centers and observation of Berry phase with all-optical manipulation of NV centers were reported [79, 80, 87] while our paper [72] was in preparation.

3.2 MEASUREMENT OF BERRY PHASE: METHOD, THEORY AND SIMULATIONS

In section 2.4.1 it is shown that the single NV centers under bias magnetic field along z axis (N − V axis) and microwave driving field can be treated as a spin-$\frac{1}{2}$ system with Hamiltonian in rotating frame as in equation 2.7:

$$\widetilde{H}_{eff} = -\Omega\cos\phi\, S_x - \Omega\sin\phi\, S_y - \Delta S_z$$

where $\Omega = \frac{|\gamma_e| B_{MW}}{\sqrt{2}}$ is the Rabi frequency of the microwave driving field, ϕ is the phase of the microwave, and $\Delta = \omega_L - \omega_{MW}$ is the detuning of microwave field from the Larmor frequency of NV center qubit. It is also shown that this Hamiltonian is identical to the Hamiltonian of a spin-$\frac{1}{2}$ particle in an effective magnetic field as in equation 2.9:

$$\vec{B}_{eff} = \frac{1}{\gamma}(\Omega\cos\phi \quad \Omega\sin\phi \quad \Delta)$$

Thus, by modifying microwave parameters Ω, Δ and ϕ, we can build any time-dependent effective magnetic field for the spin-$\frac{1}{2}$ system. To recover the magnetic field cycle shown in Figure 3.2, parameters Ω and Δ are fixed and ϕ is changing from 0 to 2π. Berry phase on this spin-$\frac{1}{2}$ system can be accumulated in a well-controlled way with proper microwave modulation.

3.2.1 Spin Echo Sequence and Experimental Setup

Since the phase of a quantum state cannot be measured directly, interferometry of two different states is used in observation of Berry phase. The spin is initialized to the coherent superposition state of $|0\rangle$ and $|1\rangle$, then the $|0\rangle$ component and $|1\rangle$ component acquires a quantum phase respectively, and finally the relative phase between $|0\rangle$ and $|1\rangle$ can be measured as mentioned in previous chapter. Consider the cyclic motion of effective magnetic field in Figure 3.2, as $|0\rangle$ and $|1\rangle$ states accumulate geometric phase $+\frac{\Theta}{2}$ and $-\frac{\Theta}{2}$ respectively within one cycle, the relative phase accumulated within one cycle is Θ.

To isolate the Berry phase from the accompanying dynamic phase, a spin echo sequence is used to cancel the trivial dynamic phase. The experimental sequence is shown in Figure 3.3.

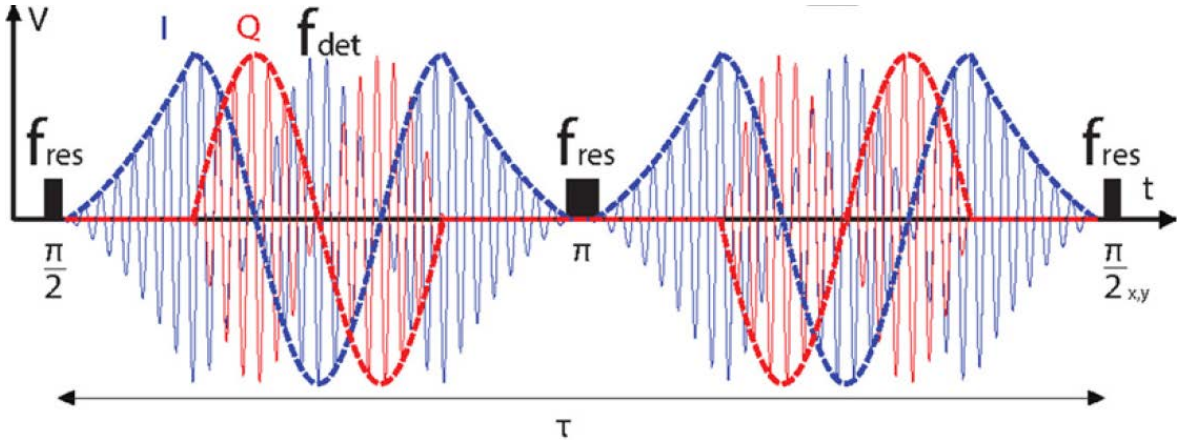

Figure 3.3 Schematic time sequence of modulated microwaves for Berry phase measurement. The black blocks represent resonant microwave pulses. The blue and red solid curves are detuned microwave driving field modulated via IQ modulator. The modulation functions are shown as blue and red dashed curves.

The first $\frac{\pi}{2}$ pulse initializes the NV center qubit to superposition state. This is a resonant microwave pulse and calibrated with Rabi oscillation in previous chapter. Then a detuned microwave is ramped up adiabatically (the first rising of blue dashed envelope in Figure 3.3) with amplitude modulation. Note that the rotating frame is used to deal with time-dependent driving field. To avoid the time-dependent Hamiltonian, the frequency of the rotating frame must be chosen equal to the instantaneous frequency of the driving field. Thus, before the ramping-up, the frequency of the rotating frame is changed from ω_{res} to ω_{det}, the detuned frequency of the microwave from the second synthesizer. For $\omega_{det} < \omega_{res}$, $\Delta > 0$, the effective magnetic field

without microwave is along z axis. The ramping-up process of the microwave amplitude correspond to the change in polar angle of effective magnetic field, as shown in Figure 3.4 left. After that, a phase modulation on the detuned microwave is performed with IQ modulator (the sinusoidal I and Q envelope in Figure 3.3). This phase modulation process corresponds to the rotation of effective magnetic field about the z axis as shown in Figure 3.4 middle. And the microwave is ramped down via amplitude modulation, corresponding to the falling of blue dashed envelope in Figure 3.3. The complete closed loop of magnetic field in its parameter space is shown in Figure 3.4 right.

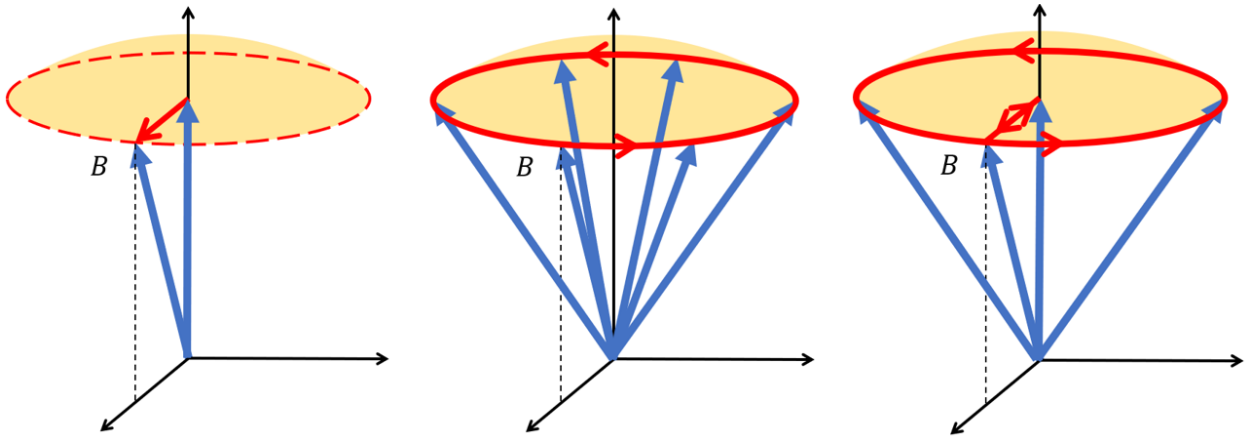

Figure 3.4 Motion of effective magnetic field for ramping-up and phase modulation of detuned microwave. Left, the ramping up step. Middle, the phase modulation step. Right, the complete procedure and the closed loop in parameter space.

Considering fast fluctuations in the resonance frequency of the NV center, the start and end of the path may not coincide with each other at the z axis, and as a result, the complete path in parameter space may not be closed. In this case, instead of using the original definition of Berry phase, which requires a closed path, we can use the generalized definition of Berry phase by Samuel and Bhandari in [88] about noncyclic evolution. However, this subtlety would not influence the results of our experiments [89].

The π pulse in the middle of the sequence inverts the phase accumulated in the first half of spin echo, including both dynamic phase and geometric phase. In the second half of the spin echo sequence, the (ramping up – phase modulation – ramping down) processes are repeated except for the direction of phase modulation is toggled. As the effective magnetic field rotated inversely in the second half, the geometric phase accumulated in the second half is the opposite of its counterpart in the first half, while the dynamic phases in both halves are identical and cancelled

by the spin echo sequence. This is the method we used for isolating the geometric phase from the dynamic phase. Finally, the $\frac{\pi}{2}$ pulse in either x or y direction is used for state tomography, which measures either S_x or S_y before the last $\frac{\pi}{2}$ pulse by projecting the S_x or S_y signal onto the z axis. The total geometric phase accumulated in both halves of the spin echo can be extracted from the measured spins S_x and S_y.

The confocal microscope with steering mirrors is used for addressing single NV center in diamond. A permanent magnet is placed near the diamond sample stage and creates a bias magnetic field of $\sim 4.5 \times 10^2$ G along the N − V axis. The strength of magnetic field is estimated from the $D - |\gamma_e| B_0 = 1.614$ GHz resonance of NV center, which is measured by pulsed ODMR frequency scan. The microwave is delivered to the NV center through a copper wire on top of the diamond sample with 20 μm thickness. The microwave circuit used in Berry phase measurement is shown in Figure 3.5. Two independent microwave synthesizers are the sources of microwaves with different frequencies we use in the experiment. The microwave with resonant frequency is split into two with phase difference of $\frac{\pi}{2}$, and pulsed with switches to create resonant pulses. The detuned microwave is sent into an IQ modulator and modulated by the outputs of 2-channel AWG (Arbitrary Waveform Generator). The combined microwave is then sent to the NV center via the copper wire. Detailed instruments are listed in Appendix D.1.

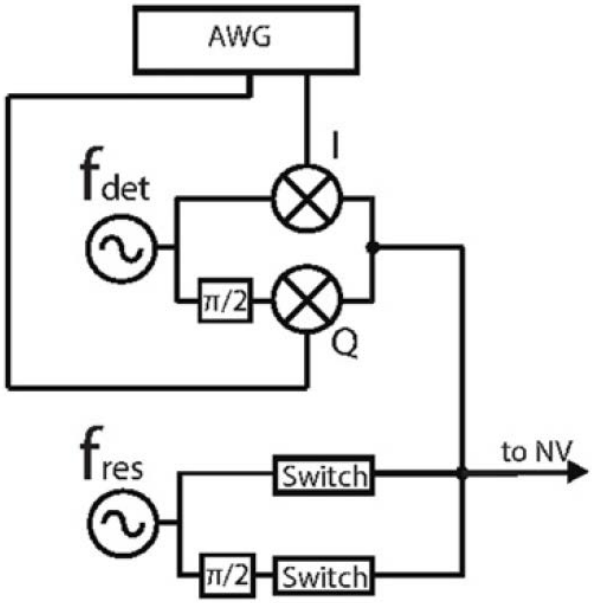

Figure 3.5 Schematic drawing of microwave circuit. The detuned microwave goes through an IQ modulator controlled by an arbitrary waveform generator, and combined with pulsed resonant microwave before delivered to NV center.

As mentioned in section 2.4.4, because of the collapses and revivals of spin echo signal due to the ^{13}C nuclei nearby, measurements based on spin echo sequence are limited to sequence times of ^{13}C revivals. We estimated the first ^{13}C revival at $2\ \mu s$, given the magnetic field of $\sim 4.5 \times 10^2$ G, and this agrees with our spin echo experiment result. The first ^{13}C revival at $2\ \mu s$, with total sequence time $\tau = 4\ \mu s$, is used for Berry phase measurement.

3.2.2 Theory and Simulation

As mentioned in previous section 3.2.1, during the first half of spin echo sequence, the relative quantum phase between the $|0\rangle$ and $|1\rangle$ accumulated can be written as $\beta_D + \beta_G$, where β_D is dynamic phase and β_G is geometric phase. The π pulse in the middle flips it to $-\beta_D - \beta_G$. During the second half of spin echo, the quantum phase accumulated is $\beta_D - \beta_G$. Here the geometric phase becomes the opposite and the dynamic phase remains the same, because the direction of cyclic motion is flipped by flipping the direction of phase modulation. The net phase accumulated in the complete sequence is $-2\beta_G$. The magnitude of the net phase is,

$$\beta = -2\beta_G = -2\left(\frac{N}{2}\right)\Theta = -N\Theta \tag{3.4}$$

where N is the total number of cycles and $\frac{N}{2}$ is the number of cycles in each half of spin echo, Θ is the solid angle of the closed loop towards the origin. For example, the sequence shown in Figure 3.3 corresponds to $N = 2$, as the effective magnetic field cycles one revolution on each half of spin echo sequence. The solid angle is calculated as

$$\Theta = 2\pi(1 - \cos\theta) = 2\pi\left(1 - \frac{\Delta}{\sqrt{\Delta^2 + \Omega^2}}\right)$$

where Δ is the frequency detuning of the detuned microwave from the resonance frequency, and Ω is the Rabi frequency of the detuned microwave. The phase being measured is

$$\beta = \beta(\Delta, \Omega, N) = -2\pi N\left(1 - \frac{\Delta}{\sqrt{\Delta^2 + \Omega^2}}\right) \tag{3.5}$$

The final $\frac{\pi}{2}$ pulse in either x or y direction for state tomography is realized by power splitter with $\frac{\pi}{2}$ phase shift for the resonant microwave shown in Figure 3.5. The measured signal in S_x and S_y is $\cos\beta$ and $\sin\beta$ respectively.

$$S_x = \cos\left[2\pi N\left(1 - \frac{\Delta}{\sqrt{\Delta^2 + \Omega^2}}\right)\right] \tag{3.6}$$

$$S_y = -\sin\left[2\pi N\left(1 - \frac{\Delta}{\sqrt{\Delta^2 + \Omega^2}}\right)\right] \tag{3.7}$$

For $N = 2$ as the microwave sequence shown in Figure 3.3, the spin vectors as function of Ω, the Rabi frequency of the detuned microwave, can be calculated as in Figure 3.6, given the detuning $\Delta = 10$ MHz fixed. We can also scan the detuning Δ while keeping the Rabi frequency Ω fixed, as shown in Figure 3.7. Sinusoidal signal is expected when we scan N while keeping both Δ and Ω fixed, because β is proportional to N.

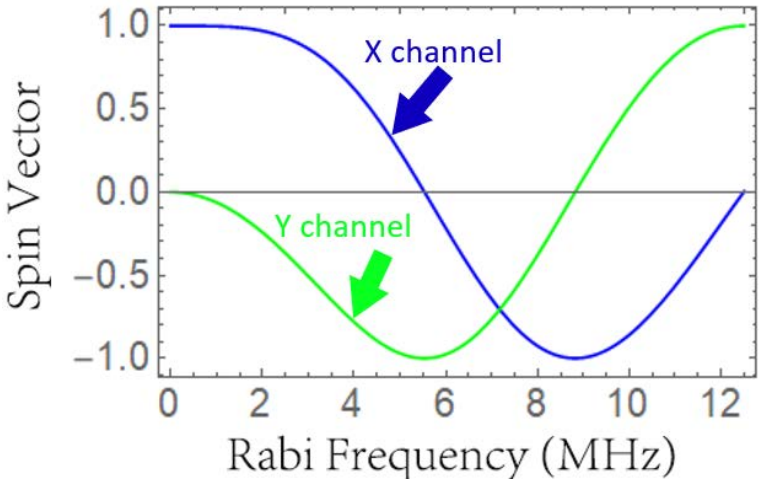

Figure 3.6 Theoretical prediction of measured probabilities as function of Rabi frequency for $\Delta = 10$ MHz. Blue and green curves correspond to S_x and S_y, respectively.

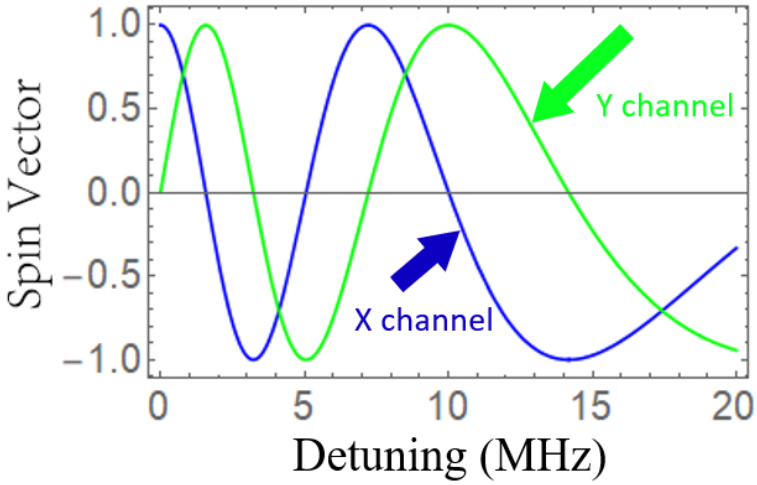

Figure 3.7 Theoretical prediction of measured probabilities as function of detuning for $\Omega = 12.5$ MHz. Blue and green curves correspond to S_x and S_y, respectively.

3.3 MEASUREMENT OF BERRY PHASE: EXPERIMENTAL RESULTS

In this section the Berry phase measurement is shown as function of Ω and N respectively. Comparison with theoretical prediction shows an obvious deviation. The Berry phase measurement as function of Δ is shown in Appendix C.4.

3.3.1 Berry Phase as Function of Microwave Amplitude

Figure 3.8 shows the data of Berry phase signal as varying Rabi frequency of the detuned microwave while the detuning $\Delta = 10$ MHz remains fixed. The theoretical expectation is also plotted as dashed lines.

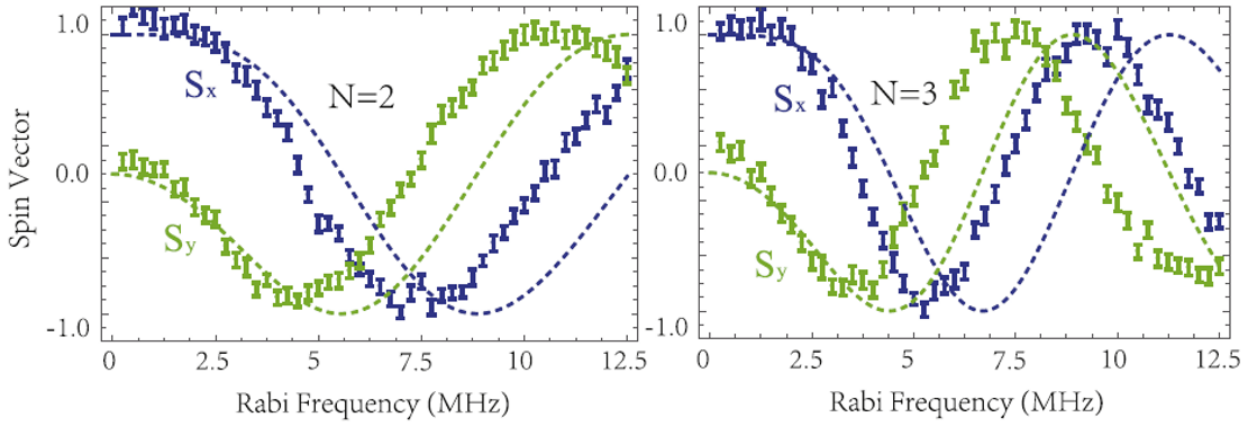

Figure 3.8 Measured S_x and S_y as function of Rabi frequency at $\Delta = 10$ MHz. The dashed line for comparison is theoretical calculation according to our theory in section 3.2.2.

To verify that the data observed is indeed due to geometric phase instead of other artifacts, the same measurement is carried out where we do not reverse the direction of the effective magnetic field rotation in the second half of the spin echo sequence. The oscillations disappear since both dynamic phase and geometric phase are cancelled by the spin echo, as shown in Figure 3.9.

From the measured spin vector in x and y direction, we can extract the net quantum phase accumulated during the whole sequence. The extracted phase data for different values of N (the

number of cycles in the whole spin echo sequence) is plotted in Figure 3.10 as function of calculated solid angle with varying Rabi frequency. $N = 0$ branch is obtained with the cancellation of Berry phase data shown in Figure 3.9.

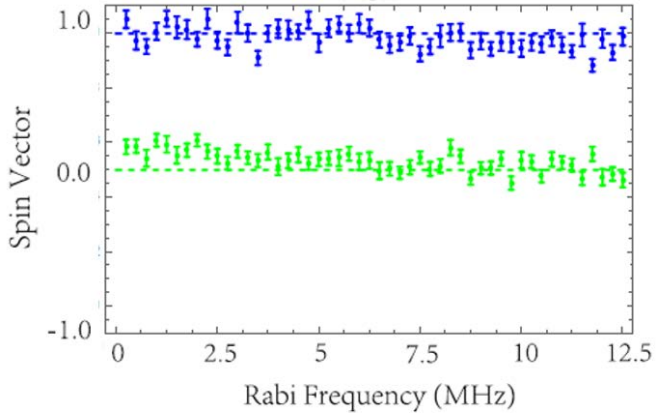

Figure 3.9 Cancellation of Berry phase. We did not flip the direction of the cyclic motion of effective magnetic field in the second half of spin echo sequence. The Berry phase is cancelled just like the dynamic phase. The measured S_x and S_y show no obvious change as we scan the Ω.

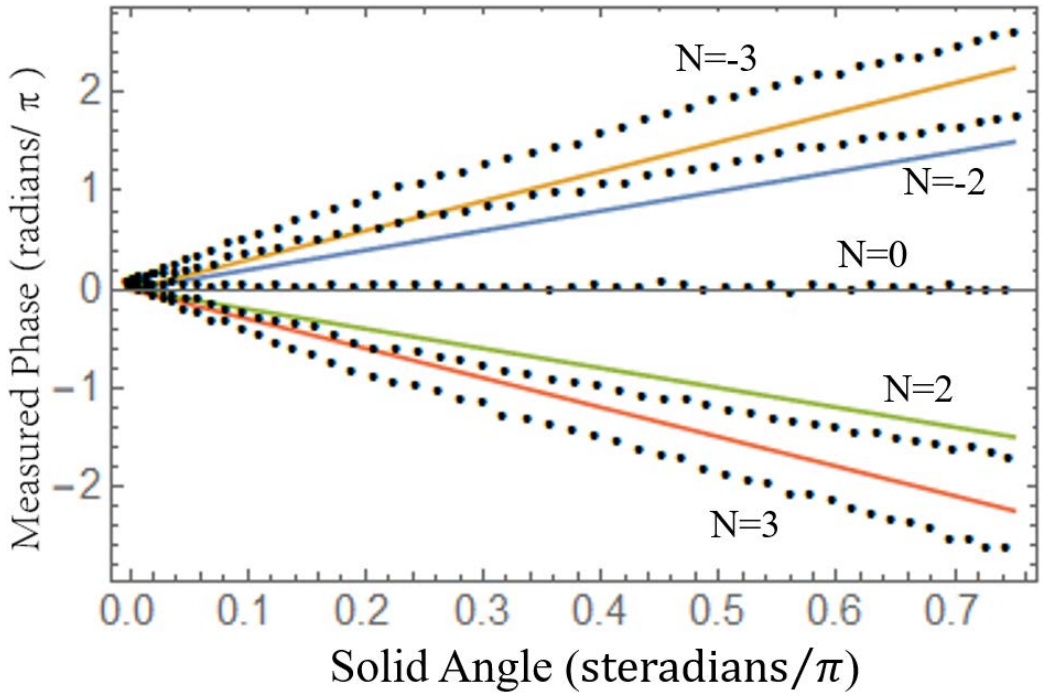

Figure 3.10 Plot of the measured phase against the calculated solid angle based on varying Rabi frequency, for different values of N. The measured phase is extracted from the measured spin vector data, for example, data shown in Figure 3.8 for $N = 2$ and $N = 3$. The $N = 0$ branch is obtained with the cancellation of Berry phase data shown in Figure 3.9. Straight lines with slope ± 2, ± 3 are theoretical predictions as the net phase proportional to solid angle.

3.3.2 Berry Phase in Varying Cycle Numbers

Unlike the Rabi frequency Ω and the frequency detuning Δ, the net phase being measured is linearly dependent on the number of cycles, N. We can test this linear dependency by scanning the N while keeping Ω and Δ fixed. First the definition of N should be broadened to non-integer. Figure 13 shows the corresponding closed loop in parameter space when N is fractional. The solid angle of the closed loop is still defined as the solid angle of the whole spherical cap. The ratio between the actual solid angle of the closed loop and the solid angle of the spherical cap is defined as N. In fact, the $N = \pm 3$ situation in previous section 3.3.1 consist of a fractional $N = \pm\frac{3}{2}$ on each half of the spin echo.

The 2 μs spin echo sequence can handle $N = \pm 3$ on each half without breaking the adiabaticity condition. But as the number of cycles increases further, a longer spin echo sequence is needed. For the N scan experiment, we chose the fifth ^{13}C revival, which is at 10 μs ($\tau = 20$ μs in total).

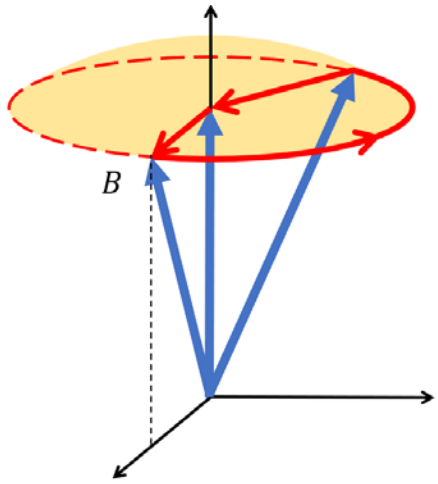

Figure 3.11 Closed path the effective magnetic field traces out for fractional number of cycles. The yellow sphere cap shows the solid angle of the entire circle. The solid angle of the closed path is a fraction of the sphere cap.

The fixed parameters, the Rabi frequency Ω and the frequency detuning Δ, are chosen to be $\Omega = 12.5$ MHz and $\Delta = 20$ MHz. The solid angle based on Ω and Δ is calculated as

$$\Theta = 2\pi\left(1 - \frac{\Delta}{\sqrt{\Delta^2 + \Omega^2}}\right) = 0.955 \text{ sr}$$

As shown in Figure 3.12, the measured spin vector signals are sinusoidal functions (with decay) of N as expected $\beta = -N\Theta$. To take the decay of signal into account, we assume a Gaussian error in the fixed solid angle and obtain the expression of measured signal as

$$S_x = \cos(-N\Theta)\exp\left(-\frac{N^2}{N^{*2}}\right) \tag{3.8}$$

where N^* is a parameter characterizing how fast the decay happens. Detailed discussion of the decay can be found in next section 3.4. The measured spin vectors are then fitted to this expression with fit parameters Θ and N^*. The solid angle is treated as a fit parameter instead of a constant because of the deviation of measured phase from theory mentioned in previous section 3.3.1. The fitted solid angle from the N scan experiment is 0.817 sr, and the fitted N^* is 13.95.

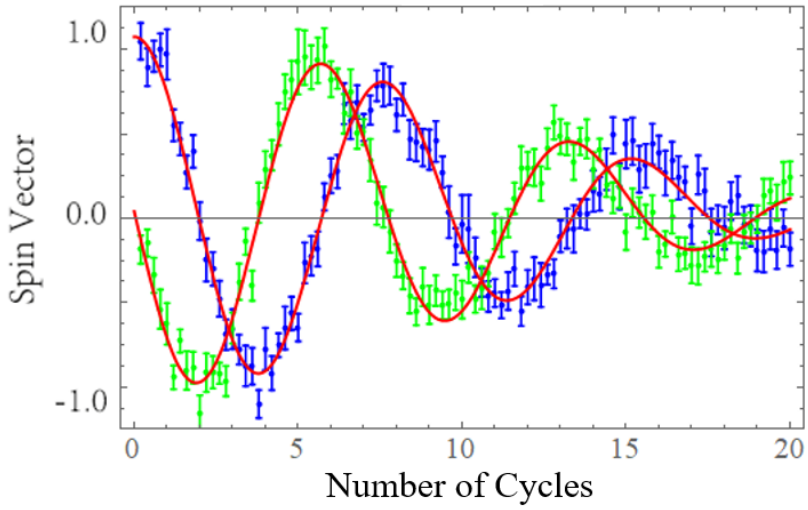

Figure 3.12 Measured S_x and S_y as function of number of cycles. The red solid curves are fits to sinusoidal functions with decay (see text).

3.3.3 Explanation of Deviation and Related Test Experiments

To find a reasonable explanation of the deviation between measured phase and theoretical prediction, a series of test experiments were performed to verify our microwave parameters, stability, fluorescence levels of NV center, adiabaticity etc.

The first parameter being tested is the Rabi frequency Ω at detuned frequencies. The Rabi frequency is proportional to microwave amplitude and is calibrated everyday with resonant Rabi oscillations. However, microwave amplitude of the detuned microwave is not tested. Microwave

components, especially amplifiers, may have frequency-dependent output amplitude. Although the frequency of detuned microwave is only shifted slightly by tens of megahertz, it's worth to be tested with Rabi oscillations of NV center. Under detuned microwave driving field, the frequency, amplitude, and equilibrium position of the Rabi oscillation vary according to the frequency detuning. As the detuning increases, the frequency of Rabi oscillation increases as

$$\Omega_{eff} = \sqrt{\Omega^2 + \Delta^2} \tag{3.9}$$

And the amplitude of the Rabi oscillation decreases as

$$A(\Delta) = A(0)\frac{\Omega^2}{\Omega^2 + \Delta^2} \tag{3.10}$$

while the equilibrium position of the Rabi oscillation increases as

$$b(\Delta) = b(0) + A(0)\frac{\Delta^2}{\Omega^2 + \Delta^2} \tag{3.11}$$

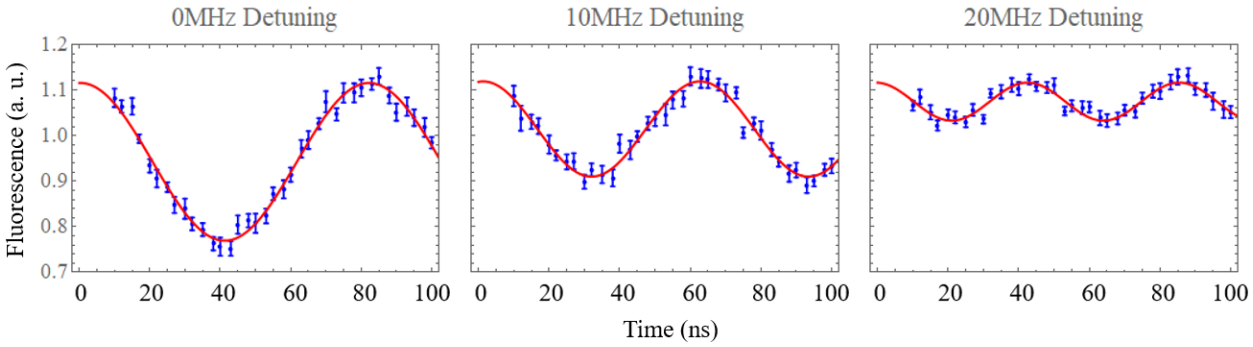

Figure 3.13 Rabi oscillation with different detuned microwave frequency. Red curves are sinusoidal fits. As the detuning increases, the amplitude of Rabi oscillation decreases, the frequency increases and the equilibrium level increases.

Figure 3.13 shows observed Rabi oscillations with different frequency detuning values respectively. The increase in oscillation frequency and equilibrium level and decrease in amplitude is observed as the detuning increases. The fitted parameters are plotted as functions of detuning in Figure 3.14. The results show reasonable agreement with theoretical expectations. To attribute the deviation of Berry phase measurement at $\Delta = 10$ MHz in section 3.3.1 to the error in Rabi frequency of detuned microwave, the error must be 20 % from fittings to our Berry phase data in section 3.3.1. The red crosses in Figure 3.14 mark where the microwave parameters should be at $\Delta = 10$ MHz when the error in Rabi frequency is as large as 20 %. The red crosses are far away from our measured data, especially in fitted frequency. As a result, using a frequency-dependent

microwave amplitude to explain the deviation in Berry phase measurement is not supported by this test experiment of Rabi oscillations.

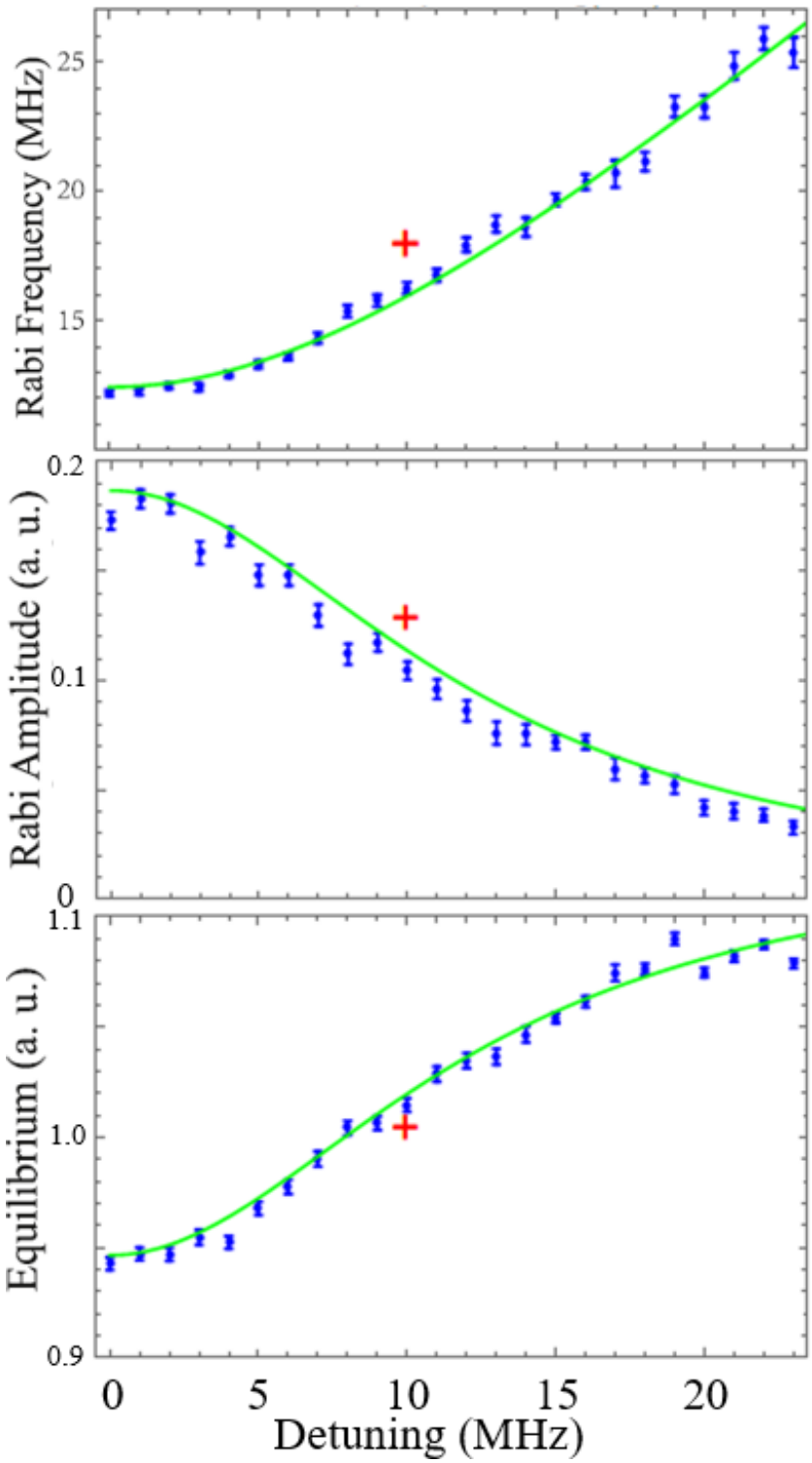

Figure 3.14 Fitted frequency, amplitude and equilibrium position of Rabi oscillations with different detuning values. Green curves are theoretical predictions with fitted parameters from resonant Rabi oscillation measurement. The red cross marks the deviation from theory at $\Delta = 10$ MHz needed to explain the deviation in section 3.3.1.

Another possible reason for the deviation is the transitions between $|0\rangle$ and $|1\rangle$ states. The Berry phase theory is based on adiabatic approximation and the transitions between $|0\rangle$ and $|1\rangle$ states are neglected under adiabatic approximation. Adiabatic condition is verified both theoretically and experimentally. In order to check our adiabaticity experimentally, almost the same waveform as Berry phase experiment ($N = 2$, $\Delta = 5$ MHz and $\Omega = 12.5$ MHz) was used. The only difference is that the first $\frac{\pi}{2}$ pulse and the last $\frac{\pi}{2}$ pulse were removed, as shown in Figure 3.15. If the adiabatic condition is satisfied, the spin should stay in $|0\rangle$ state before the π pulse and in $|1\rangle$ state after. The probability in $|0\rangle$ state at the end of the sequence should be close to 0. This probability is plotted as a function of ramping up/down time T_a and as a function of cyclic period T in Figure 3.16.

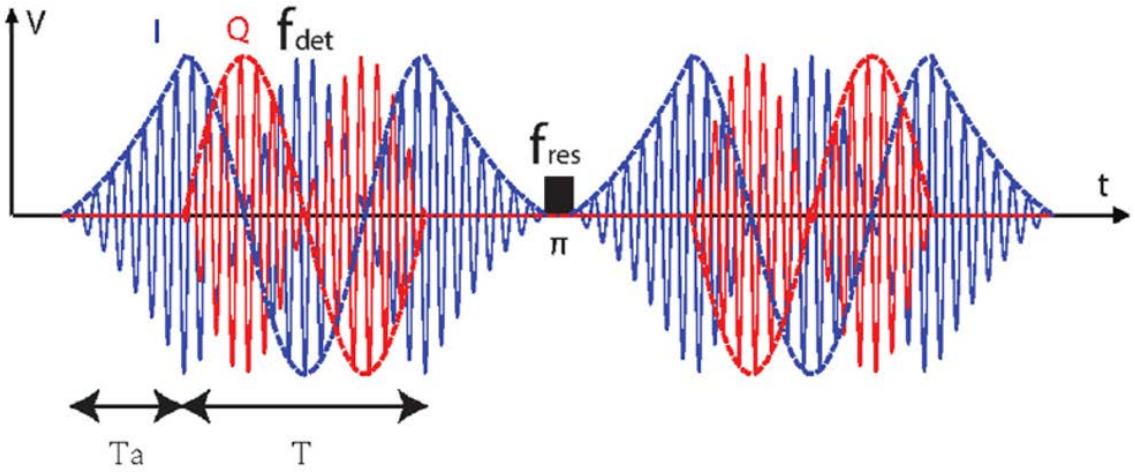

Figure 3.15 Microwave sequence for adiabaticity-checking experiment. Without the first $\pi/2$ pulse, the qubit stays in the $|0\rangle$ state in the first half, and flipped to the $|1\rangle$ state in the second half.

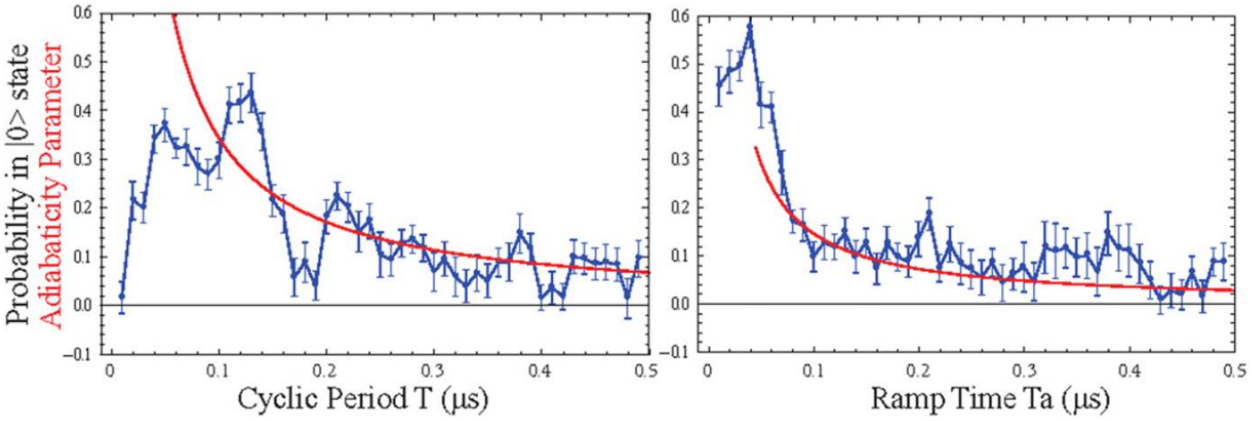

Figure 3.16 Probability in $|0\rangle$ state as functions of cyclic time and ramping time. $\Delta = 5$ MHz and $\Omega = 12.5$ MHz. Red curves are calculated adiabaticity parameter.

The adiabaticity parameters are also calculated and shown in Figure 3.16 for both the ramping and cyclic processes as

$$A = \begin{cases} \dfrac{1}{2\Delta T_a}\sqrt{\dfrac{\Omega^2}{\Delta^2+\Omega^2}}, & (Ramping) \\ \dfrac{\frac{2\pi}{T}\Omega}{2(\Delta^2+\Omega^2)}, & (Cycling) \end{cases} \tag{3.12}$$

We use $T_a \geq 0.35$ μs and $T \geq 0.8$ μs in all Berry phase experiments, and the detuning is set to $\Delta = 10$ MHz or above in all Berry phase experiments. Both the measured transition probabilities and calculated adiabatic parameters verify that the Berry phase experiments are performed in an adiabatic regime.

The IQ modulator is the key part in our Berry phase experiment as the adiabatic cycling motion of the effective magnetic field is controlled through the IQ modulator. The schematic drawing of an IQ modulator is shown in Figure 3.17. The IQ modulator consists of a $\frac{\pi}{2}$ phase shifted power splitter, two mixers and a combiner. By controlling the input signal V_i and V_q, the IQ modulator can be used in amplitude modulation and phase modulation.

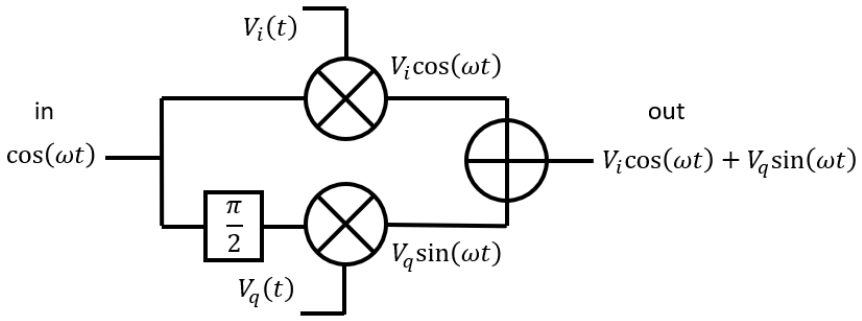

Figure 3.17 Schematic drawing of an IQ modulator. The IQ modulator consists of a $\pi/2$ phase shifted power splitter, two mixers and a combiner. It is capable of doing amplitude modulation and phase modulation.

The imperfection in this modulator could play an important role in distortions of the closed loop in parameter space. Single channel nonlinearity is the imperfection that the output microwave amplitude is not fully linear to the controlled voltage in either I or Q channel. The test experiment is based on resonant Rabi oscillation. The microwave is sent through the IQ modulator with different DC voltage input for I channel and 0 input for Q channel. The Rabi oscillation is expected as

$$S = \cos(V_i \Omega t) + C$$

where V_i is the normalized DC input for I channel. In our test experiment, the pulse length t in fixed to $100\,\mathrm{ns}$, and the maximum microwave Rabi frequency is set to $\Omega = 12.5\,\mathrm{MHz}$. The measured fluorescence as a function of normalized modulation voltage is shown in Figure 3.18.

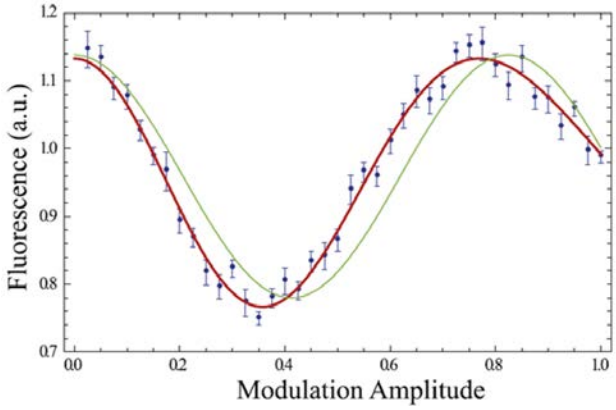

Figure 3.18 Rabi signal with fixed pulse length 100 ns at varying input voltage for I channel of IQ modulator. Green curve is the theoretical expectation without single channel nonlinearity and red curve is fit function with single channel nonlinearity.

Noticing a deviation from the theoretic expectation (green curve), the data is fitted to the Rabi signal corrected with single channel nonlinearity as

$$S = \cos\left(\left(aV_i + bV_i{}^3\right)\Omega t\right) + C \tag{3.13}$$

The fitted parameters are $a = 1.17$, $b = -0.17$. This effect of single channel nonlinearity results in an increased microwave amplitude, and thus an increased solid angle of the closed loop due to distortion.

An additional source for distortion is amplitude imbalance in I and Q channel, meaning identical control voltage input to I or Q channel ends up with different output microwave amplitude.

3.3.4 Simulations with Corrected Hamiltonian

We performed numerical simulation of out Berry phase experiment for comparison with our experimental data. The microwave sequence is separated into small time steps ($\delta t \ll \frac{1}{\Omega}, \frac{1}{\Delta}$) and the time-dependent Hamiltonian in the rotating frame is approximately constant during each time step. The quantum state will evolve as:

$$|\Psi(t+\delta t)\rangle = exp\left(-i\frac{\hat{H}(t)}{\hbar}\delta t\right)|\Psi(t)\rangle \tag{3.14}$$

Any imperfections in our microwave driving field can be easily taken into account by modifying the Hamiltonian $\hat{H}(t)$. The complete Hamiltonian used in our simulation is

$$\hat{H}(t) = \Delta\hat{S}_z + \Omega\overbrace{(aV_i(t) + bV_i(t)^3)}^{nonlinearty}\hat{S}_x - \Omega\overbrace{\left\{a\left[\underbrace{(1+\varepsilon)}_{imbalance}V_q(t)\right] + b\left[\underbrace{(1+\varepsilon)}_{imbalance}V_q(t)\right]^3\right\}}^{nonlinearty}\hat{S}_y \tag{3.15}$$

with single channel nonlinearity parameters $a = 1.17$, $b = -0.17$, and amplitude imbalance between I and Q channel $\varepsilon = 10$ % (0.8 dB in microwave power).

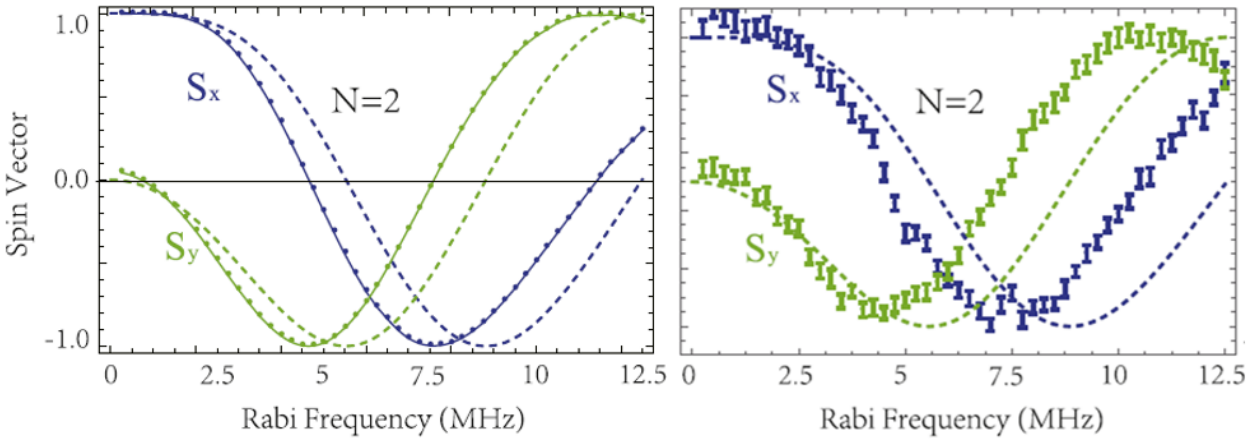

Figure 3.19 Comparison of simulation (left) and experimental data (right) of Berry phase measurement in varying Rabi frequency. The simulation is based on Hamiltonian corrected with single channel nonlinearity and IQ imbalance. Dashed lines are theoretical predictions with ideal driving field.

Figure 3.19 shows the simulation results of our Berry phase measurement in varying Rabi frequency of detuned microwave at fixed detuning $\Delta = 10$ MHz, as shown in section 3.3.1. The deviation from the ideal situations recovers the deviation of our data from theory. Figure 3.20 summarizes the comparison for different numbers of cycles among our experimental data, theoretical predictions for ideal situations and simulations with corrected Hamiltonian.

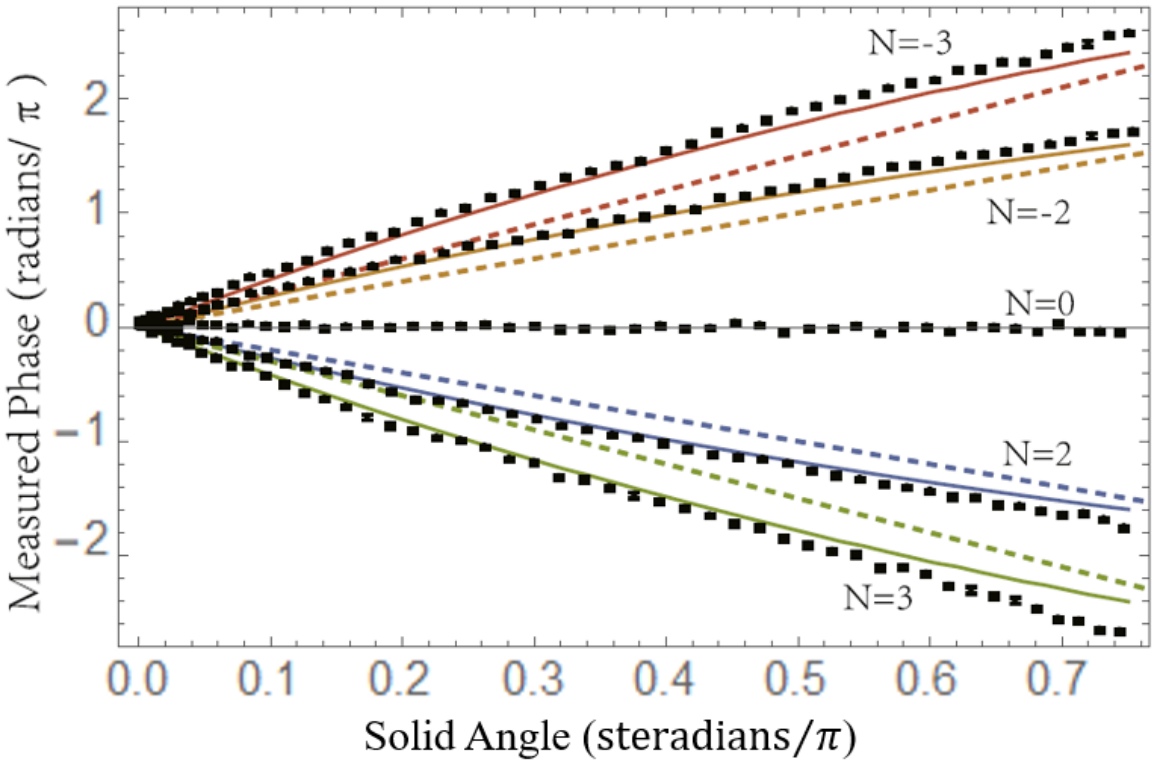

Figure 3.20 Plot of the measured phase against the calculated solid angle based on varying Rabi frequency. The data points are the same as in Figure 3.10. Straight dashed lines with slope ± 2, ± 3 are theoretical predictions as the net phase proportional to solid angle. Solid curves are simulations based on Hamiltonian corrected with single channel nonlinearity and IQ imbalance.

3.4 DISCUSSIONS OF DEPHASING

In this section the decay of Berry phase signal is discussed in detail. As the robustness of geometric phase against certain types of error is one of the motivations of exploring geometric phase, the dephasing of measured phase signal needs to be understood better.

3.4.1 Dephasing in Our Berry Phase Experiment

In the Berry phase experiment in varying cycle number (section 3.3.2), an obvious decay in signal in observed when the number of cycles increases, as shown in Figure 3.12. Based on the measured

phase in section 3.3.2, the calculated gate fidelity[11] for multiple operations of the $\pi/2$ phase gate is shown in Figure 3.21 [90]. Note that the gate fidelity rapidly approached the classical limit $F = 2/3$ for a single qubit gate after ~ 10 repetitions.

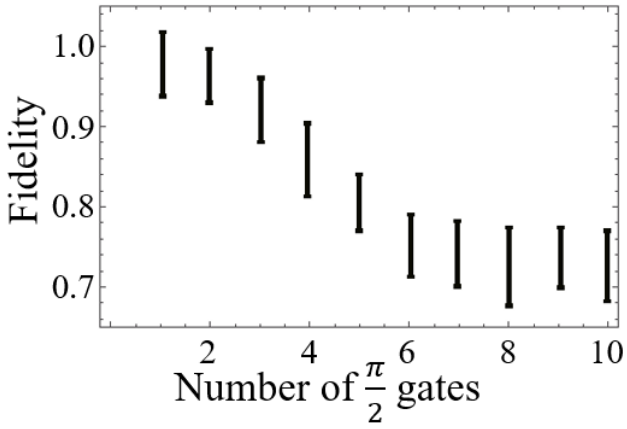

Figure 3.21 Gate fidelity of $\pi/2$ phase gates based on Berry phase. The fidelity is calculated based on our experimental data in section 3.3.2. The error bars are calculated with error transfer formula from the error in measured phase when the phase is extracted from the spin vectors in Figure 3.12.

It is briefly mentioned in section 3.3.2 that random errors in microwave parameters leads to a random solid angle under normal distribution, and to the decay in signal as $\sim exp\left(-\frac{N^2}{N^{*2}}\right)$. We call this model *Geometric Dephasing* [76]. Both the random errors in microwave amplitude (Ω) and resonant frequency (Δ) contribute to the random error in the corresponding solid angle.

The random error in resonant frequency, or the frequency detuning Δ, is due to the fluctuation in Larmor frequency of our spin qubit instead of our microwave sources, because the microwave synthesizers take our atomic clock frequency standard as reference and are accurate down to sub-Hz. The resonance of our NV centers, on the other hand, could drift up to MHz due to temperature fluctuation, magnetic field instability and mechanical drift of sample mount. The fluctuation in Δ can be characterized with Ramsey experiment. As mentioned in section 2.4.3, the Ramsey signal decays as

$$S = \cos(|\gamma_e|B_1 t)\, e^{-\frac{t^2}{T_2^{*2}}} \tag{3.16}$$

[11] The gate fidelity F_U of gate U is calculated as the average probability of getting an expected quantum state when the initial state is $|\pm x\rangle$, $|\pm y\rangle$ and $|\pm z\rangle$. $F_U = \frac{1}{6}[Pr(U|+x\rangle) + Pr(U|-x\rangle) + Pr(U|+y\rangle) + Pr(U|-y\rangle) + Pr(U|+z\rangle) + Pr(U|-z\rangle)]$.

In fact, the decay in signal of Ramsey experiment can be explained with a normal-distributed random error in the frequency detuning, σ_Δ. The relation between σ_Δ and the inhomogeneous dephasing time, T_2^*, of the NV center is given by

$$\sigma_\Delta = \frac{\sqrt{2}}{T_2^*} \tag{3.17}$$

The result of Ramsey experiment is shown in Figure 3.22. The fitting to the data (red curve) shows the inhomogeneous dephasing time as $\sim 0.78 \pm 0.04$ μs.

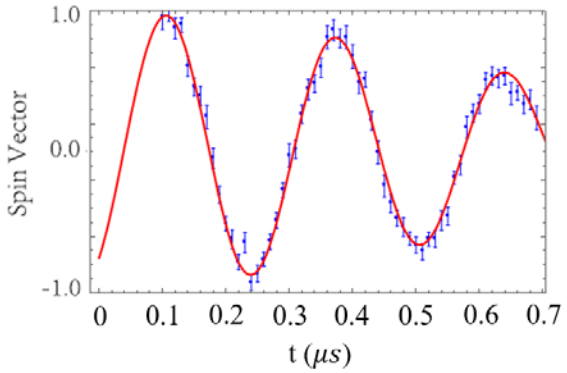

Figure 3.22 Ramsey experiment with frequency ~3.7 MHz and inhomogeneous dephasing time $\sim 0.78 \pm 0.04$ μs. Red solid curve is the fit function considering the dephasing. More details of Ramsey experiments are in section 2.4.3 and Appendix A.5.

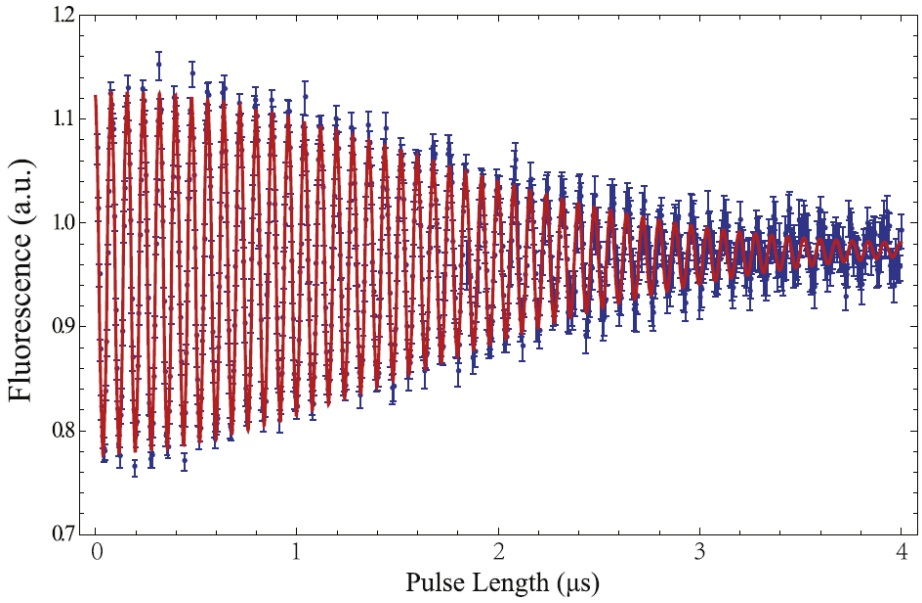

Figure 3.23 Rabi oscillation decay for long pulse lengths. Red curve is the fitting to the data with exponential of $-t^2$ decay factor. The fitting to the decay gives the value of T_ρ as $\sim 2.21 \pm 0.03$ μs. The decay is due to fluctuations in our microwave field strength.

On the other hand, the random error in microwave amplitude, or Rabi frequency Ω, can be characterized with Rabi oscillation. The same as the error in Δ, we assume a normal-distributed random error in the Rabi frequency, σ_Ω. The Rabi oscillation will decay the same way as Ramsey oscillation decays due to this random error.

$$S = \cos(\Omega t)\, e^{-\frac{t^2}{T_\rho^2}} \tag{3.18}$$

The time scale of the decay is characterized as T_ρ, with the relation to σ_Ω as

$$\sigma_\Omega = \frac{\sqrt{2}}{T_\rho} \tag{3.19}$$

The decay of Rabi oscillation is observed at long pulse lengths as shown in Figure 3.23. The fitting to the decay gives the value of T_ρ as $\sim 2.21 \pm 0.03$ μs.

Given T_ρ and T_2^*, *the* σ_Ω and σ_Δ can be calculated and the standard deviation in corresponding solid angle Θ is calculated as

$$\sigma_\Theta = \left|\frac{\partial \Theta}{\partial \Omega}\right| \sigma_\Omega + \left|\frac{\partial \Theta}{\partial \Delta}\right| \sigma_\Delta \tag{3.20}$$

The decay parameter N^* is

$$N^* = \frac{1}{\sqrt{2}\pi\sigma_\Theta} \tag{3.21}$$

and can be estimated as $N^* \sim 4 \times 10^2$, much larger than measured value $N^* = 14$. This suggests the geometric dephasing should only occur at much larger number of cycles and is not the source of the decay shown in section 3.3.2. There are other sources of decay responsible for the decay observed in our experiment.

The way we isolate the geometric phase from the trivial dynamic phase is using a spin echo sequence with symmetric waveform to cancel the dynamic phase accumulated in the two halves. This method, however, requires identical dynamic phase accumulated in both halves, which is not trivial to achieve. The dynamic phase accumulated is given by

$$\beta_D = \int_0^t \sqrt{\Omega^2 + \Delta^2}\, dt \tag{3.22}$$

We kept our microwave parameter Ω and Δ constant during the experimental sequence, so the dynamic phases in both halves are identical and will cancel each other in ideal cases. Nevertheless, any fast fluctuations that behave differently in the two halves of spin echo will cause a difference in dynamic phases accumulated, and as a result, a random residual of dynamic phase after the

cancellation was left in our measured phase. The random residual of dynamic phase will cause dephasing in our measured Berry phase signal, as we call it *Dynamic Dephasing.*

The effect of dynamic dephasing is experimentally tested. The experimental sequence is shown in Figure 3.24 left. Similar to Berry phase experiment, a detuned microwave is applied in both halves of spin echo with adiabatic ramping up and down. Instead of performing phase modulation of the detuned microwave to rotate the effective magnetic field, the control voltages to the IQ modulator are kept constant, corresponding to a constant effective magnetic field. The closed path of effective magnetic field in parameter space is a straight line back and forth, shown in Figure 3.24 right, with zero solid angle towards the origin. There is no geometric phase involved in this test experiment, and the dynamic phase should be cancelled just as in the Berry phase experiment because the Hamiltonians in two halves of spin echo are the same.

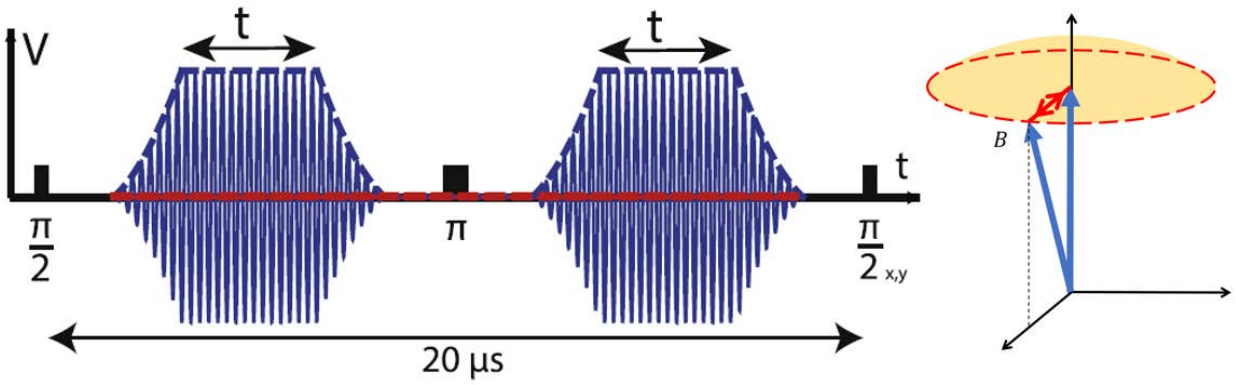

Figure 3.24 Experimental sequence for dynamic dephasing test and the corresponding closed path of effective magnetic field in parameter space. Instead of performing phase modulation of the detuned microwave to rotate the effective magnetic field as in our Berry phase experiments, the control voltages to the IQ modulator are kept constant, corresponding to a constant effective magnetic field during the time t.

However, as we scan the time the effective magnetic field is kept still (marked as t in Figure 3.24 left), the dynamic dephasing shows up. As shown in Figure 3.25, the measured signal decays when the time t increases. This decay is dynamic dephasing due to the random residual of dynamic phase that is not canceled by the spin echo sequence and geometric phase is not involved in this experiment at all. This dynamic dephasing effect matches the decay observed in Berry phase experiment in time scale, and it is believed that the decay of signal in section 3.3.2 is due to dynamic dephasing.

As mentioned above, the source for dynamic dephasing could be fast fluctuations in microwave parameter Ω and Δ. Because all of our Berry phase experiments are done in a time scale

$\tau \ll T_2$, where T_2 is the coherence time of NV center, the fast fluctuation in Δ should be negligible. As a result, we attribute the dynamic dephasing of our Berry phase experiment to the effect of fast fluctuations in microwave amplitude Ω. To improve the fidelity of phase shift gates based on Berry phase, better control of fast fluctuations in microwave power must be achieved.

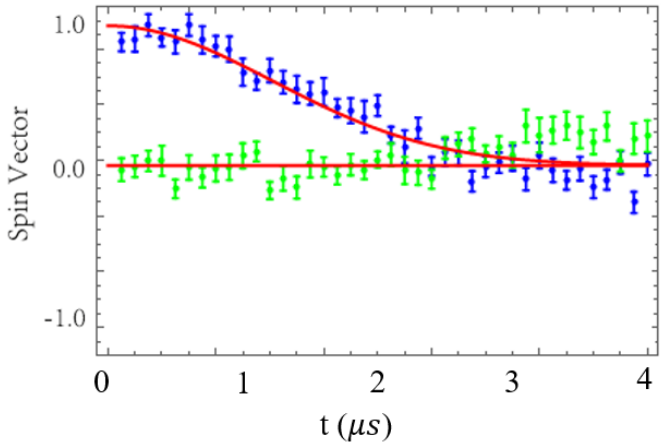

Figure 3.25 Data from dynamic dephasing experiment, with pulse sequences shown in Figure 3.24. Blue and green data points are measured S_x and S_y, respectively. Red curves are fits to Gaussian decay.

3.4.2 The Connection of Geometric Phase and Dynamic Phase

The effect of dynamic dephasing showing up in geometric phase measurement is important and encourage me to explore the intrinsic relation between geometric phase and dynamic phase. And more importantly, the influence of this dynamic dephasing effect on other potential applications of geometric phase needs to be better understood.

Geometric phase is introduced as a correction term to the dynamic phase. As a correction term, geometric phase is always accompanied with the main term, the dynamic phase. To isolate geometric phase from dynamic phase, the only way is to cancel the dynamic phase with spin echo or similar methods, which requires accurate control of the dynamic phase. Another approach trying to circumvent this problem is to work with degenerate states and non-abelian geometric phases, where the dynamic phase vanishes. However, keeping the states ideally degenerate also requires accurate control of the Hamiltonian. Although geometric phase itself is robust against certain type of errors [89], it's meaningless if the accompanying dynamic phase is not, as the fluctuations in

the residual of dynamic phase add directly to the net phase being measured. While geometric phase is less prone to errors or fluctuations than dynamic phase, unless the dynamic phase can be canceled perfectly or is completely absent (as in ideal non-abelian geometric phases), the quantum phase will still have errors.

Looking at the geometric phase from a different angle gives us insight to the essence of geometric phase. For simple cases when the geometric phase accumulates linearly in time, the exact solution of the Schrödinger Equation can be calculated by going into another reference frame. This "*provides a particularly physical interpretation of the adiabatic arguments underlying the geometric phase*" [91]. In particular, such interpretation may be important for recent topics like adiabatic and holonomic quantum computation.

As shown in Appendix A.7, the dynamic phase of an eigenstate is defined by integrating instantaneous Hamiltonian over time,

$$\beta_D = -\frac{1}{\hbar}\int_{t_0}^{t} E(t)dt \tag{3.23}$$

where $E(t)$ is the instantaneous eigenvalue of the time-dependent Hamiltonian $H(t)$. As mentioned in section 3.1, the dynamic phase accumulated by a spin-$\frac{1}{2}$ particle in a slowly varying periodic magnetic field during one cycle is in equation 3.1,

$$\beta_D = \gamma_s \int_0^T B(t)dt$$

However, the actual phase the quantum system accumulates during one cycle consists of not only the dynamic phase, but the geometric phase as well. According to Berry's theory, this geometric phase can be calculated as

$$\beta_G = i\oint_C \langle\psi_m(\vec{R})|\nabla_{\vec{R}}|\psi_m(\vec{R})\rangle \cdot d\vec{R} \tag{3.24}$$

which is a time-independent function which depends only on the geometric path of the Hamiltonian in the parameter space [82].[12]

In our case, the experiments are described in a rotating frame. To avoid confusion, it is preferable to take one step back and review the background of rotating frame. As mentioned in section 2.4.1 and Appendix A.3, using the transform

[12] See Appendix A.7 for details.

$$\left|\tilde{\psi}(t)\right\rangle = R_z(-\omega_{ref}t)|\psi(t)\rangle \tag{3.25}$$

with the effective Hamiltonian $\tilde{H}(t)$, the dynamics of our system (NV center as a qubit) in the rotating frame is identical to the dynamics of a spin-$\frac{1}{2}$ particle in the lab frame. The definition of dynamic phase of our system in a rotating frame is the same as the definition above, except that the $E(t)$ is the instantaneous eigenvalue of the time-dependent effective Hamiltonian $\tilde{H}(t)$ in a rotating frame.

$$\tilde{\beta}_D = -\frac{1}{\hbar}\int_{t_0}^{t} E(t)dt = -\frac{1}{\hbar}\int_{t_0}^{t} \langle\tilde{\psi}_{m,t}|\tilde{H}(t)|\tilde{\psi}_{m,t}\rangle dt \tag{3.26}$$

For our system with effective Hamiltonian $\tilde{H}(t)$ in a rotating frame, the geometric phase in the rotating frame can be calculated, using exactly the same mathematics, as a time-independent function which depends only on the geometric path of the effective Hamiltonian $\tilde{H}(t)$ in the parameter space

$$\tilde{\beta}_G = i\oint_C \left\langle\tilde{\psi}_m\left(\vec{\tilde{R}}\right)\right| \nabla_{\vec{\tilde{R}}} \left|\tilde{\psi}_m\left(\vec{\tilde{R}}\right)\right\rangle \cdot d\vec{\tilde{R}} \tag{3.27}$$

where the parameter $\vec{\tilde{R}}$ sets the effective Hamiltonian as $\tilde{H}(t) = \tilde{H}\left(\vec{\tilde{R}}(t)\right)$. For our NV center system, as described in section 2.4.1, $\vec{\tilde{R}} = (\Omega_x \quad \Omega_y \quad \Delta)$ is a vector in the 3-dimentional parameter space, which can be treated as an effective magnetic field. Similar to the example of a spin-$\frac{1}{2}$ system under a time-dependent magnetic field discussed in Appendix A.7, using Stokes' theorem, the geometric phase can be calculated as

$$\tilde{\beta}_G = \pm\frac{\Theta_{\tilde{C}}}{2} \tag{3.28}$$

where $\Theta_{\tilde{C}}$ is the solid angle of the contour $\tilde{C}$ in the 3-dimentional parameter space.

When describing a physical process, different choices of rotating frame ω_{ref} lead to different effective Hamiltonian $\tilde{H}(t)$ in that frame, which results in different geometric path of $\vec{\tilde{R}}$ in parameter space and different geometric phase in that rotating frame. On the other hand, different choices of rotating frame lead to different dynamic phase as well, due to different effective Hamiltonian $\tilde{H}(t)$ in that frame. Overall, the sum of dynamic phase and geometric phase is consistent in different rotating frames.

Our Berry phase experiment is a good example. The geometric phase accumulation happens during the microwave phase modulation, corresponding to the rotation of effective magnetic field in parameter space. The effective Hamiltonian in the rotating frame is

$$\tilde{H} = \Delta S_z + \Omega R_z(\phi) S_x R_z(-\phi)$$

where $\Delta = \omega_L - \omega_{det}$ and the phase of microwave increases as

$$\phi = \frac{2\pi}{T} t$$

The ramping up and down processes have no contribution to geometric phase accumulation. They are used for maintaining adiabaticity of the whole sequence. During phase modulation, the phase of microwave varies linearly in time, which is equivalent to shifting the frequency of microwave by $\frac{2\pi}{T}$, where T is defined as the period of rotation in section 3.3.3.

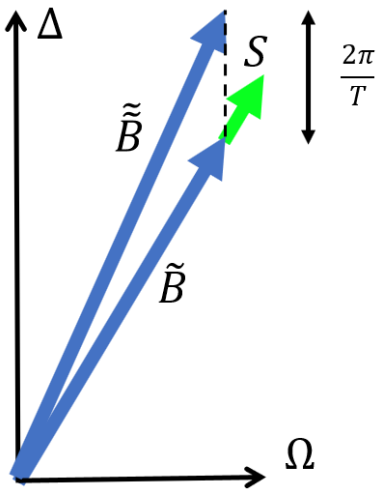

Figure 3.26 Effected magnetic field in rotating frame with shifted frequency. The magnetic field B is the effective magnetic field in the original reference frame. S is the spin vector. B' is the effective magnetic field in the new frame.

Now we choose a different rotating frame that rotates at the shifted frequency. The transformation from the state in the original rotating frame to the state in the new frame is defined as

$$\left|\tilde{\tilde{\psi}}(t)\right\rangle = R_z\left(\frac{2\pi}{T}t\right)\left|\tilde{\psi}(t)\right\rangle = R_z\left(-\omega_{det}t + \frac{2\pi}{T}t\right)|\psi(t)\rangle \tag{3.29}$$

And the effective Hamiltonian in the new rotating frame changes to

$$\tilde{\tilde{H}} = \left(\Delta + \frac{2\pi}{T}\right) S_z + \Omega S_x \tag{3.30}$$

This effective Hamiltonian is a static Hamiltonian and thus there is no geometric phase accumulated. To picturize the new effective Hamiltonian, as the frequency detuning Δ shifted by $\frac{2\pi}{T}$, the effective magnetic field changes from B to B', and stays constant during the phase modulation, shown in Figure 3.26. The initial spin state is aligned (parallel in Berry's theoretical work, but perpendicular in our experiment) with the effective magnetic field before (green arrow in Figure 3.26). The change in direction of effective magnetic field results in precession of spin about the new axis. But this precession can be neglected because the change in direction of effective magnetic field is small. This approximation corresponds to the adiabatic approximation in Berry phase picture, which claims the transition between the instantaneous energy eigenstates is negligible. On the other hand, the change in magnitude of effective magnetic field is not negligible. The dynamic phase accumulated during time T under this new rotating frame is

$$\tilde{\tilde{\beta}}_D = \int_0^T \sqrt{\Omega^2 + \left(\Delta + \frac{2\pi}{T}\right)^2}\, dt = T\sqrt{\Omega^2 + \left(\Delta + \frac{2\pi}{T}\right)^2}$$

where $\frac{2\pi}{T} \ll \Omega, \Delta$. Taking first order approximation, the dynamic phase during time T can be written as

$$\tilde{\tilde{\beta}}_D = T\sqrt{\Omega^2 + \Delta^2} + \frac{2\pi\Delta}{\sqrt{\Omega^2 + \Delta^2}}$$

After the phase modulation time T we need to switch back to the original rotating frame. Since the new frame rotates more slowly than the original frame by $\delta\omega = \frac{2\pi}{T}$, an additional correction term $-\delta\omega \cdot T = -2\pi$ is added to the phase when switching back to the original frame, which leads to

$$\tilde{\phi} = \tilde{\tilde{\beta}}_D - 2\pi = T\sqrt{\Omega^2 + \Delta^2} - 2\pi\left(1 - \frac{\Delta}{\sqrt{\Omega^2 + \Delta^2}}\right) \tag{3.31}$$

This is exactly the same result with Berry phase picture in the original rotating frame where

$$\tilde{\beta}_D = T\sqrt{\Omega^2 + \Delta^2}$$

$$\tilde{\beta}_G = -\Theta = -2\pi\left(1 - \frac{\Delta}{\sqrt{\Omega^2 + \Delta^2}}\right)$$

This example shows the fact that effect of geometric phase is equivalent to dynamic phase when using a different rotating frame. This better explains the intrinsic connection between geometric phase and dynamic phase, and provides insight into how fluctuations in dynamic phase can affect

geometric phase experiments. A more general problem, spin-*J* particle in a magnetic field, is discussed with both geometric phase idea and exact solution in a rotating reference frame in [91].

If the microwave phase does not increase linearly in time during the phase modulation, the dynamic phase treatment would become much more complicated while the geometric phase picture remains simple. Providing new angles to look at physical processes is the importance of exploring geometric phase, as Anandan pointed out in the conclusion of his review paper [81]: "*Geometric phases and angles provide a unified description of a wide range of phenomena in classical and quantum physics. But their greatest value lies perhaps in giving us a new way of looking at quantum theory.*"

3.4.3 Comments on Publications from Other Research Groups

The pioneering works in geometric phase, including original adiabatic geometric phase by Berry [82], generalization of definition by Aharonov and Anandan [92], and geometric phenomena of light decades before Berry by Pancharatnam [93], are summarized by Anandan in his review paper [81] with insight. As mentioned above, providing new ways of looking at physical processes, geometric phase is still important today for understanding complex quantum mechanical phenomena [94].

One of the most influential publications that brings geometric phase back to researchers' interests is an experimental paper in 2000 by Jones et al [74]. The Berry phase is accumulated and measured in an NMR (Nuclear Magnetic Resonance) apparatus and the spin echo technique to isolate geometric phase from the accompanying dynamic phase is referred to by many publications on Berry phase measurement, including ours [72, 76, 87, 95, 96]. More importantly, the authors suggest taking advantage of the intrinsic robustness of geometric phase towards certain types of errors to improve quantum computation. This suggested application became the most important motivation of many following researches. Unfortunately, they also admitted that they found "*no particular advantage over more conventional methods in NMR quantum computation*" [74]. However, canceling dynamic phase with spin echo sequence is indeed a great contribution to this field.

A theoretical publication came out in 2003 by De Chiara and Palma [89] discussing the effect of fluctuations in control field on Berry phase. The fluctuations are modeled with Ornstein-

Uhlenbeck (OU) process in a much more professional way compared to our work, but the conclusion is the same: the dephasing is dominantly due to fluctuations of the dynamic phase. However, the intrinsic connection between geometric phase and dynamic phase is not emphasized and the method to isolate geometric phase from dynamic phase is not discussed.

In 2007, Leek et al published a paper on Science, reporting observation of Berry phase in a superconducting qubit [76]. This is the first paper in a series from Dr. Wallraff's research group. The Berry phase measurement was brought to solid state system with microwave driving field from NMR apparatus. This is the first measurement of Berry phase in solid state qubits and an important motivation to our work. However, there are some imperfections in this paper. First, the deviation between measured signal and theoretical expectation is not mentioned. The fitted curve in Fig. 3 of the paper matches the theoretical curve at $\Delta = 45$ MHz but they explicitly claimed they were using $\Delta \approx 50$ MHz. A follow-up of this paper is published in 2012 by Berger et al from the same group [95], reporting the deviation and attributing it to the influence of higher excited states. Second, they attributed the dephasing they observed as geometric dephasing, contradictory to the paper by De Chiara and Palma [89] and our results. They cited the paper by De Chiara and Palma for the mathematical form of geometric dephasing without noticing their conclusion that the fluctuations in geometric phase do not contribute considerably to dephasing.

Berger et al published another paper in 2013 discussing the robustness of Berry phase towards different types of noise [96]. After a direct comparison between Berry phase and dynamic phase, they drew a conclusion that the Berry phase is less affected by noise-induced dephasing, which is true but misleading. Berry phase is indeed noise-resilient compare to dynamic phase, but it cannot be experimentally tested because Berry phase is always accompanied by dynamic phase, or residual of dynamic phase after cancellation. A closer look to their experimental details reveals their trick. The random noise in their Berry phase experiment was generated by AWG (Arbitrary Waveform Generator) and carefully controlled to be symmetric about the two halves of spin echo sequence. A symmetric noise in time is not a realistic noise. On the other hand, the noise induced to dynamic phase measurement was not symmetric but truly random. It was not a fair comparison.

In 2013, Abdumalikov Jr et al from Dr. Wallraff's research group published an experimental paper in Nature [78], reporting experimental realization of non-Abelian non-adiabatic geometric gates, which were originally proposed by Sjöqvist et al in 2012 [77]. The non-Abelian non-adiabatic geometric phase is very different from Abelian adiabatic geometric phase,

or Berry phase. However, the statement "*geometric phase is always accompanied by dynamic phase*" remains true, as the correction term is always accompanied by the main term. There is no way to isolate geometric phase from dynamic phase without accurate control of dynamic phase. In the theoretical proposal [77], it is pointed out that the pure geometric gates are realized "*by choosing time-independent* ω_0 *and* ω_1 *over the duration of the pulse and by tuning the laser frequencies so that the detunings* Δ_0 *and* Δ_1 *vanish.*" In other words, the dynamic phase is carefully controlled to be zero by accurate control of Ω and Δ (technically it is the ratio between amplitudes of two driving fields $\frac{\Omega_0}{\Omega_1}$ that needs accurate control). Abdumalikov Jr et al admitted that the dynamic contributions are the major limiting factor for gate performance and discussed dynamic dephasing in supplementary information.

The same experiment is brought to NV centers in 2014 by Zu et al [80], and by Arroyo-Camejo et al [79] when we were in preparation of our paper after we finished data-taking of Berry phase experiment. The same argument goes for this paper that it requires accurate control in detunings Δ_0 and Δ_1, and the ratio between amplitudes of two driving fields $\frac{\Omega_0}{\Omega_1}$ to eliminate the dynamic phase. The fidelity reported is much higher than our work [72], which is not surprising because non-adiabatic gates are run in very short time scale that there is no time for phase error accumulation.

In fact, the robustness of non-Abelian non-adiabatic geometric gates proposed by Sjöqvist et al is studied in another paper from the same group by Johansson et al in 2012 [97]. The conclusion is the dephasing can be avoided by using extremely short gate time. However, short gate time means large Ω and Δ, which leads to large errors in Ω and Δ, assuming the percentage error unchanged. As a result, there is no advantage of non-Abelian non-adiabatic geometric gates over conventional dynamic phase gates under the same accuracy of control field parameters.

An interesting paper with geometric phase in NV centers worth noticing is published on Europhysics Letters in 2011 by Rong et al [98]. The topic is using dynamic decoupling to enhance phase estimation, but they used Aharonov-Anandan phase (AA phase, or non-adiabatic geometric phase) as the phase signal to be estimated. Actually, the phase is generated just by two microwave π pulses with different phases, which is easily understood as dynamic phase in conventional Bloch sphere picture. However, this conventional dynamic phase is interpreted as non-adiabatic

geometric phase when looking from the authors' angle. This is another example of the connection between geometric and dynamic phase depending on the frame.

3.5 CONCLUSION

We present measurement of Berry phase with a single NV center in diamond. The spin qubit is manipulated geometrically by applying microwave radiation that creates a rotating effective magnetic field, and the resulting Berry phase signal is observed by cancelling out the dynamic phase with spin echo sequence. The study on dephasing shows that the dynamic dephasing results from fast fluctuations in control field is responsible for the decay of signal. Since the geometric phase is intrinsically connected to dynamic phase when we transform between different rotating frames, geometric phase cannot be experimentally isolated from dynamic phase without extremely accurate control of the driving fields.

4.0 TOWARDS SCANING DIAMOND PROBE MICROSCOPE

This chapter shows the effort spent on realization of scanning probe microscope (SPM) with diamond probe and single NV centers used for high-resolution magnetic imaging experiments.

4.1 INTRODUCTION: SCANNING DIAMOND PROBE MICROSCOPE

As described in chapter 1, NV centers are atomic scale sensors which can potentially image magnetic field in sub-nanometer resolution. A scanning probe scheme for magnetic imaging based on optically detected magnetic resonance (ODMR), combining scanning probe microscope (SPM) and optical addressing of sensing spins, is proposed in 2005 [99], and experimentally realized with NV centers in 2008 [15].

The principle of magnetic imaging with NV centers is a scanning probe microscope (SPM) with a diamond probe containing NV center, and an integrated confocal microscope for optical addressing NV center. There are two configurations for the confocal-integrated SPM. An easier one is to place the objective for the confocal microscope at the opposite side of the sample to the diamond tip (inverted configuration), where the confocal microscope looks through the sample to see the diamond tip [15]. This requires the magnetic sample to be thin and optically transparent. The other one is to place both the objective and diamond tip at the same side of the sample, which requires a long working distance of the objective [100]. Engineering the diamond probes with NV centers has been achieved in two different ways. The most straightforward one is by grasping a diamond nanocrystal at the apex of a typical AFM (atomic force microscope) tip. This requires the inverted configuration and thus thin and transparent samples [15]. The much more complicated way is to fabricate a diamond chip with a tip containing NV center, and attach it to the SPM probe [43].

Because of the compatibility to general magnetic samples, the same-side configuration and the fabricated diamond tip is more attractive to us for most applications in magnetometry. Because of the position control of NV centers at the tip, and the relatively long coherence time of NV centers, fabricated diamond tips from a high-quality diamond sample with implanted NV centers are preferred to realize the full potential of NV center magnetometry. Nevertheless, due to the difficulty in fabrication processes, only a handful of research groups reported successful in implementation of the scanning diamond probe microscope (SDPM) [43, 101, 102].

4.2 DESIGNING DIAMOND PROBE COMPATIBLE SPM

The original design of our SDPM setup was aiming for sub-nanometer resolution of magnetic imaging in ambient condition. This ambitious design includes two separate 3-axes nano-stages for accurate position control of both the sample and the diamond probe, a coarse sample stage, and a motorized stage for tip approaching.

The SPM with optical feedback is not appropriate for our application because we need free space for optical access to the diamond probe for integration of confocal microscope. The tuning fork feedback SPM [103] can be integrated with our confocal microscope by using an objective with long working distance, at the cost of numerical aperture (NA). Figure 4.1 shows the drawing of our setup design based on the SPM model from Mad City Labs Inc. The SPM can be setup in either inverted configuration or same-side configuration, as the center aperture for optical access is free from both top and bottom. The SPM setup in Figure 4.1is in inverted configuration, where the objective is at the bottom side. In the same-side configuration (not shown) the objective will block our vision of the tuning fork and sample stage.

Considering the magnetic field sensitivity of single NV centers, sensing magnetic field due to nuclear spins takes time. It was estimated the magnetic imaging of nuclear spins takes $\sim$10 min/pixel. This requires long time stability of our SPM setup. Acoustic drifts and thermal drifts, as the most common drifts in SPM system, are taken into account. The effect of acoustic drifts can be minimized by shielding the entire setup with an acoustic hood, and the effect of thermal drifts can be minimized by choosing CTE-matching (coefficient of thermal expansion)

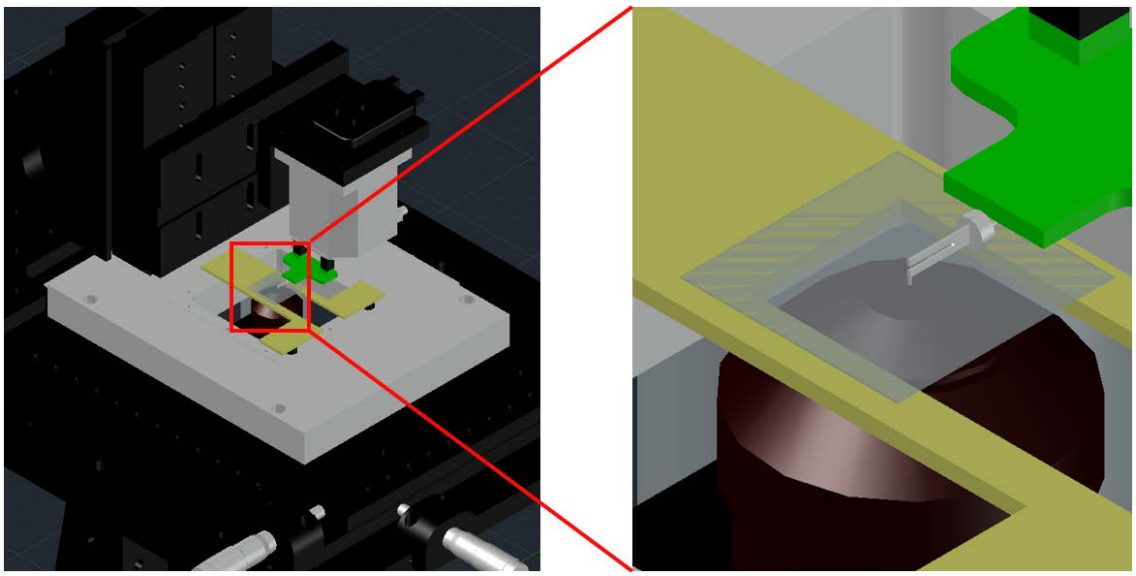

Figure 4.1 Realistic drawing of our SPM system in the inverted configuration. Black blocks are coarse positioning stages and adapters. Silver blocks in the middle are 3-axes nano stages for sample positioning and tip positioning.

materials for the whole SPM. As shown in Figure 4.2, along the geometric contour from the tip to the sample, it is desired the materials have the same CTE as much as possible. Except for the PCB board shown as green and yellow, all other stages and mounts are made of aluminum, in order to match the aluminum nanopositioning stages purchased from Mad City Labs Inc..

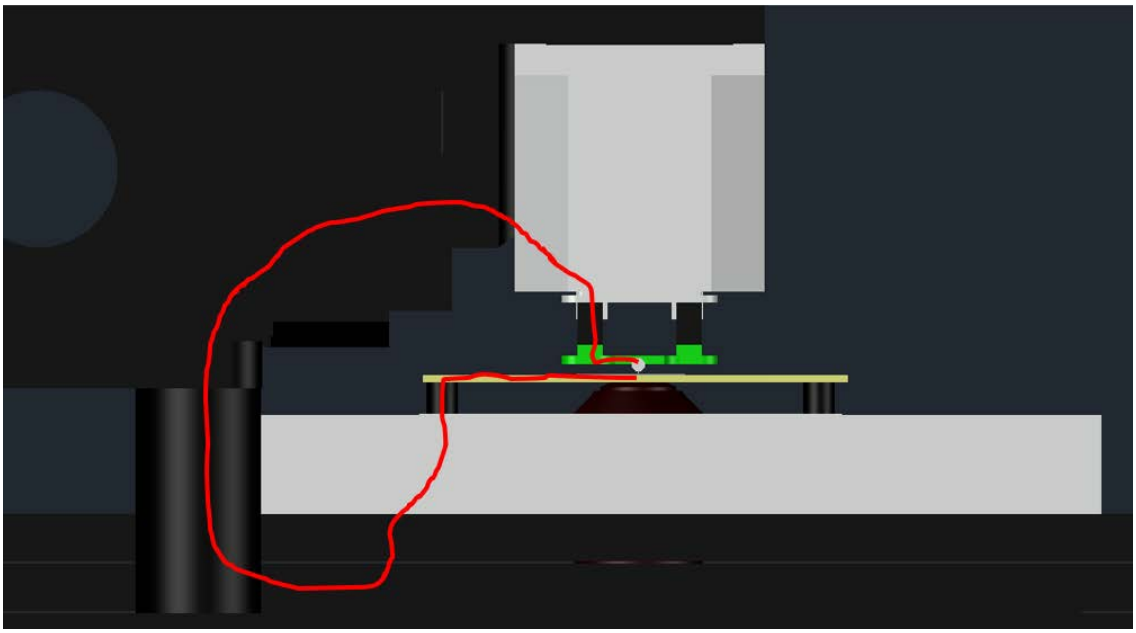

Figure 4.2 Side view of SPM design. The red curve marks the geometric contour from the tip to the sample. The geometric contour of the SPM is the shortest path from the tip to the sample. It passes through the minimum number of solid pieces on the path.

4.3 DIAMOND PROBE FABRICATION

Diamond probe fabrication is the key technique to the magnetic imaging setup with NV centers. The first fabricated diamond probe with a single NV center at the tip is reported in 2012 [43]. The fabrication recipe is inherently complicated.

As the detailed recipe can be found in [104], the complete procedure is briefly introduced by three stages shown in Figure 4.3. The first stage is the sample preparation stage when a diamond membrane sample with a layer of shallowly implanted NV centers is prepared for fabrication. In the second stage, the diamond probes with NV centers at the tip are fabricated using the prepared membrane with lithography and plasma etching. The last stage is the assembling stage where the fabricated diamond probes are selectively picked up and attached to the AFM probe.

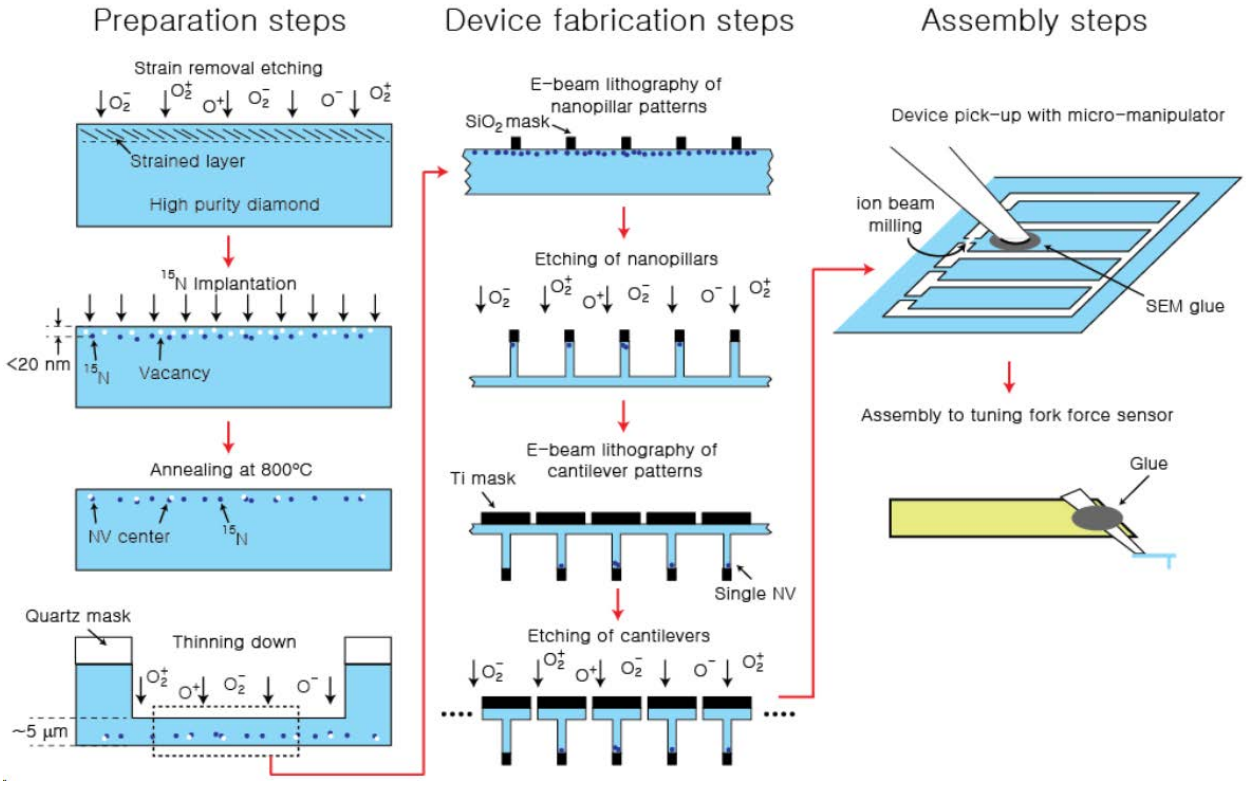

Figure 4.3 Reproduced with permission from [104]. Diamond probe fabrication procedure. The whole procedure can be divided into three stages: preparation, fabrication and assembly.

In the sample preparation stage, we start with a high-purity single-crystalline diamond slab grown in CVD (chemical vapor deposition). The diamond slabs are commercially available at Element Six Ltd with nitrogen concentration less than 5 ppb. These diamond slabs can be sliced into thin layers of tens of micrometers and polished at Delaware Diamond Knives Inc. After the slicing, there are polishing marks remaining at the surface. In order to avoid these strained layers, the first few micrometers diamond at the surface are removed by plasma etching with oxygen plasma, leaving a strain-free smooth diamond surface. Commercial ion implantation of nitrogen is then applied to the diamond sample with proper energy and dose. A following annealing process makes the vacancies from the implantation damages mobile and forms NV centers when trapped by nearby implanted nitrogen ions. To remove the graphitized layer at diamond surface, the sample is cleaned by boiling mixture of sulfuric, nitric and perchloric acids. Finally, the diamond slab is further thinned down to a few micrometers by plasma etching from the back side.

In the second stage, the diamond sample is patterned with arrays of dots in EBL (electron beam lithography) and evaporator if deposition of metal is needed. The dots on the diamond surface are used as etching masks in the plasma etching. The oxygen plasma etching then creates the arrays of nanopillars containing NV centers. The shape of cantilevers are patterned on the other side of the diamond sample. With the similar lithography-etching process from the back side, arrays of cantilevers with single tips are fabricated.

Before the last stage of picking up, the fabricated probes on-chip is characterized under the confocal microscope. Only those probes with single NV centers at the tip are usable. To pick up the good probes, a micropipette with glue is brought to the chosen probed and release the probe from the diamond chip after the glue fuses. And the micropipette is then glued to the AFM probe or tuning fork.

This recipe requires advanced fabrication and characterization techniques at nanometer scale and successfully accomplished by only a few groups. These groups kept simplifying this procedure till recently. For example, to increase the fabrication efficiency, instead of fabricating one tip on each diamond probe, an array of tips is fabricated on the same probe [101]. The assembly stage is simplified without using FIB (focused ion beam) to break the pipet [102]. And commercial diamond membranes without etching a thick layer of diamond helps to simplify the preparation stage [105]. There are some techniques indispensable to the recipe including nanoscale patterning with EBL, and plasma etching of diamond with reactive ion etcher (RIE).

The challenge of EBL patterning on diamond is from the diamond sample. Diamond is a very good insulator which is not a proper sample for scanning electron microscope (SEM). The sample is charged up where exposed to the electron beam, and the accumulated charge at the spot bends the electron beam and distorts the image. For EBL on diamond samples, this charging effect causes bending of the electron beam and the distortion of the resulting pattern, as shown in Figure 4.4. Decreasing the accelerating voltage, aperture and current of the electron beam helps to cut down the charging effect, at the cost of lower resolution and longer exposure time.

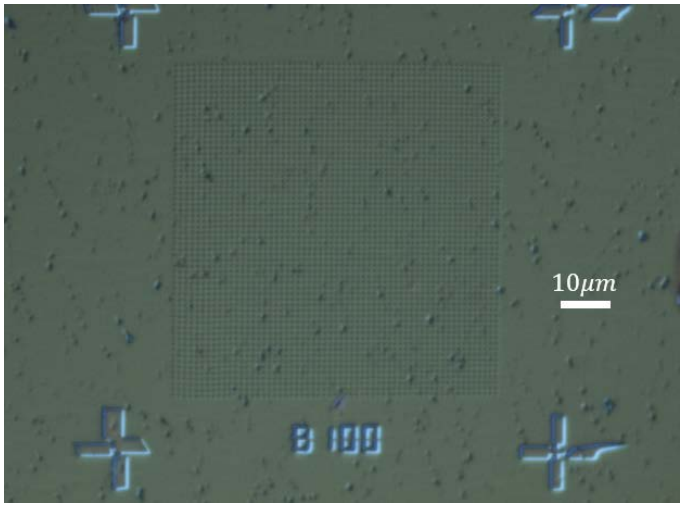

Figure 4.4 EBL with developed resist on diamond with dot array. The markers are distorted due to charging effect of the diamond substrate.

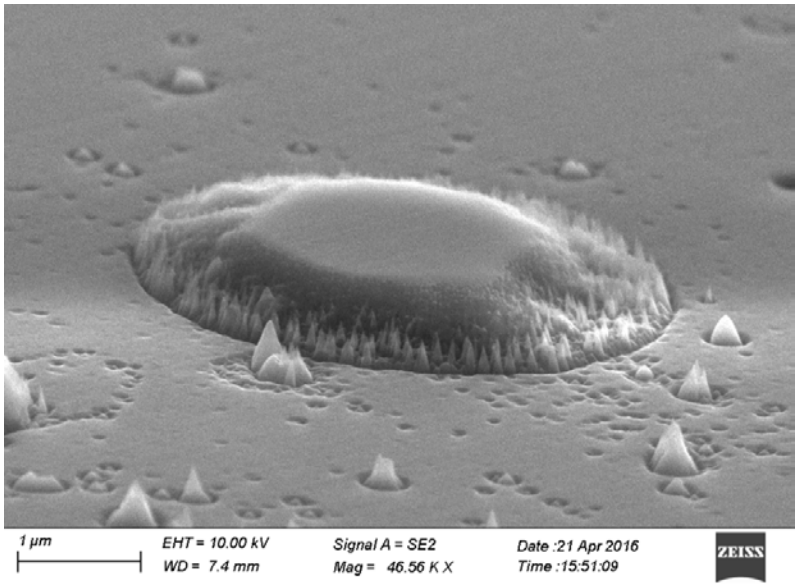

Figure 4.5 SEM image of etched diamond surface. The center island and many spikes beside it are not etched due to micro-masking, leaving a rough diamond surface.

The challenge in plasma etching of diamond is the micro-masking effect, as shown in Figure 4.5. The diamond sample is etched in an inductively coupled plasma reactive ion etcher (ICP RIE) with oxygen plasma and the etching parameters are from [106]. After a four-minute etching procedure, the diamond surface was etched down by $0.6\ \mu m$. Figure 4.5 shows the micro-masking effect on the resulting surface. Besides many grass-like spikes, there are also large areas left untouched, as the smooth original surface at the center of the island. To solve this micro-masking problem, Hausmann et al. tried with many different combinations of etching parameters in [106] to get the best combination. The micro-masking effect remains unsolved due to limited access to ICP RIE.

4.4 TUNING FORK FEEDBACK SPM SYSTEM

The SPM system we built is based on MadPLL, the SPM controller from Mad City Labs Inc. This controller provides us three driving mode of tuning fork. As the oscillating tuning fork with tip touching the sample surface, the oscillation is influenced by van der Waals force between the tip and the sample surface. A measured parameter of the oscillation, amplitude, frequency or phase, is used as a feedback signal to keep the distance between the tip and the surface constant while scanning across the sample.

The most traditional driving mode is driven oscillation of the tuning fork. A sinusoidal driving voltage with predefined frequency and amplitude is synthesized and sent to the tuning fork, leading to a driven oscillation of the tuning fork. When the tuning fork touching the sample surface, amplitude and phase of the driven oscillation will be shifted under the influence of van der Waals force, while the frequency remains the same as the driving frequency. Either the amplitude shift or the phase shift is used as the feedback signal. The driven oscillation mode is suitable for the tuning forks with quality factor $Q < 100$ [107].

Self-oscillation is the driven oscillation when the driving force is controlled by the oscillation itself so that the driving force acts in phase with velocity, leading to a negative damping of the oscillation. No predefined frequency is needed for self-oscillation because the resonance frequency can be found by itself. The self-oscillation mode is another mode allowed in our SPM controller, where the tuning fork is driven under self-oscillation. In self-oscillation mode, a phase

shifter is required for adjusting the phase of driving force for maintaining in phase with velocity. As a result, the phase of oscillation is not a good choice of feedback signal for SPM. The frequency and amplitude of the oscillation is used as feedback signal. Self-oscillation mode is suitable for tuning forks with quality factor $Q > 1000$ [107].

For tuning forks with mediocre quality factors, the self-oscillation is assisted with a phase lock loop (PLL). In the PLL-assisted mode, a clean sinusoidal signal is synthesized and frequency-locked to the measured oscillation via the PLL.

Akiyama probes are AFM probes which integrates a vertical tip to a horizontal quartz tuning fork and compatible with our SPM setup [108]. We used Akiyama probes for scanning tests of our SPM. The Akiyama probe is characterized with frequency scan in driven oscillation mode. After adjusting the parasitic capacitance compensation parameter and proper gain of the amplifiers [107, 109], the frequency response data is shown in Figure 4.6 and the quality factor is calculated as $Q = 750$.

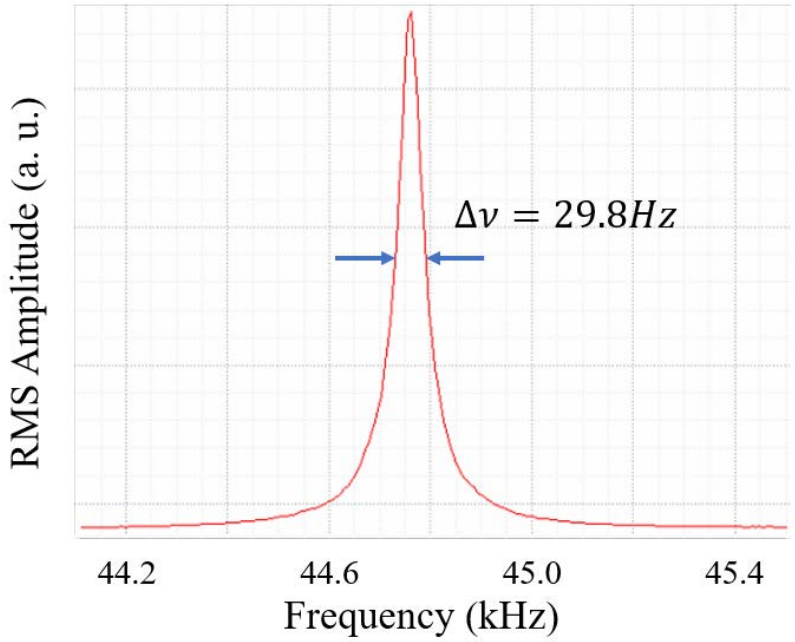

Figure 4.6 Akiyama probe frequency response in driven oscillation mode. The linewidth is measured as full width at half maximum (FWHM).

The image of a resolution target under our AFM with Akiyama probe using PLL mode is shown in Figure 4.7, and a line cut of data marked with red line is shown in Figure 4.8. The fluctuation of z position is at the order of 10 nm, which prevents us from getting images with higher resolution.

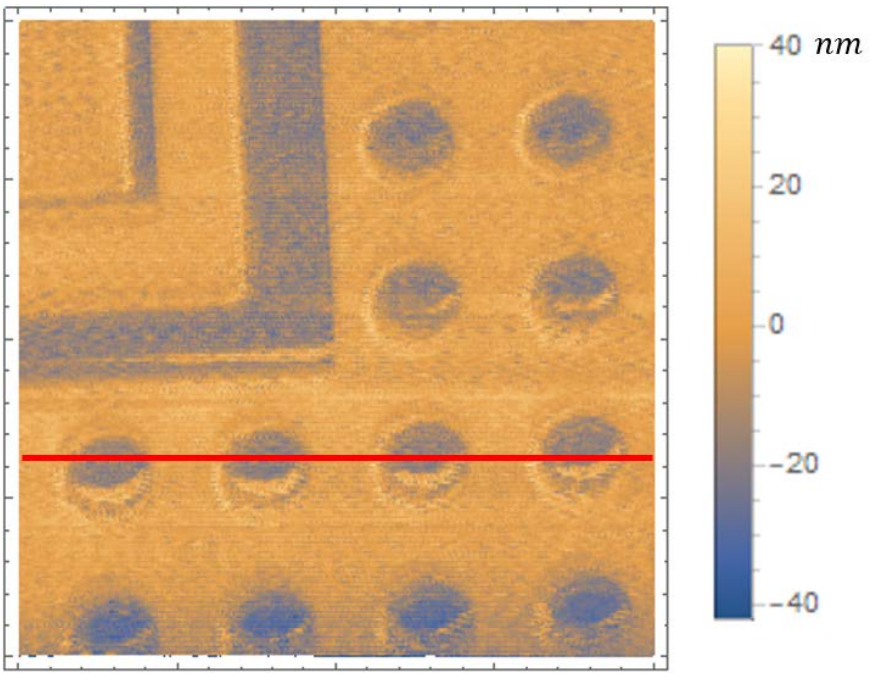

Figure 4.7 20 μm × 20 μm AFM image of resolution target with hole array whose depth is 20 nm. The incline angle correction of the data has been made via 3-point calibration.

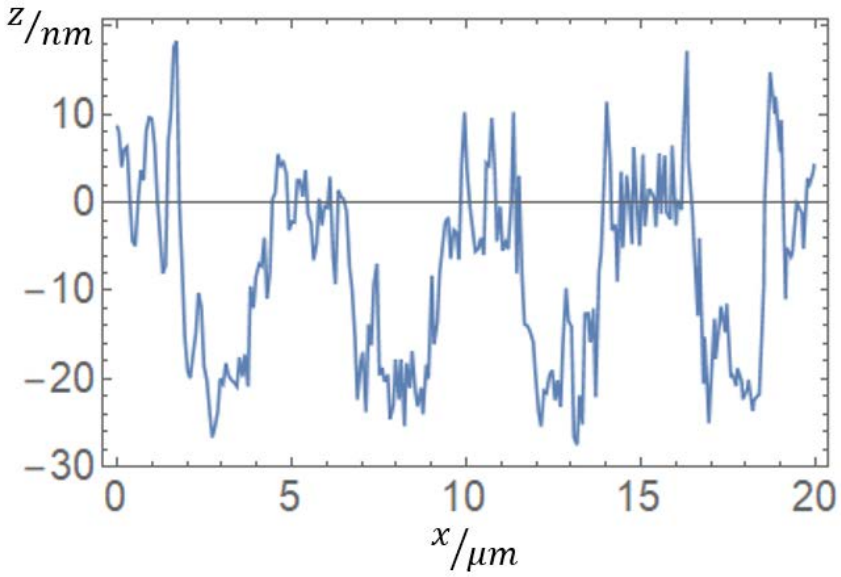

Figure 4.8 Line cut of image data in Figure 4.7 (marked with red line). Despite the large fluctuation in measured *z* position, the pattern with depth of 20 nm can still be resolved.

The fluctuation happens not only in the scanning process, but also when the Akiyama probe is staying at a fixed location, as shown in Figure 4.9. This instability could be from either lacking decent acoustic hood or inappropriate PI parameters in feedback control loop.

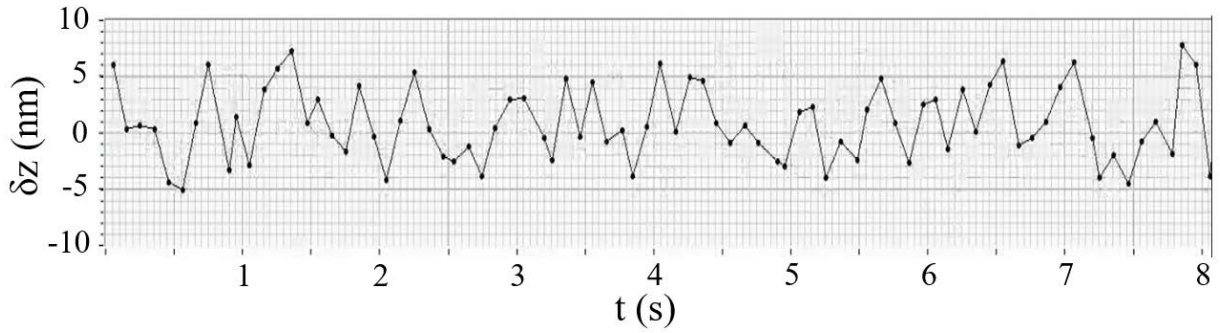

Figure 4.9 Fluctuation of tip height in 8 seconds. This instability of tip height when engaged is the main reason for the large fluctuation in the scanning image.

4.5 CONCLUSION

With efforts made towards the implementation of a SDPM, we realize that such a diamond-based SPM system with sub-nm resolution is inherently difficult to build. Only a handful of research groups around the world are successful in experimental implementation of SPDM system with diamond probe. Meanwhile, the atomic force microscope (AFM) in our lab is experiencing fluctuations not only when scanning but also when staying still. Further work is required to reduce these fluctuations and carry out NV magnetic imaging measurements. Considering the efforts and instrumental investment of such system, many groups shift their research interests in SPDM to magnetic sensing with stationary surface NV centers in various context, as discussed in the following chapter.

5.0 SENSING EXTERNAL ELECTRON SPINS WITH MAGNETIC RESONANCE OF SINGLE SPINS IN DIAMOND

This chapter introduces NV center magnetometry for sensing external spins and presents results in our experiments. This ongoing experiment has potential applications in interdisciplinary subjects in physical chemistry. One of the major contribution of this thesis is that we clearly show detection of electron spin from copper ions external to the diamond lattice. Unlike past work using nitroxide electron spin, which is hard to distinguish from nitrogen donors in diamond lattice, our work present evidence for detection of external copper ion spins. Another important contribution is that we show collapse and revival pattern and coherent oscillations in DEER (double electron-electron resonance) Rabi experiment, which implies the signal we observed may be from individual spins.

5.1 INTRODUCTION: NV CENTER MAGNETOMETRY FOR SENSING EXTERNAL SPINS

The sensitivity of NV magnetometry is limited by the coherence time T_2 of the NV center (or inhomogeneous dephasing time T_2^* for DC magnetometry) as $\eta \propto \frac{1}{\sqrt{T_2}}$ [17]. With isotopically purified diamond sample, the coherence time of NV center was measured at the order of milliseconds, corresponding to an AC sensitivity of ~ 10 nT$/\sqrt{\text{Hz}}$ [19]. This sensitivity is enough to sense nearby spins as long as the target spin is close to the NV center [24]. In fact, sensing dark spins in diamond lattice near the NV center was realized in [110]. However, for most general-purpose applications of a nanoscale magnetic sensor, it is important to show the capability of sensing not only the spins in diamond lattice, but external spins as well.

As the magnetic field due to a target spin dipole decays quickly as the inverse third power of distance, the NV center as a sensor needs to be put very close to the external target spin, which requires the NV center very close to the diamond surface. Unlike the NV centers deep inside the lattice, the surface NV centers suffer from a relatively short coherence time. The decoherence of these surface NV centers is due to the environmental spin bath, mainly from the surface, including free electron spins from the dangling bonds, hydrogen nuclear spins from hydrogen termination and moisture absorbed by the surface, the abundant nitrogen electron and nuclear spins implanted or doped during diamond growing process due to low yield of $N \rightarrow$ NV transition, and all kinds of other spins at the surface. Efforts have been made to improve the surface environment by physical and chemical treatments [62, 111], engineered annealing processes [56, 57], and diamond growing process [55]. The best coherence time reported for surface NV centers is in δ-doped diamond samples, while the improved coherence time for implanted surface NV centers is ~ 50 μs.

External spin sensing is still possible with the help of dynamic decoupling sequences. With a large number of π pulses periodically driving the surface NV center, the coherence time can be increased to ~ 100 μs and signal of nuclear ensemble can be observed [112, 113]. For example, detection of nuclear spin signals using single surface NV center was reported in 2013, with the help of dynamical decoupling sequences with 80 π pulses [114]. Signals from only ~ 30 nuclear spins on a 2-dimensional material using single surface NV center can be detected with up to 371 π pulses [115]. However, the drawbacks of using dynamical decoupling sequences are also obvious. The more π pulses are used in the dynamical decoupling sequences, the more time it takes for the entire measurement. The overall measurement time for each data point could be up to tens of seconds in order to achieve $\mathrm{SNR} = 1$ (signal to noise ratio) [116].

On the other hand, a smarter approach is to drive the target spin actively [48, 54, 117-121]. As long as the resonant frequency of the target spins is different from the resonant frequency of NV center, and the relaxation time T_1 of the target spin is long enough to allow active driving, we can drive the target spins without interfering the NV center magnetometry. Driving the target spin distinguishes the target spin from the environmental spin bath, which is the essence of magnetic resonance. By actively driving the target spin, the sensitivity is not limited to the coherence time T_2 of the target spin, but the depolarization time T_1 instead [54]. The terminology DEER (double electron-electron resonance) is borrowed from electron paramagnetic resonance (EPR) for

designed experimental sequence of external spin sensing with target spin driving field in 2011 [117]. In this chapter, we will demonstrate our experimental results of DEER.

5.2 SENSING EXTERNAL ELECTRON SPINS: METHOD, THEORY AND SIMULATIONS

The experimental sequence of DEER is shown in Figure 5.1. The DEER sequence is based on the spin echo sequence of the NV center. As mentioned in chapter 2, the spin echo sequence is used in AC magnetometry as the resultant fluorescence intensity is sensitive to changes of magnetic field. [13] In the DEER sequence, the target spins are driven by another driving pulse at the same time of the π pulse of the spin echo sequence, causing a change of external magnetic field between the two halves of spin echo due to the target spin flipping, and consequently a decrease in fluorescence.

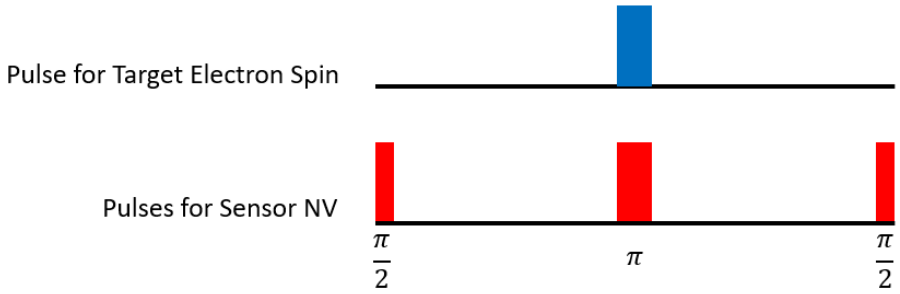

Figure 5.1 Experimental sequence of DEER. The pulse sequence for the NV center is a spin echo sequence used for detecting AC magnetic field. When the pulse for the target electron spin drives the target spin, the resultant AC magnetic field is detected by the NV center.

5.2.1 Surface NV Centers Preparation

Although the δ-doping technique produces the surface NV centers with best quality (coherence time and depth control), it is extremely instrument-demanding, and very few groups reported

[13] In section 2.4.4 the measured fluorescence signal is translated into probability in spin state $|0\rangle$. For DEER experiments in this chapter, the convention is to leave the measured fluorescence as it is.

successful in this technique [122]. We used the traditional ion implantation to generate surface NV centers. We start with a ⟨100⟩-cut CVD bulk diamond from Element Six. It is the highest grade (electronic grade) listed by the company with low concentration of native ^{14}N (< 1 ppb). It is not isotopically engineered and the concentration of ^{13}C is at natural level of ~1.3 %. ^{15}N ions are implanted into our diamond sample with proper implantation parameters.

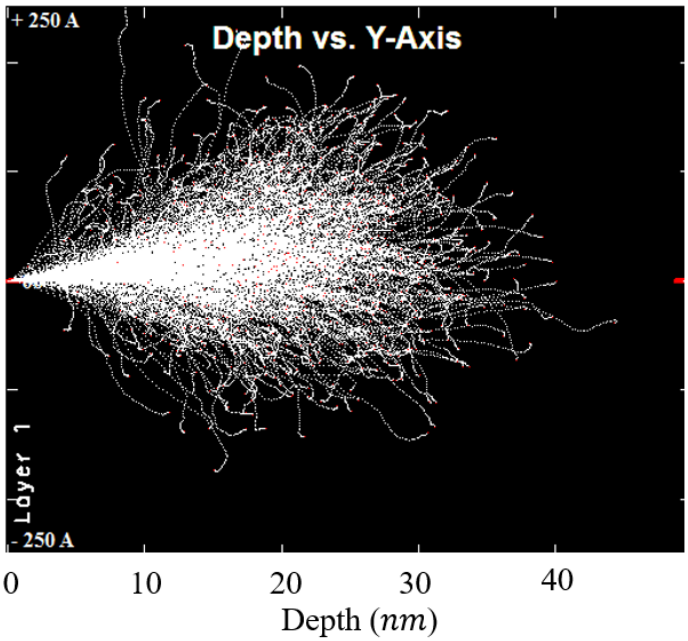

Figure 5.2 Simulation of TRIM with 1000 repetitions of nitrogen ion implantation into bulk diamond. Using implantation energy of 14 keV, incident angle of 7°, the average implantation depth is expected to be 20 nm.

The ion implantation of ^{15}N ions into diamond substrate is simulated with SRIM (Stopping and Range of Ions in Matter) and TRIM (Transport of Ions in Matter) to find out the proper implantation energy for the expected depth [52]. As shown in Figure 5.2, with implantation energy at 14 keV, the trajectories of implanted ^{15}N ions stop at an average depth of ~20 nm. The longitudinal straggle of the depth is ~7 nm, implying a wide-spread distribution of depth of resulting implanted NV centers. The ^{15}N ion implantation was commercially done by INNOViON Corp. with 14 keV implantation energy, $1 \times 10^9/\text{cm}^2$ dose, and 7° angle of incidence. The angle of incidence is used to decrease the straggling by preventing ions from tunneling through interstitial channels of the lattice.

The implanted diamond sample was then annealed with a tube furnace in a forming gas atmosphere (N_2 and H_2, 10 mTorr pressure) at 1000 ℃ for two hours. The ion implantation not

only implants nitrogen ions into the diamond lattice, but generates large amount of damages, especially vacancies, to the lattice as well. During the annealing process, the vacancies become mobile and the majority diffuse to the diamond surface, while some others are captured by the implanted nitrogen nuclei nearby and form NV centers.

Because of the oxygen residual in the atmosphere during the annealing process, the diamond surface is usually graphitized. The graphitization layers on diamond surface has similar fluorescence spectrum as the phonon side band of NV center fluorescence and will overwhelm the signal fluorescence from our NV centers. The graphitization layers can be removed by acid cleaning, bathing the diamond sample in a boiling mixture of sulfuric, nitric and perchloric acid for more than one hour. Detailed setup for acid cleaning is described in Appendix B.5.

The target electron spins sample we use is Cu^{2+} ions. Cu^{2+} is a commonly used spin label in molecular EPR (electron paramagnetic resonance) [123]. The functionalization of Cu^{2+} ion spin labels on molecule has smaller spatial flexibility to the molecule compared to some other spin labels [124, 125]. Cu^{2+} ions have large anisotropy in g-factor and hyperfine coupling strength, which leads to large splitting in spectrum and easier selective driving. Compared to some other spin labels, Cu^{2+} ions require less functionalization and result in less influence on the molecule.

During our sample preparation, a small amount of water solution containing 100 nmol of $CuCl_2$ is mixed into 1 mL water solution with 0.01 % concentration of poly-L-lysine. A small droplet ($\sim$5 μL) of the mixed solution with Cu^{2+} target spins is dropped on the diamond surface with implanted NV centers. After drying out, the target spins with poly-L-lysine residuals holding them in position are left on the diamond surface.

5.2.2 Experimental Setup

The confocal microscope used in our DEER experiments is implemented with scanning sample mechanism. As shown in Figure 5.3, the diamond is placed on top of a coverslip with fabricated coplanar waveguide. The coplanar waveguide delivering microwave to the NV center is fabricated with lithography and metal deposition. Detailed fabrication procedure of the coplanar waveguide on coverslips is described in Appendix B.6. Note that the diamond is never closely touching the coverslip and the waveguide due to dust particles or lift-off residuals in between. The gap between

the diamond and the coverslip is usually at the order of 10 μm, as we can see two different focuses of illumination light with our confocal microscope. Tiny amount of immersion oil is applied to fill the air gap between the diamond and the coverslip. The confocal microscope with a coverslip-corrected oil-immersion objective see through the coverslip from the bottom to look at the NV center.

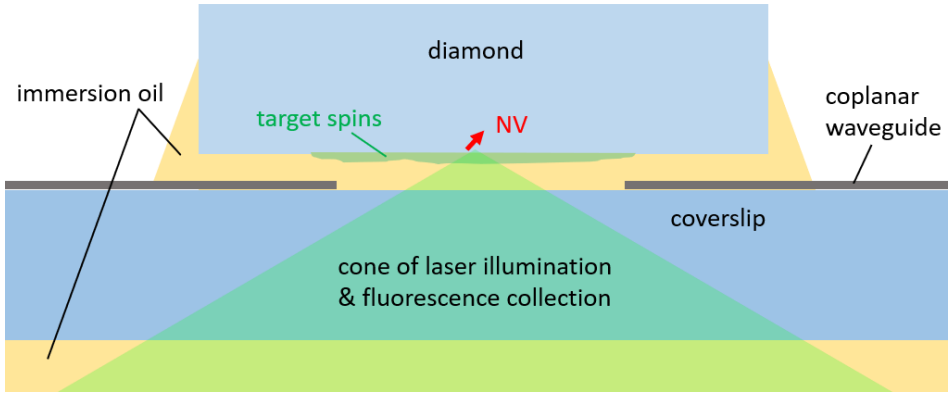

Figure 5.3 Schematic drawing of experiment configuration near the NV center. The chemical holding target spins is put on diamond surface with NV center implanted. The coplanar waveguide is fabricated on the coverslip. The air gap between the diamond surface and cover slip is filled with immersion oil.

The coverslip is glued to a sample holder mounted to a 3-axes piezo nanopositioning stage. When we scan the position of the sample mount while keeping the optical beam fixed, a fluorescence image of confocal microscope is acquired. Figure 5.4 shows an example of confocal image of implanted surface NV centers under this confocal microscope.

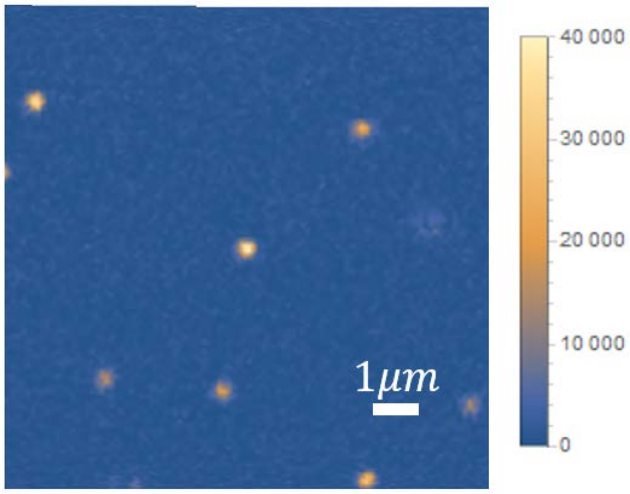

Figure 5.4 Confocal image of implanted NV centers. The diameter of the Gaussian bright spots (the single NV centers) is 0.3 μm.

In DEER experiments, the microwave pulses to drive NV centers and target spins are in different frequencies, because the zero-field splitting of NV center makes the Larmor frequency of NV center different from typical electron spins. As shown in Figure 5.5 the microwave circuit is implemented using two separate microwave synthesizers with independent control and separate microwave switches triggered by independent channels of AWG (Arbitrary Waveform Generator). The two separate microwaves are combined and amplified before delivered to the NV center. The coplanar waveguide fabricated on the coverslip is connected to our microwave circuit with soldered microwave SMA connector at one end, leaving the other end of the waveguide open.

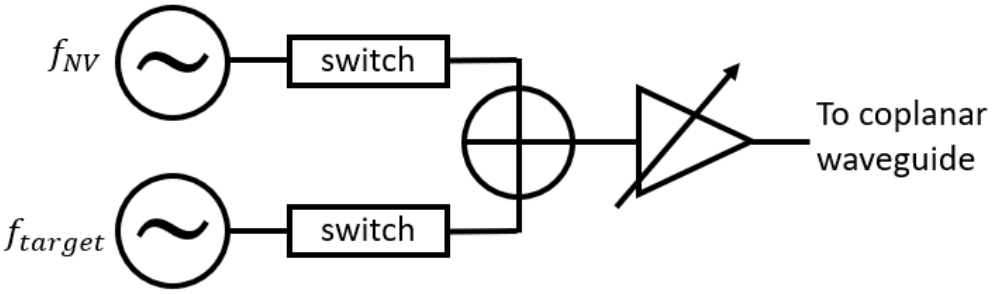

Figure 5.5 Schematic drawing of microwave circuit. The microwave pulses to drive the NV center and the target spins are generated by two different synthesizer and combined into one channel before amplified and sent to the waveguide.

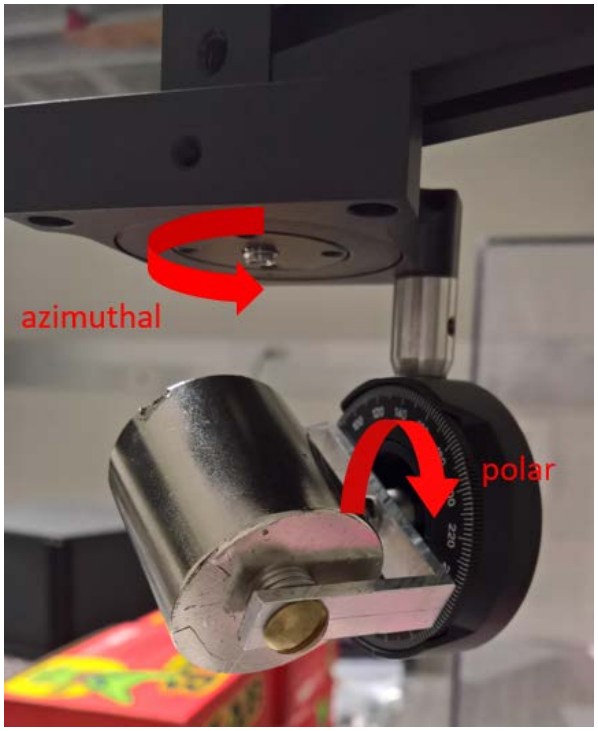

Figure 5.6 Permanent magnet on rotation mounts. By independent controlling the azimuthal angle and the polar angle, the axis of the permanent magnet can be rotated to any direction in space.

To generate a constant magnetic bias field and align it with the $\mathrm{N}-\mathrm{V}$ axis of the chosen NV center, a permanent magnet is held by two rotation mounts hanging from a fixed beam, as shown in Figure 5.6. The two rotation mounts are responsible for the azimuthal angle and polar angle independently, resulting a rotation degree of freedom in all possible directions in space.

This experimental setup is the best setup in our lab. It has the best optical resolution and highest photon count rate up to 1.3×10^5 per second from a single NV center, because of the high NA (numerical aperture) of the oil-immersion objective. It can achieve much higher and more stable Rabi frequency (> 25 MHz) of microwave driving field compared to the experimental setup used in chapter 3 (12.5 MHz), due to high efficiency of coplanar waveguide. However, the thin layer of immersion oil between the coverslip and diamond surface causes us trouble. Under high intensity of laser illumination for long time (one week at minimum), this thin layer of oil becomes fluorescent and the fluorescence overwhelms the signal fluorescence from NV centers. In our experimental configuration there is no way to refresh the immersion oil between the coverslip and diamond sample without moving the diamond. Once we take off the diamond sample for cleaning and refresh the immersion oil in between, we cannot put it back exactly the same position and find the same NV center under our microscope. As a result, we can only keep working on the same NV center for weeks.

5.2.3 Theory of DEER on Single Electron

To understand the DEER experiment and make a theoretical prediction of DEER signal, a simplified physical model is built. In this model, we assume the target spin is a single electron spin near the NV center and the only interaction between the target spin and the NV center is magnetic dipole-dipole interaction. The Hamiltonian of magnetic dipole-dipole interaction can be written as:

$$H = -\frac{\mu_0}{4\pi r^3}[3(\vec{m}_1 \cdot \vec{e}_r)(\vec{m}_2 \cdot \vec{e}_r) - \vec{m}_1 \cdot \vec{m}_2] \tag{5.1}$$

where the r is the distance between the two magnetic dipoles $\vec{m}_1$ and $\vec{m}_2$, and $\vec{e}_r$ is the unit vector indicating the direction of the displacement between $\vec{m}_1$ and $\vec{m}_2$. This Hamiltonian can also be written as:

$$H = -\vec{B} \cdot \vec{m}_2$$

$$\vec{B} = \frac{\mu_0}{4\pi r^3}[3(\vec{m}_1 \cdot \vec{e}_r)\vec{e}_r - \vec{m}_1]$$

where $\vec{B}$ is the magnetic field at $\vec{m}_2$ location due to the magnetic dipole $\vec{m}_1$. In our DEER experiments, $\vec{m}_1$ is the target spin and $\vec{m}_2$ is the NV center. The magnetic field $\vec{B}$ at the NV center location is measured by the NV center with spin echo sequence.

As mentioned in chapter 2, the NV center is only sensitive to magnetic field component in $N-V$ axis (defined as z axis). This component can be written as:

$$B_z = \vec{B} \cdot \vec{e}_z = \frac{\mu_0}{4\pi r^3}[3(\vec{m}_1 \cdot \vec{e}_r)(\vec{e}_r \cdot \vec{e}_z) - \vec{m}_1 \cdot \vec{e}_z]$$

For single electron spin as our target spin, $\vec{m}_1 = \frac{\gamma_e \hbar}{2}\vec{e}_1$,

$$B_z = \frac{\mu_0 \gamma_e \hbar}{8\pi r^3}[3(\vec{e}_1 \cdot \vec{e}_r)(\vec{e}_r \cdot \vec{e}_z) - \vec{e}_1 \cdot \vec{e}_z]$$

This can transform to a simplified form

$$B_z = \vec{e}_1 \cdot \left\{\frac{\mu_0 \gamma_e \hbar}{8\pi r^3}[3(\vec{e}_r \cdot \vec{e}_z)\vec{e}_r - \vec{e}_z]\right\} = \lambda \vec{e}_1 \cdot \vec{e}_i \tag{5.2}$$

where λ and $\vec{e}_i$ are the magnitude and direction of the vector $\left\{\frac{\mu_0 \gamma_e \hbar}{8\pi r^3}[3(\vec{e}_r \cdot \vec{e}_z)\vec{e}_r - \vec{e}_z]\right\}$:

$$\begin{cases} \lambda = \dfrac{\mu_0 \gamma_e \hbar}{8\pi r^3} / \|3(\vec{e}_r \cdot \vec{e}_z)\vec{e}_r - \vec{e}_z\| \\ \vec{e}_i \parallel [3(\vec{e}_r \cdot \vec{e}_z)\vec{e}_r - \vec{e}_z] \end{cases} \tag{5.3}$$

When $\vec{e}_1$ is aligned with $\vec{e}_i$, the z component of magnetic field at NV center location reaches maximum.

In the first half of the spin echo sequence, given the external magnetic field $B_z = \lambda \vec{e}_1 \cdot \vec{e}_i$ and neglecting all other magnetic fields from the spin bath, the phase accumulated due to the target spin is:

$$\varphi_1 = \int_0^\tau \gamma_e B_z dt = \gamma_e \tau \langle \lambda \vec{e}_1 \cdot \vec{e}_i \rangle_t \tag{5.4}$$

where τ is the time of each half of spin echo sequence. As calculated above, the parameters λ and $\vec{e}_i$ are time-independent.

$$\varphi_1 = \gamma_e \tau \lambda \langle \vec{e}_1 \rangle_t \cdot \vec{e}_i$$

With the existence of the bias constant magnetic field, the target spin is under precession along the external magnetic field. The bias constant magnetic field is induced by a permanent magnet as described in the previous section 5.2.2, and aligned with the $N-V$ axis of the NV center by

adjusting the rotation mounts while monitoring the fluorescence intensity from the NV center. Since there is possibility of misalignment of magnetic field, without losing the generality, the direction of bias magnetic field is defined as $\vec{e}_B$ instead of $\vec{e}_z$. $\vec{e}_B$ and $\vec{e}_z$ must be close enough so that the NV magnetometry described in chapter 2 is still valid. The frequency of the target spin precession along $\vec{e}_B$ is the Larmor frequency which is on the order of 10^2~10^3 MHz. During the first half of echo with τ~6 μs, the target spin precession along $\vec{e}_B$ is on the order of 10^3 cycles. Therefore, the time-average of $\vec{e}_1$ is the projection of $\vec{e}_1$ on $\vec{e}_B$ direction:

$$\langle \vec{e}_1 \rangle_t = (\vec{e}_1 \cdot \vec{e}_B)\vec{e}_B$$

The phase accumulated in the first half of spin echo is calculated as:

$$\varphi_1 = \gamma_e \tau \lambda (\vec{e}_1 \cdot \vec{e}_B)(\vec{e}_B \cdot \vec{e}_i) \tag{5.5}$$

To consider the effect of microwave driving pulse on target spin in the middle of the spin echo, we choose the rotating frame that rotates with the driving field. This rotating frame is a completely different rotating frame from the one for the NV center. This rotating frame for the target spin is rotating about $\vec{e}_B$, the direction of the bias magnetic field, while the rotating frame for the NV center rotates about $\vec{e}_z$. Setting up different coordinate system XYZ for the target spin rotating frame helps to separate these two systems apart. Figure 5.7 shows the schematic drawing of the two rotating coordinate systems.

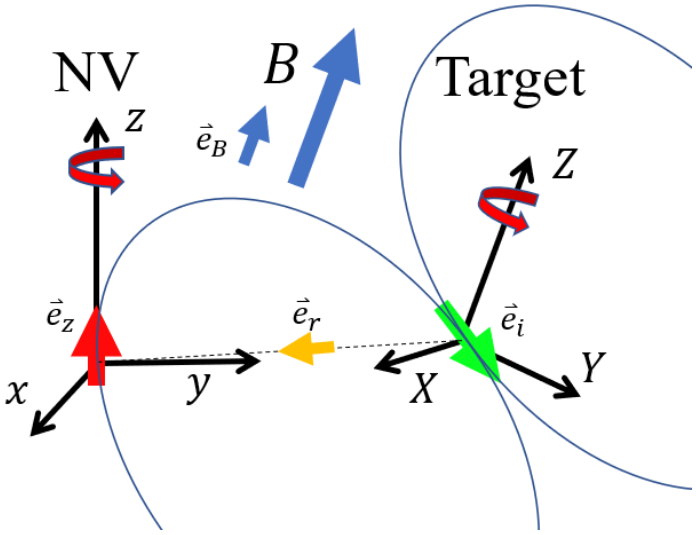

Figure 5.7 Schematic drawing of NV center system and target spin system with separate coordinate systems in lab frame. Unit vectors $\vec{e}_B$, $\vec{e}_i$, $\vec{e}_r$ are also shown with colored arrows.

In rotating frame XYZ, the target spin is preceding along an effective constant magnetic field which depends on the microwave amplitude and frequency detuning, the same as driving the

NV center described in chapter 2 and chapter 3. Without losing generality, the rotating frame is chosen so that the initial phase of driving field is 0, and the manipulation to the target spin by the driving field can be described as a rotation operation $R_{\vec{a}}(\alpha)$ along axis $\vec{a}$ by angle α, where the axis in XYZ coordinate system is

$$\vec{a} \parallel (\Omega, \quad 0, \quad \Delta) \tag{5.6}$$

and the angle

$$\alpha = t_p\sqrt{\Omega^2 + \Delta^2} \tag{5.7}$$

where and t_p is the pulse length. After the driving pulse in the middle, the direction of target spin is rotated as

$$\vec{e}_1 \xrightarrow{driving\ pulse} \vec{e}_1' = R_{\vec{a}}(\alpha)\vec{e}_1$$

Note that this result is in the rotating XYZ coordinate system. Back to the lab frame, the manipulation to the target spin can be treated as a nutation. Another rotation about $\vec{e}_B$ with random angle $\phi_r \in [0, 2\pi)$ transforms the $\vec{e}_1'$ to the lab frame

$$\vec{e}_1' = R_{\vec{e}_B}(\phi_r)R_{\vec{a}}(\alpha)\vec{e}_1$$

ϕ_r is random because the phase of target spin driving field is random. At the same time, the π pulse on the NV center makes the phase accumulated opposite:

$$\varphi_1 \xrightarrow{\pi\ pulse} -\varphi_1 = -\gamma_e\tau\lambda(\vec{e}_1 \cdot \vec{e}_B)(\vec{e}_B \cdot \vec{e}_i)$$

In the second half of spin echo, the phase accumulated due to the target spin can be calculated by replacing $\vec{e}_1$ with $\vec{e}_1'$,

$$\varphi_2 = \gamma_e\tau\lambda(\vec{e}_1' \cdot \vec{e}_B)(\vec{e}_B \cdot \vec{e}_i)$$

And the net phase of the complete spin echo sequence is:

$$\varphi = \varphi_2 - \varphi_1 = \gamma_e\tau\lambda(\vec{e}_B \cdot \vec{e}_i)\left[\left(R_{\vec{e}_B}(\phi_r)R_{\vec{a}}(\alpha)\vec{e}_1 - \vec{e}_1\right) \cdot \vec{e}_B\right] \tag{5.8}$$

In our DEER experiments, τ and α are controlled by our sequence design and microwave driving field parameters, λ, $\vec{e}_B$ and $\vec{e}_i$ are arbitrary constants depend on the displacement of target spin from the NV center and the alignment of bias magnetic field, ϕ_r is random and $\vec{e}_1$ is a random direction because the target spin is not initialized to a fixed state before the experimental sequence. As a result, the measured fluorescence is an ensemble average of all possible directions of $\vec{e}_1$ and all possible angle ϕ_r:

$$f = a\langle\cos\varphi\rangle_{\vec{e}_1,\phi_r} + b$$

where a is the contrast of spin readout and b is background level. Both of a and b can be calibrated with Rabi oscillation of NV center, as mentioned in chapter 2. The probability integral can be expressed as:

$$f(\Omega, \Delta, t_p) = a \int_0^{2\pi} d\phi_r \int_{-1}^{1} d\cos\theta_1 \int_0^{2\pi} d\phi_1 \cos\{c[(R_{\vec{e}_B}(\phi_r) R_{\vec{a}}(\alpha)\vec{e}_1 - \vec{e}_1) \cdot \vec{e}_B]\} + b \quad (5.9)$$

where θ_1 and ϕ_1 are the polar angle and azimuthal angle of $\vec{e}_1$, and $c = \gamma_e \tau \lambda(\vec{e}_B \cdot \vec{e}_i)$ is the dimensionless prefactor. The measured fluorescence signal is a function of the Rabi frequency Ω, detuning Δ, and the pulse length t_p of the driving field of target spin. The dependence on Ω, Δ and t_p is at the rotation operator $R_{\vec{a}}(\alpha)$. Unfortunately, there is no analytical solution of the probability integral. To better understand our DEER spectrum and our DEER Rabi experiment, numerical integration is used to calculate $f(\Delta)$ and $f(t_p)$ with different assumptions of parameters.

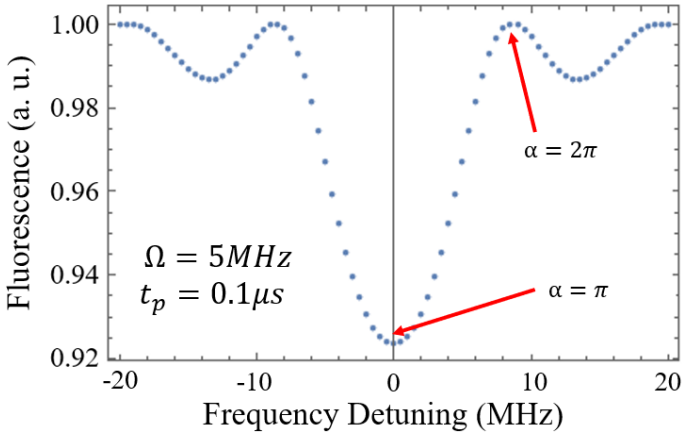

Figure 5.8 Calculation of DEER spectrum of single target spin using numerical integration of $f(\Delta)$. The pulse length of the target spin driving field is designed to make a π pulse when resonant.

Figure 5.8 shows a numerical integration of $f(\Delta)$ with appropriate parameters. The parameters Ω and t_p are chosen so that the target spin driving pulse is a π pulse when the frequency of driving field is on resonance. The first revival of fluorescence signal happens when the frequency detuning satisfies $\alpha = t_p\sqrt{\Omega^2 + \Delta^2} = 2\pi$ so that the target spin driving pulse becomes a 2π pulse. Define the detuning that gives the first fluorescence revival as

$$\Delta_r = \sqrt{\frac{4\pi^2}{t_p^2} - \Omega^2} \quad (5.10)$$

Besides the position of the first fluorescence revival, Δ_r also gives a rough idea of the measured linewidth of the resonance.

The numerical integration of $f(t_p)$, the DEER Rabi experiment, is shown in Figure 5.9. The frequency of the target spin driving field is assumed to be on resonance, $\Delta = 0$. Note that $f(t_p)$ is a periodic function as the rotation operator $R_{\vec{a}}(\alpha)$ is periodic in time t_p, so our simulation shows only one period, corresponding to α from 0 to 2π. As shown in Figure 5.9, the change in the prefactor c leads to dramatic change in the shape of the function $f(t_p)$. For the situation when $c > 3$, there is an obvious deviation from sinusoidal function. In the strong coupling regime such as $c = 10$, the fluorescence signal oscillates a few cycles within a decay-revival period. It is worth mentioning that these oscillations were mistakenly recognized as Rabi oscillations of target spin in [54], and thus lead to incorrect 2π pulse length for target spin.

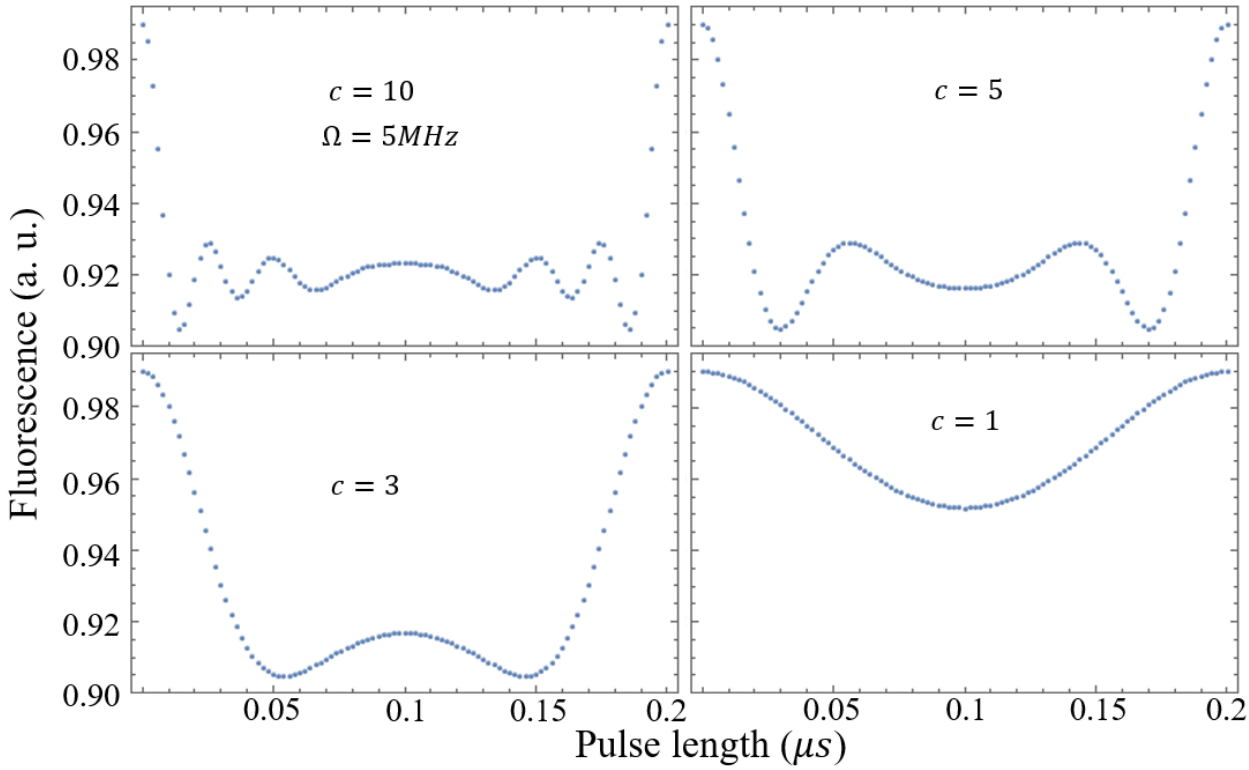

Figure 5.9 Calculation of expected DEER Rabi experiment results of single target spin using numerical integration. We can see clear oscillations when the prefactor c is much greater than 1.

The value of the prefactor c used in our simulation needs to be on the order of 10^0 to achieve reasonable contrast of measured fluorescence signal. Taking the time of spin echo sequence $\tau = 6$ μs, the $c = 1$ situation is achievable when the distance between the target spin and the NV center is ~10 nm, and ~4 nm for the $c = 10$ situation.

5.2.4 Theory of DEER on Ensemble of Electrons

The theory of DEER experiment with single target electron spin can be extended to multiple electron spins. Assuming the interaction between the target spins are negligible and each individual target electron spin has its unique λ and $\vec{e}_i$, the resultant magnetic field is

$$B_z = \sum_k \lambda_k \vec{e}_k \cdot \vec{e}_{ik} \tag{5.11}$$

where $k = 1,2,\cdots n$, n is the total number of electrons. The net phase measured is

$$\varphi = \gamma_e \tau \sum_k \lambda_k (\vec{e}_B \cdot \vec{e}_{ik}) \left(\left(R_{\vec{e}_B}(\phi_r) R_{\vec{a}}(\alpha) \vec{e}_k - \vec{e}_k \right) \cdot \vec{e}_B \right) \tag{5.12}$$

And the fluorescence as our measured signal is

$$f = a\langle \cos\varphi \rangle_{\vec{e}_1, \vec{e}_2, \cdots, \vec{e}_n, \phi_r} + b$$

This result is based on the assumption that the gradient of bias magnetic field and microwave driving field is negligible at different locations of the target spins.

For a small number of target spins nearby with different λ_k and $\vec{e}_{ik}$, the probability integration has to be done n times as the n independent target spins. For the situation with a large number of target spins and small prefactor $\gamma_e \tau \lambda_k (\vec{e}_B \cdot \vec{e}_{ik})$ for each spin, the net phase φ is the sum of many independent random contributions

$$\varphi_k = c_k \left(\left(R_{\vec{e}_B}(\phi_r) R_{\vec{a}}(\alpha) \vec{e}_k - \vec{e}_k \right) \cdot \vec{e}_B \right) \tag{5.13}$$

where $c_k = \gamma_e \tau \lambda_k (\vec{e}_B \cdot \vec{e}_{ik})$ is the prefactor for each spin. According to central limit theorem, the net phase φ tends towards a normal distribution regardless of the individual distribution for each φ_k. Obviously, the mean value of φ is 0, because each φ_k has a mean value of 0. To calculate the probability average, we choose an instant XYZ coordinate system fixed in lab frame. The random unit vector can be written as $\vec{e}_k = \left(\sqrt{1 - Z^2} \cos\phi, \quad \sqrt{1 - Z^2} \sin\phi, \quad Z \right)$ in the fixed XYZ coordinate system, the variance of each φ_k can be calculated with probability integral

$$\langle \Delta\varphi_k^2 \rangle = \langle \varphi_k^2 \rangle = \int_0^{2\pi} \frac{d\phi_r}{2\pi} \int_{-1}^{1} \frac{dZ}{2} \int_0^{2\pi} \frac{d\phi}{2\pi} c_k^2 \left(\left(R_{\vec{e}_B}(\phi_r) R_{\vec{a}}(\alpha) \vec{e}_k - \vec{e}_k \right) \cdot \vec{e}_B \right)^2 \tag{5.14}$$

Note that $\vec{e}_B = (0, \quad 0, \quad 1)$ in the XYZ coordinate system. This probability integration can be calculated as

$$\langle \Delta\varphi_k^2 \rangle = c_k^2 \frac{4\Omega^2}{3(\Omega^2 + \Delta^2)} \sin^2 \left(\pi t_p \sqrt{\Omega^2 + \Delta^2} \right) \tag{5.15}$$

For simplicity we assume the prefactors c_n for each target spin are similar and we can replace individual c_k^2 with an average value over all target spins as $\overline{c^2} = \overline{c_k^2}$. According to central limit theorem, the net phase φ, as the sum of all contributions φ_k, will have a variance of

$$\langle \Delta\varphi^2 \rangle = \sum_{k=1}^{n} \langle \Delta\varphi_k^2 \rangle = n\,\overline{c^2}\,\frac{4\Omega^2}{3(\Omega^2+\Delta^2)}\sin^2\left(\pi t_p\sqrt{\Omega^2+\Delta^2}\right) \tag{5.16}$$

And the standard deviation of the net phase is

$$\sigma_\varphi = \sqrt{\langle \Delta\varphi^2 \rangle} = \frac{2\sqrt{3n\,\overline{c^2}}\Omega}{3\sqrt{\Omega^2+\Delta^2}}\left|\sin\left(\pi t_p\sqrt{\Omega^2+\Delta^2}\right)\right| \tag{5.17}$$

Given the net phase φ is normally distributed as $\varphi \sim \mathcal{N}(0, \sigma_\varphi^2)$, the measured fluorescence can be calculated as

$$f = a\langle \cos\varphi \rangle + b = a \cdot exp\left(-\frac{\sigma_\varphi^2}{2}\right) + b$$

and written in the complete form as

$$f(\Omega, \Delta, t_p) = a \cdot exp\left[-\frac{2n\,\overline{c^2}\Omega^2}{3(\Omega^2+\Delta^2)}\sin^2\left(\pi t_p\sqrt{\Omega^2+\Delta^2}\right)\right] + b \tag{5.18}$$

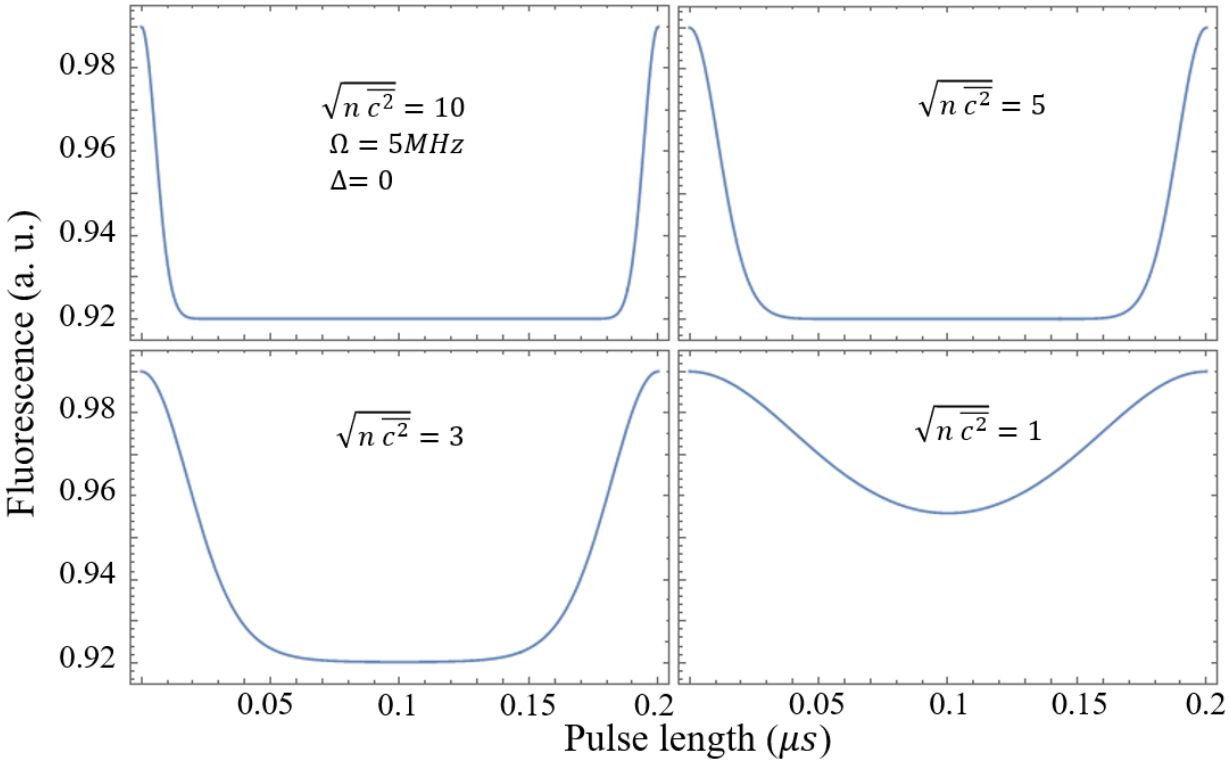

Figure 5.10 Simulation of DEER Rabi experiment of ensemble target spins. As the prefactor becomes much larger than 1, there are no oscillations showing up.

Figure 5.10 shows the simulation of DEER Rabi experiment, $f(t_p)$, on ensemble of target electron spins. Compared with simulations on single target spin, the fast oscillations in time t_p under strong coupling regime disappear for ensemble target spins. As a result, the fast oscillations within one period of DEER Rabi experiment can be used as fingerprints of single target spins.

5.3 SENSING EXTERNAL ELECTRON SPINS: EXPERIMENTAL RESULTS

As mentioned in previous section 5.2.2, for technical reasons we have a limited time (from one week to a few weeks) for DEER experiments on each NV center. We observed DEER signal from two single NV centers, named $NV1$ and $NV2$ respectively. Judging from their hyperfine splitting in pulsed ODMR frequency scan experiment and their measured coherence time from spin echo experiment (see Appendix C.5), the $NV1$ is the implanted NV center close to the surface, while the $NV2$ is unlikely implanted and unlikely to be a surface NV center.

5.3.1 DEER Spectrum

When the experimental sequence of DEER is introduced in previous section 5.2, the driving pulse of the target spin is applied at the same time as the π pulse for the NV center. However, carrying two microwave pulses at different frequencies at the same time through our microwave circuit could be problematic. We observed a large decrease in contrast of spin readout, as shown in Appendix C.6. Therefore, the experimental sequence is slightly modified to avoid this effect as shown in Figure 5.11. The driving pulse for the target spin is applied after, instead of at the same time of, the π pulse in the middle. And an identical driving pulse is applied at the first half of spin echo, just to balance any direct

For DEER experiment on $NV1$, the half sequence length τ is chosen as $6.6\ \mu s$, the first ^{13}C revival time. The pulse length of the driving pulses for target spins is $100ns$. The DEER signal we observed is the decrease in fluorescence of the NV center when the frequency of target spin driving field hits the resonance of the target spin transition, as shown in Figure 5.12. After the resonance frequency of target spins is acquired from the DEER spectrum, the DEER Rabi

experiment (see the following section 5.3.2) helps us to optimize the pulse length. As mentioned in previous section 5.2.3, the optimized pulse length doesn't have to be a π pulse length. A finer frequency scan of DEER is performed with the optimized pulse length, as shown in Figure 5.12. effects on the NV center of the driving pulse.

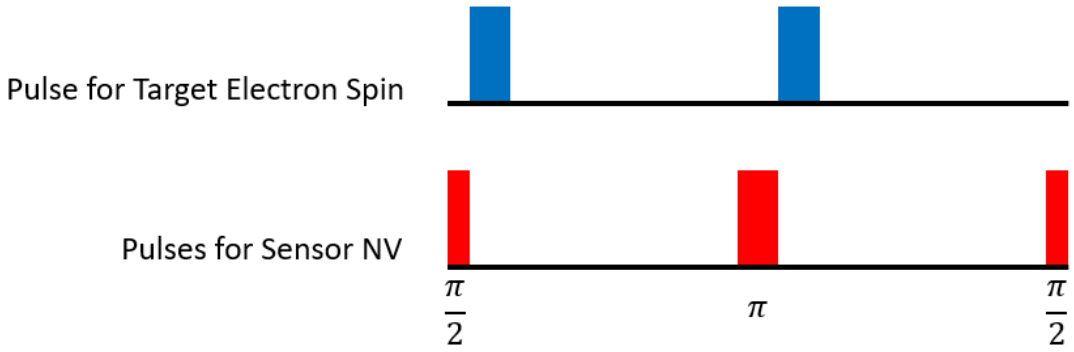

Figure 5.11 Modified experimental sequence for DEER. The target spin driving pulse in the middle is slightly shifted in time, right after the π pulse. The first target spin driving pulse is added to balance any unwanted influence on the NV center.

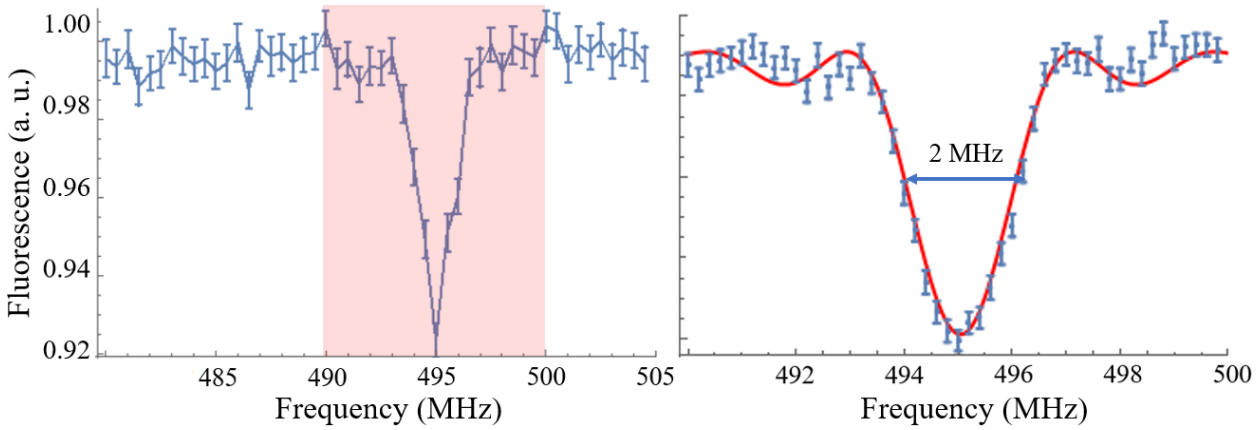

Figure 5.12 DEER spectrum of the target spin with $NV1$. The shaded region in the left is zoomed in with more averages (500 data point averages, 50000 times repetition of sequence per data point) shown to the right. The pulse width for the target spin is 100 ns. The π pulse width for the NV center is 20 ns. The resonant frequency of NV center is 2.4 GHz. Red curve is the fit to the data using the function of pulsed ODMR in Appendix A.5.

The spectrum data is shown directly without any fitting functions, because the theoretical model discussed in section 5.2.3 does not have an analytical expression. We notice the linewidth of our DEER spectrum $\Delta\nu = 2$ MHz is much narrower than expected.[14] As our pulse length of the

[14] Here the linewidth refers to FWHM (full width at half maximum/minimum) directly measured from our data, not from the fit.

target spin driving field is 100 ns, the power broadening should be ~10 MHz, which is similar to our theoretical calculation with our model in section 5.2.3.

The $NV1$ suffered from fluorescent immersion oil after one week as mentioned in previous section 5.2.2. After the sample cleaning, we found another NV center $NV2$ we can work with. As mentioned above, $NV2$ is unlikely a surface NV center because it is not an implanted NV center and it has relatively long coherence time. The observation of DEER signal on $NV2$ is unexpected.

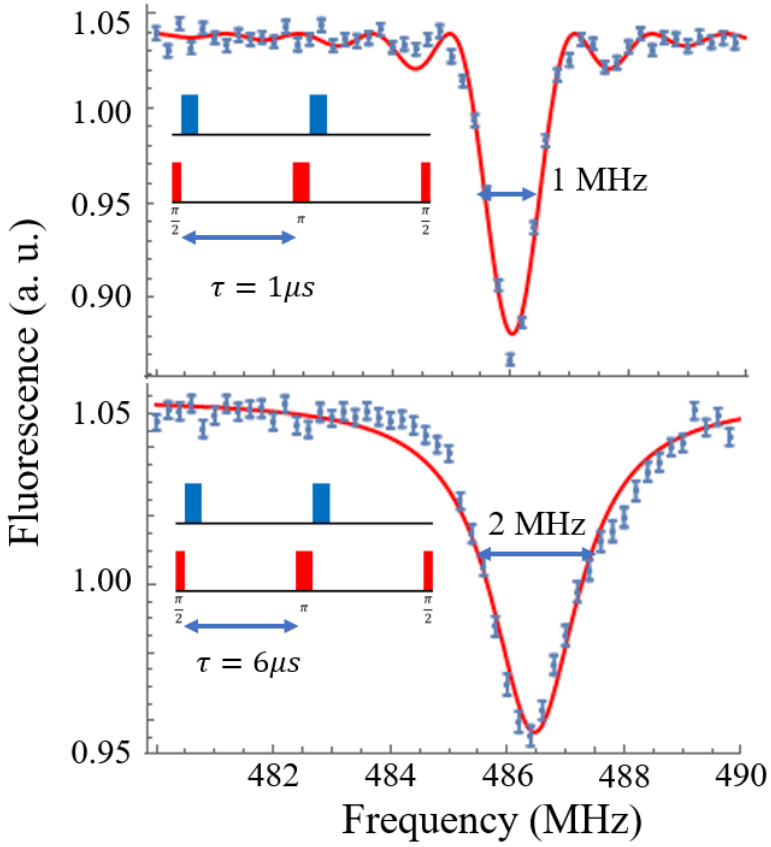

Figure 5.13 DEER spectrum of the target spin with $NV2$. The experiment is based on spin echo sequences with $\tau =$ 1 μs and $\tau = 6$ μs half-length respectively. The pulse width for the target spin is 220 ns. The π pulse width for the NV center is 20 ns. The resonant frequency of NV center is 2.4 GHz. Red curve in the top plot is the fit to the data using the function of pulsed ODMR in Appendix A.5. Red curve at bottom is a Lorentzian fit.

The DEER spectrum observed on $NV2$ is shown in Figure 5.13. The optimized pulse length for target spin is 220 ns, the pulse length of π pulse. Based on the spin echo experiment on $NV2$, the first ^{13}C revival is at $\tau = 6$ μs. The DEER spectrum of the target spins is taken both when the sequence time sits at $\tau = 6$ μs, and when the sequence time is within the zeroth peak of spin echo experiment at $\tau = 1$ μs. The DEER dip at $\tau = 1$ μs has smaller linewidth and larger contrast. One

of the reason could be the resonance of the target spin drifted during the DEER experiment at $\tau =$ 6 μs due to mechanical or thermal reasons, as the total experiment time of DEER experiment at $\tau = 6$ μs is 15 μs (12 μs of microwave sequence and 3 μs of optical readout), 3 times longer than the total experiment time of 5 μs when $\tau = 1$ μs.

The electron spin in Cu^{2+} has hyperfine splitting and anisotropy in g-factor, which should lead to multiple resonances in the spectrum. Before we lost $NV2$, three resonances are found. Figure 5.14 shows the other two resonances based on spin echo with half length $\tau = 6$ μs. The pulse length used for the resonance at 811 MHz is 130 ns and the pulse length for the resonance at 1105 MHz is 380 ns.

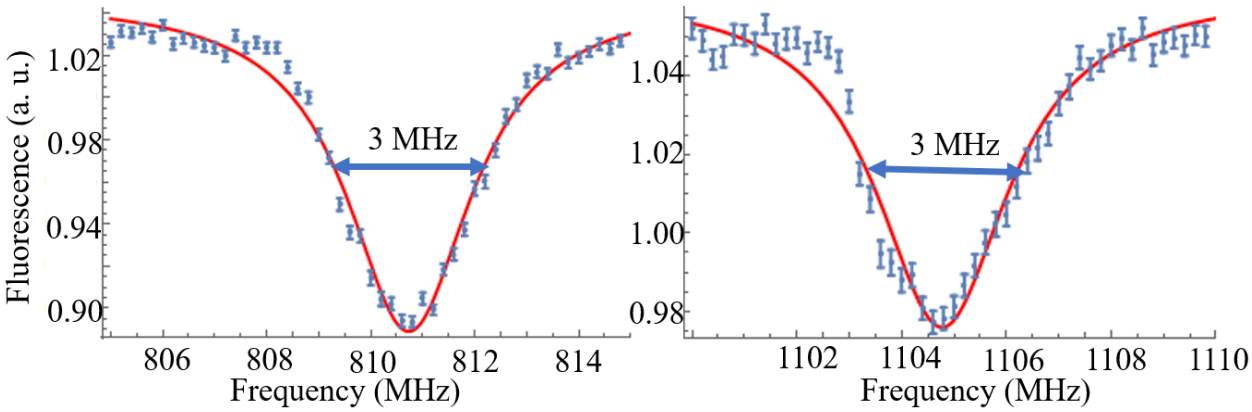

Figure 5.14 DEER spectrum of the target spin with $NV2$ based on spin echo sequences with $\tau = 6$ μs half length. The pulse width for the target spin on the left is 130 ns. The pulse width for the target spin on the right is 380 ns. The π pulse width for the NV center is 20 ns. The resonant frequency of NV center is 2.4 GHz. Red curves are Lorentzian fit functions.

The three resonances at 486 MHz, 811 MHz, 1105 MHz with $\sim 3 \times 10^2$ MHz spacing are likely due to the hyperfine structure of Cu^{2+}.

5.3.2 DEER Rabi Experiment

The experimental sequence of DEER Rabi experiment is shown in Figure 5.15. With the frequency of target spin driving field fixed at the resonance frequency, the pulse length is scanned monitoring the fluorescence. The resonant frequency to drive the target spin must be measured prior to this experiment, and the result of the DEER Rabi experiment can be used to adjust the pulse length

used in DEER frequency scan and optimize the contrast. The bootstrapping steps we take to acquire a DEER spectrum with high quality after we calibrated our spin echo sequence is:

1. Perform the DEER frequency scan experiment with random driving power and random pulse length at frequency ranges where a DEER dip is expected. Considering our linewidth, each step of the frequency scan must be 2 MHz at most.
2. Keep averaging until the fluctuation in spectrum becomes smooth and repeatable dip shows up. If no dips are discovered in measured fluorescence signal, jump to another frequency range or change to another pulse length.
3. Use the estimated center value of the dip as fixed driving frequency, perform DEER Rabi experiment to find the proper pulse length.
4. Perform DEER frequency scan to get a better spectrum with higher contrast.

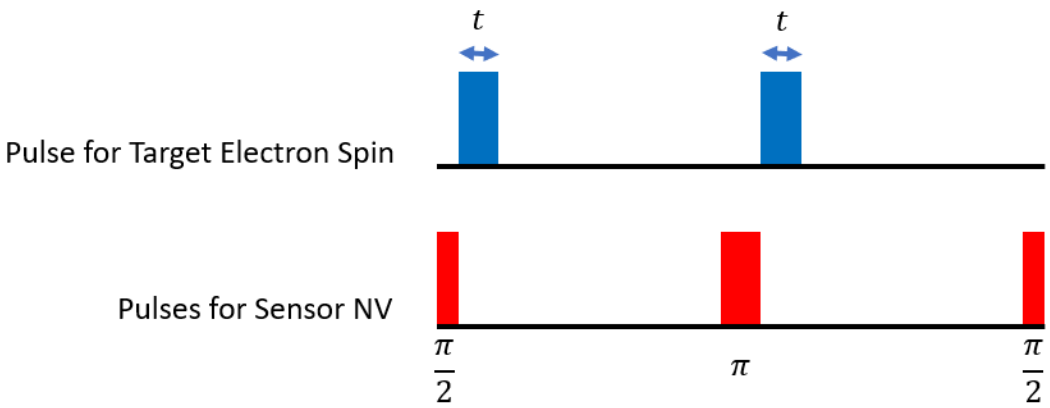

Figure 5.15 Experimental sequence of DEER Rabi experiment. The frequency of the target spin driving pulse is fixed to the resonant frequency, while the pulse length is under scanning.

The result of DEER Rabi experiment on $NV1$ is shown in Figure 5.16. As described in the previous section 5.2.3, the expected signal for the situation of single target spin can be calculated assuming the prefactor $\gamma_e \tau \lambda(\vec{e}_B \cdot \vec{e}_i)$ and microwave parameters (see Appendix A.9.2). We chose the proper value of prefactor $\gamma_e \tau \lambda(\vec{e}_B \cdot \vec{e}_i) = 5.8$ and microwave parameters $\Omega = 1.12$ MHz so that the calculated expectation is similar to our observation as shown in Figure 5.16 bottom. The pulse length of 0.1 μs used in our fine DEER frequency scan experiment is chosen from this result to optimize the contrast.

The DEER Rabi experiment on $NV2$ with resonant frequency of 486 MHz is shown in Figure 5.17. As $NV2$ is unlikely a surface NV, the model with a large number of target spins discussed in section 5.2.4 is used as theoretical prediction. In the calculation, we chose the proper

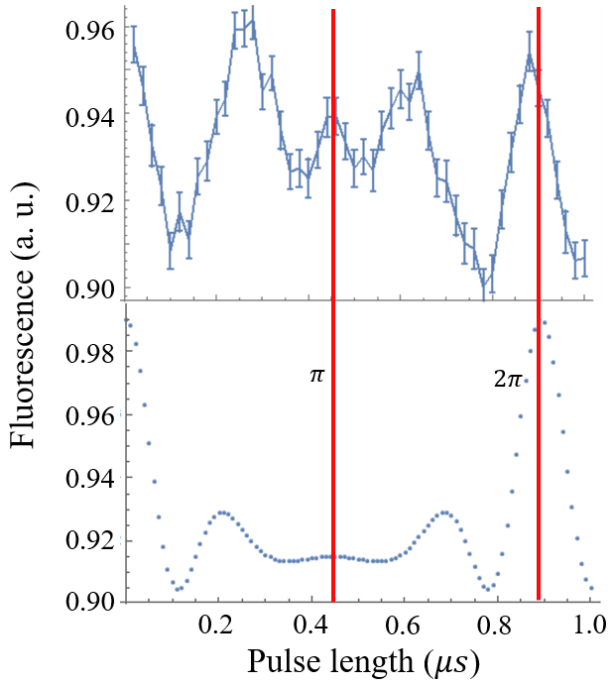

Figure 5.16 DEER Rabi experiment on $NV1$ (top) compared to calculated expectation with single target spin (bottom, see previous section 5.2.3). The red lines mark the pulse lengths of π and 2π pulse. The pulse width and frequency for NV center is the same as in section 5.3.1. The frequency for target spin is 495 MHz.

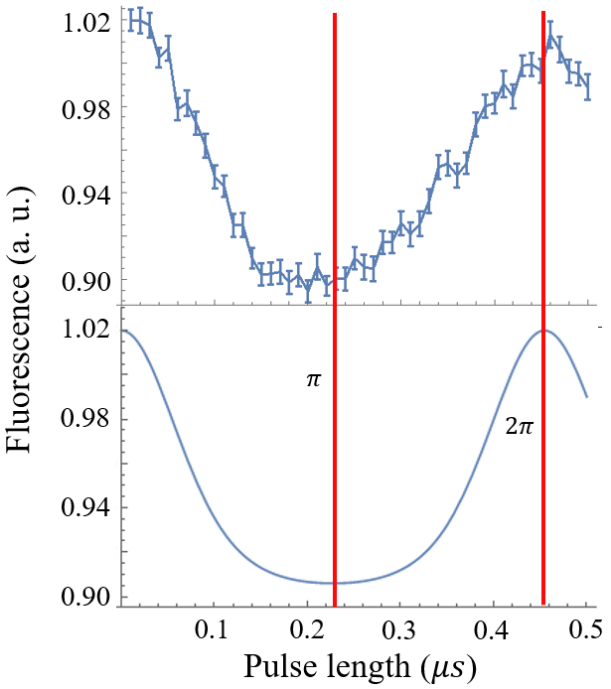

Figure 5.17 DEER Rabi experiment on $NV2$ (top) compared to calculated expectation with large number of target spins (bottom). The red lines mark the pulse lengths of π and 2π pulse. The pulse width and frequency for NV center is the same as in section 5.3.1. The frequency for target spin is 486.4 MHz.

value of prefactor $\frac{2n\bar{c}^2}{3} = 2.5$ and microwave parameters $\Omega = 2.2$ MHz so that the calculated expectation is similar to our observation as shown in Figure 5.17 bottom.

5.4 DISCUSSION OF DEER SPECTRUM

The observed DEER spectrum is not consistent with a powder spectrum of Cu^{2+} ions. This implies that the commonly used powder spectrum may be inappropriate for our situation. Unlike typical solid-state EPR apparatuses, our NV center is only sensitive to the target electrons close by, there may not be sufficient $CuCl_2$ crystals to form a powder pattern.

5.4.1 Density of Copper Ions and Thickness of Polymer

To estimate the number of Cu^{2+} ions we are sensing with our NV center, we assume the Cu^{2+} ions and Cl^- ions are randomly distributed in the poly-L-lysine residuals. The mass of poly-L-lysine in the droplet ($\sim$5 μL $= \sim$5 mm^3) is about 5×10^{-7} g. Given the density of poly-L-lysine as $1.125\,\mathrm{g/cm^3}$ ($1.125 \times 10^{-3}\,\mathrm{g/mm^3}$), the volume of poly-L-lysine can be calculated as 4.4×10^{-4} mm^3. Similarly, based on the mass and the density, the volume of $CuCl_2$ crystals is estimated as 3.4×10^{-5} mm^3, less than one tenth of the volume of poly-L-lysine. The total volume is about 5×10^{-4} mm^3, which contains 0.5 nmol of Cu^{2+} ions. The average number of Cu^{2+} ions per unit volume can be estimated as $0.6\ /\mathrm{nm^3}$.

Given the volume of poly-L-lysine as 4.4×10^{-4} mm^3, and the area of the dry marks on the diamond surface as about 2 mm × 2 mm, the average thickness of poly-L-lysine is about 1×10^2 nm. Considering the fact that the edge of the droplet accumulates the most poly-L-lysine (forming dry marks), the actual thickness should be much less than 1×10^2 nm at the central working area.

5.4.2 Estimation of Sensing Volume

As discussed in section 5.2.4, all electron spins from Cu^{2+} ions in the space contributes to the DEER signal. Setting up the boundary of sensing volume depends on our choice of detectability threshold, and the shape of boundary we choose.

As shown in Figure 5.10, the parameter $n\overline{c^2}$ determines the depth of DEER dips. We can choose our threshold of detectability based on the depth of DEER dips. If the parameter $n\overline{c^2}$ is too small, the depth of DEER dip would be too small to be detectable. Based on the expression of measured fluorescence in section 5.2.4, we plot the normalized depth as a function of parameter $n\overline{c^2}$ in Figure 5.18. We choose our threshold of detectability as $n\overline{c^2} = 1$. Any DEER dips from $n\overline{c^2} < 1$ is treated as undetectable.

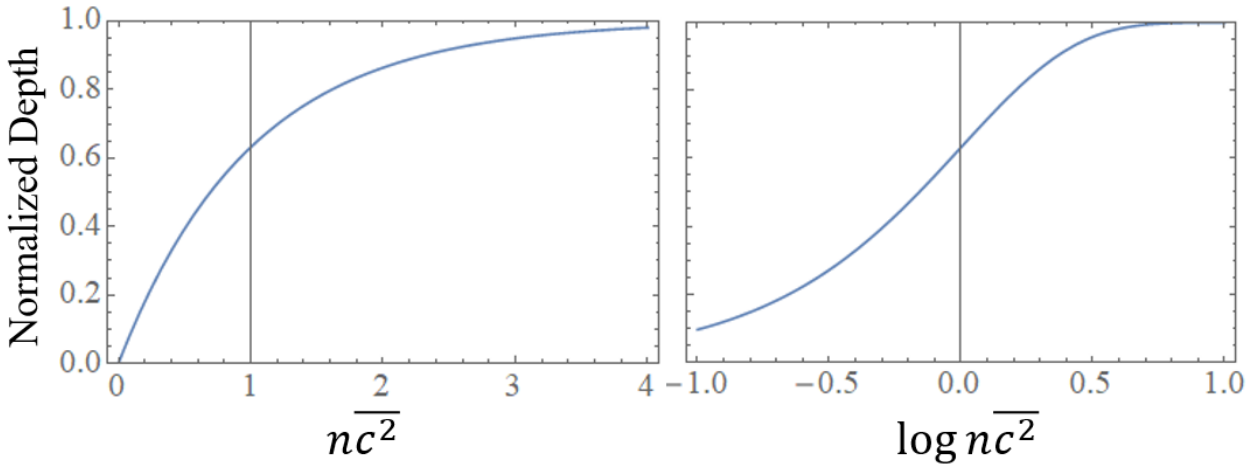

Figure 5.18 Normalized depth of DEER dips as a function of parameter $n\overline{c^2}$. Our threshold of detectability is chosen as $n\overline{c^2} = 1$, marked with black vertical lines in the plots. Any DEER signal with $n\overline{c^2} < 1$ is treated as undetectable.

Based on the theory of DEER in section 5.2.3 and 5.2.4, all electron spins in the space contributes to the parameter $n\overline{c^2}$ as

$$n\overline{c^2} = \sum_{k=1}^{n} c_k^2 \tag{5.19}$$

with

$$|c_k| = \frac{\mu_0 \gamma_e^2 \hbar \tau}{8\pi} \cdot \frac{1}{r_k^3} \cdot \frac{|\vec{e}_B \cdot \vec{e}_{ik}|}{\|3(\vec{e}_{rk} \cdot \vec{e}_z)\vec{e}_{rk} - \vec{e}_z\|} \tag{5.20}$$

The factor $\frac{|\vec{e}_B \cdot \vec{e}_{ik}|}{\|3(\vec{e}_{rk} \cdot \vec{e}_z)\vec{e}_{rk} - \vec{e}_z\|}$ varies for different electrons. In our estimation it is approximated as unity for simplicity. As a result, $|c_k|$ depends only on r, the distance between the NV center and each target electron spin:

$$|c_k| = c(r) = \kappa \cdot \frac{1}{r^3} \tag{5.21}$$

where $\kappa = \frac{\mu_0 \gamma_e^2 \hbar \tau}{8\pi} \approx (9.9 \text{ nm})^3$ is a constant. The contribution to the parameter $n\overline{c^2}$ for each target electrons in space can be binned into spherical shells with different distances to the NV center. We can define our sensing volumes as spherical caps shown in Figure 5.19. This simplified spherical cap model of sensing volume estimation is inherited from [114]. The boundary chosen in [114] for their sensing volume is that 70 % of the total signal is contributed by the target spins inside the sensing volume of spherical cap, while the other 30 % is from the negligible volume. They can even estimate the depth of NV center, h, based on their measured signals.

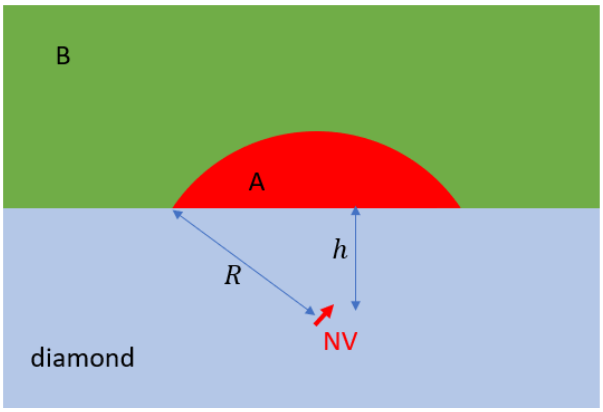

Figure 5.19 Schematic drawing of sensing volume. The volume A, spherical cap with radius *R* shown in red, is our sensing volume. The volume B, the negligible volume refers to everywhere else doesn't contributes sufficient to be detectable.

In our case, the target spins are not uniformly distributed in space but maybe concentrated in crystallites that randomly distributed in the polymer, as discussed in section 5.4.1. While the 70 % threshold based on uniform distribution of target spins is not appropriate for us, we can still get a rough estimation of our sensing volume based on the following rules:

1. Assuming maximum number density of electron spins as inside crystallites, the contribution from sensing volume is detectable ($\sum_A c_k^2 \geq 1$).
2. The contribution from negligible volume is not detectable ($\sum_B c_k^2 < 1$), even for maximum number density of electron spins as inside crystallites.

Based on these rules we imply at least some information about the sensing volume:

1. The depth of NV center cannot exceed 170 nm, in order to sense a detectable signal from our target electron spins. In fact, as our DEER Rabi experiment fits to the situation that $\sum_A c_k^2 = 5$, as shown in section 5.3.2, the depth of NV center should not be larger than $100nm$.
2. Assuming the depth of NV center $h < 100nm$, the radius of the boundary of negligible volume is 230~250 nm. Anything outside this radius is in negligible volume and can be neglected.

Taking all information mentioned above into consideration, we end up with a sensing volume model using estimations as shown in Figure 5.20. It is estimated that the depth of NV center is 70 nm and a $(50\ \text{nm})^3$ crystallite falls occasionally into the sensing volume with radius of 240 nm.

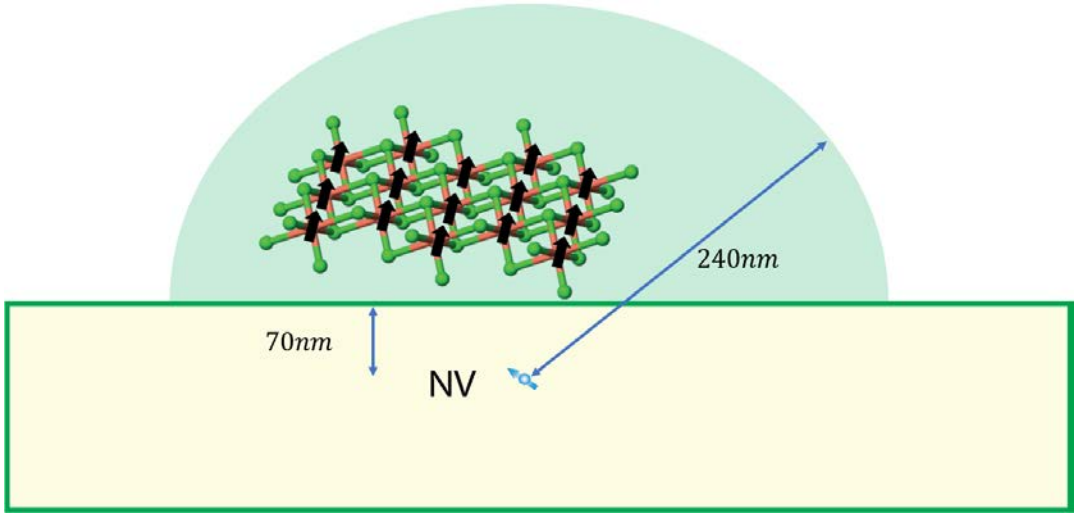

Figure 5.20 Schematic drawing of our sensing volume model. Copper chloride dihydrate crystallites are schematically shown as lattice and copper ion spins are marked as black arrows. It is estimated that a $(50\ \text{nm})^3$ crystallite falls occasionally into the sensing volume with radius of 240 nm.

5.4.3 Solid-State Spectrum

The Cu^{2+} ion contains an unpaired electron in its $3d_{x^2-y^2}$ orbital. The Hamiltonian of a single Cu^{2+} ion electron spin can be written as

$$H = -\frac{\mu_B}{\hbar}\vec{B}\cdot\overleftrightarrow{g}\cdot\vec{S} + \vec{I}\cdot\overleftrightarrow{A}\cdot\vec{S} \tag{5.22}$$

where $\overleftrightarrow{g}$ is the anisotropic g-tensor, and $\overleftrightarrow{A}$ is the hyperfine interaction tensor. The first term is the electron Zeeman interaction. The anisotropy in g-tensor comes from spin-orbit coupling and is typical in transition metal ions. For Cu^{2+} ion, the g-tensor is axial ($g_x = g_y < g_z$). The second term is the hyperfine interaction due to the copper nuclear with $I = \frac{3}{2}$. The quadrupole interaction of copper is neglected. For Cu^{2+} ions in a single crystal, the principal axes of the $\overleftrightarrow{g}$ and $\overleftrightarrow{A}$ should be parallel to the crystalline orientation, which is arbitrary in our situation. The diagonal forms of g-tensor and hyperfine interaction tensor along the crystalline orientation are

$$\overleftrightarrow{g} = \begin{pmatrix} g_\perp & 0 & 0 \\ 0 & g_\perp & 0 \\ 0 & 0 & g_\parallel \end{pmatrix}$$

$$\overleftrightarrow{A} = \begin{pmatrix} A_\perp & 0 & 0 \\ 0 & A_\perp & 0 \\ 0 & 0 & A_\parallel \end{pmatrix}$$

where $g_\perp = 2.0835$, $g_\parallel = 2.415$, $A_\perp = 30\ \text{MHz}/\hbar$, $A_\parallel = 339\ \text{MHz}/\hbar$. Numerical simulation is needed for calculating the resonances from Cu^{2+} ions in a single crystal.

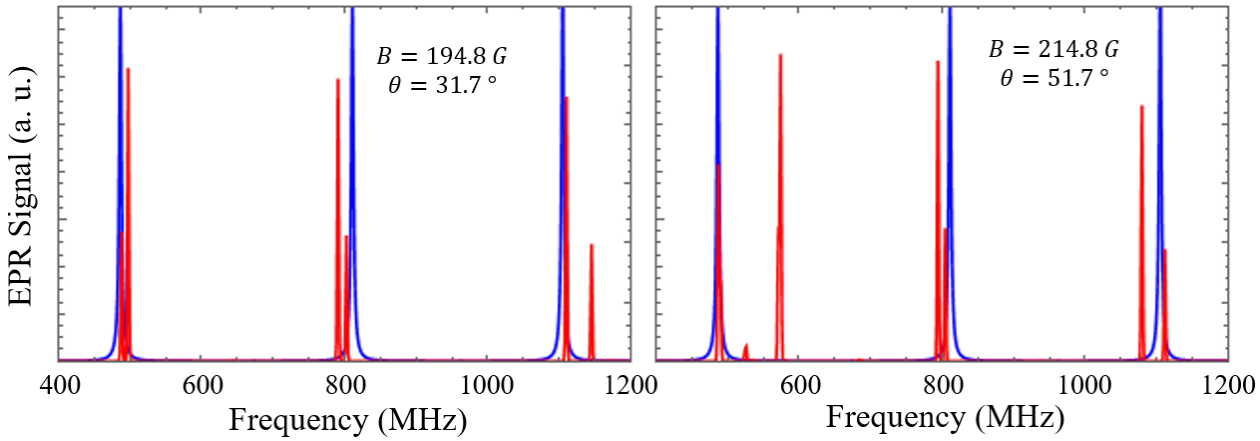

Figure 5.21 Simulation of EPR spectrum of $CuCl_2$ single crystal, shown in red. The blue peaks mark the position of resonances observed in our DEER spectrum.

The numerical simulation of EPR spectrum of $CuCl_2$ single crystal is done with EasySpin [126].[15] The EasySpin simulation uses the assumption that the Cu^{2+} ions are in a crystallite and the axes of all Cu^{2+} ions are aligned in the same direction. By adjusting the external magnetic field B and the angle θ between the principal axis and magnetic field, we can minimize the sum of

[15] See Appendix A.9.3 for EasySpin codes.

squared distance between the peaks from the simulation and the resonances we observed (χ^2). We found two different parameter sets (B, θ) which gives reasonably good fits to our observed spectrum. The comparison between the numerical simulation and the observed resonances in our DEER spectrum is shown in Figure 5.21. For the first local minimum of χ^2, the value of external magnetic field is $B = 194.8 \pm 0.5$ G and the value of the angle between principal axis and magnetic field is $\theta = 31.7 \pm 0.7\,°$.[16] And for the second local minimum of χ^2, the value of external magnetic field is $B = 214.8 \pm 0.5$ G and the value of the angle between principal axis and magnetic field is $\theta = 51.75 \pm 0.25\,°$. Because of the axial symmetry of $\overleftrightarrow{g}$ and $\overleftrightarrow{A}$ tensors, the exact same spectrum is reproduced at $\theta' = 180\,° - \theta$. Equally good fits can be found at $B = 194.8 \pm 0.5$ G, $\theta = 148.3 \pm 0.7\,°$ and $B = 214.8 \pm 0.5$ G, $\theta = 128.25 \pm 0.25\,°$. See Appendix A.8 for details of the goodness of fit.

5.5 CONCLUSION

The DEER signals we observed on $NV1$ and $NV2$ are the first successful experiment in our lab in external electron spin sensing with single NV centers. Compared to DEER experiments in other groups, our DEER spectrum has narrow linewidth and high contrast. The DEER frequency scan experiment and the DEER Rabi experiment are performed in a bootstrapping procedure to acquire target spin spectrum with high quality. By simulating the DEER Rabi experiment, we point out that the calibration of the π pulse for the target spin in [54] is incorrect, and that the fast decaying oscillations in the signal can be used as fingerprints of single target spins. Our observed results for the DEER spectrum are not consistent with a powder pattern, but are well fit to a small range of angles for the principal axis of the anisotropic tensors. This seems to imply that there is single crystal of $CuCl_2$ falling into our detection volume. Further study along with other imaging techniques may be needed to verify our explanation. These results open the door to further exploration in external electron spin sensing with NV centers and its applications in chemistry and biology.

[16] See Appendix A.8 for details of estimation of the confidence intervals.

On the other hand, there are still questions remaining unsolved to our observation. For example, the linewidth we observed is much narrower than our calculated value, exceeding the limit of power broadening with the pulse length we used. The measurement of depolarization time T_1 of target spins needs to be done, because the sensitivity of DEER technique is limited by T_1.

Further improvements of our DEER experiment include using NV centers closer to surface with less implantation energy, and less concentration of target spins for single target spin sensing. The immersion oil refreshing problem can be solved by switching to dry objectives with correction collar, at the cost of optical efficiency and resolution. With unlimited time working on the same NV center, we hope more resonance frequencies could be found and we can prove the signal we saw is indeed from Cu^{2+} ions with stronger evidence.

6.0 SUMMARY AND FUTURE WORK

This chapter summarizes the thesis and provides a brief outlook to future directions.

6.1 SUMMARY OF THESIS

Nitrogen-Vacancy centers (NV centers) are defects in diamond with optically measurable electronic spins. These isolated single spins are important quantum system used in quantum metrology, quantum information and quantum computing, quantum optics and a variety of applications in nanoscience. A brief introduction to the NV centers researches, specifically researches on NV center magnetometry, is provided in chapter 1.

The background knowledge of NV centers is explained in chapter 2, including the crystalline structure, electronic states, optical properties and optically detected magnetic resonance (ODMR). Some of the well-known existing technologies of coherent manipulation are also discussed, such as Rabi oscillation, Ramsey experiment and spin echo experiment.

In chapter 3, we present measurement of Berry phase with a single NV center in diamond. The spin qubit is manipulated geometrically by applying microwave radiation that creates a rotating effective magnetic field, and the resulting Berry phase signal is observed by cancelling out the dynamic phase with spin echo sequence. A series of test experiments are performed to verify our control field parameters. The deviation of the observed Berry phase from our theory is explained by systematic errors in our control field. The study on dephasing shows that the dynamic dephasing results from fast fluctuations in control field is responsible for the decay of signal. Since the geometric phase is intrinsically connected to dynamic phase, geometric phase cannot be experimentally isolated from dynamic phase without accurate control of the driving fields. Our work also explored the limits to the fidelity of geometric phase gates on a single qubit and showed

that the fidelity is limited by the noise in the signal generator which is not canceled by the spin echo sequence.

Chapter 4 shows our efforts made towards the implementation of a scanning diamond probe microscope (SDPM). We realize that such a diamond-based SPM system with sub-nm resolution is inherently difficult to build. Only a handful of research groups around the world are successful in experimental implementation of SPDM system with diamond probe. Meanwhile, the atomic force microscope (AFM) in our lab suffers from acoustic and thermal noise for scanning image with sub-nm resolution and needs to be isolated better from its environment.

In chapter 5, we report results of DEER experiments with NV center. The DEER signals we observed on $NV1$ and $NV2$ are the first successful experiment in our lab in external electron spin sensing with single NV centers. The DEER frequency scan experiment and the DEER Rabi experiment are performed in a bootstrapping procedure to acquire target spin spectrum with high quality. The multiple resonances we observed in our DEER spectrum are evidence of the detection of external copper ion spins. Compared to DEER experiments in other groups, our DEER spectrum has narrow linewidth and high contrast. By simulating the DEER Rabi experiment, we point out that the calibration of the π pulse for the target spin in [54] is incorrect, and that the fast decaying oscillations in the signal can be used as fingerprints of single target spins. These results open the door to further exploration in external electron spin sensing with NV centers and its applications in chemistry and biology.

6.2 FUTURE WORK

Our work on sensing external electron spins with single NV centers is just a starting point. There are still questions remaining unsolved to our observation. For example, the linewidth we observed is much narrower than our calculated value, exceeding the limit of power broadening with the pulse length we used. The measurement of depolarization time T_1 of target spins needs to be done, because the sensitivity of DEER technique is limited by T_1. Further improvements of our DEER experiment include using NV centers closer to surface with less implantation energy, and less concentration of target spins for single target spin sensing. The immersion oil refreshing problem can be solved by switching to dry objectives with correction collar, at the cost of optical efficiency

and resolution. Fabrication techniques on diamond needs improvement to improve the quality of our surface NV centers. With unlimited time working on the same NV center, we hope more resonance frequencies could be found and we can prove the signal we saw is indeed from Cu^{2+} ions with stronger evidence. If advanced e-beam lithography (EBL) and metal deposition techniques on bulk diamond is well developed in our cleanroom, the microwave waveguide could be fabricated on diamond surface directly, which would simplify our experimental setup and increase efficiency. Once our DEER technique is improved in stability, we can search for signals from single target electron spin labels on protein molecules at the surface of diamond and study the dynamics of such large molecules.

APPENDIX A

SUPPLEMENTARY MATERIALS IN THEORY AND CALCULATION

A.1 COLLECTIVE ELECTRONIC STATES OF NV CENTER

As mentioned in section 2.1, the occupancies of 3 molecular orbitals by 4 electrons forms the collective electronic states of NV centers. The occupancies of molecular orbitals for the lowest collective electronic states are schematically shown in Figure A.1.

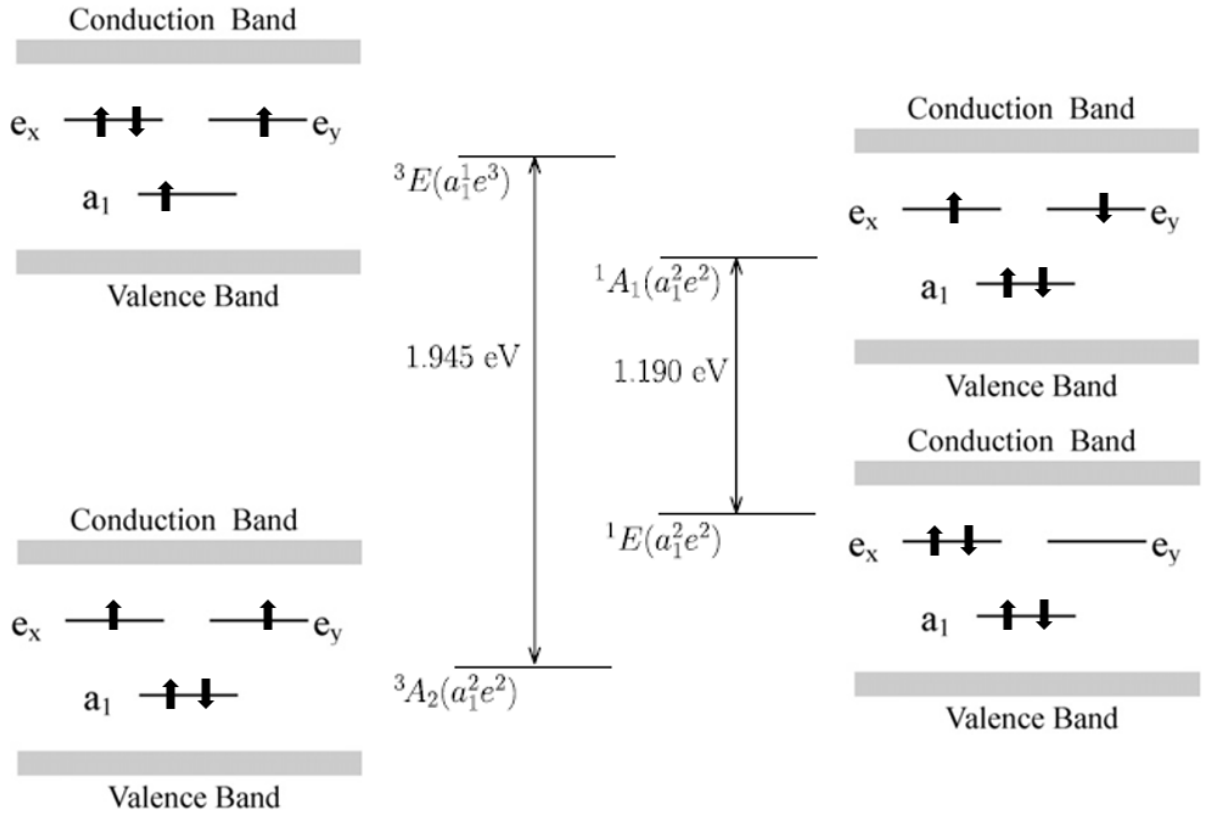

Figure A.1 Collective electronic states and corresponding occupancies of molecular orbitals.

The wave functions of collective electronic states can be expressed by product of wave functions of individual electrons. For example, the wave function of the $|m_s = 1\rangle$ state (as shown at bottom left in Figure A.1) from the orbital ground state ${}^3A_2$ can be written as,

$$\left| {}^3A_2, m_s = 1 \right\rangle = |a_1\rangle \otimes |\bar{a}_1\rangle \otimes |e_x\rangle \otimes \left|e_y\right\rangle = \left|a_1 \bar{a}_1 e_x e_y\right\rangle \qquad (A.1)$$

where the bar notation represents the opposite spin direction of electron. The wave functions of the collective electronic states of interest is listed in Table A.1.

Table A.1 The configuration and spin-orbit states of the NV center [66].

Occupancy	Symmetry	Orbital Degeneracy	Spin Degeneracy	Spin-Orbit State
$a_1^2 e^2$	${}^3A_2$		$m_s = 0$	$\left\|a_1 \bar{a}_1 \bar{e}_x e_y\right\rangle + \left\|a_1 \bar{a}_1 e_x \bar{e}_y\right\rangle$
			$m_s = 1$	$\left\|a_1 \bar{a}_1 e_x e_y\right\rangle$
			$m_s = -1$	$\left\|a_1 \bar{a}_1 \bar{e}_x \bar{e}_y\right\rangle$
	${}^1E$	x		$\|a_1 \bar{a}_1 e_x \bar{e}_x\rangle - \left\|a_1 \bar{a}_1 e_y \bar{e}_y\right\rangle$
		y		$\left\|a_1 \bar{a}_1 \bar{e}_x e_y\right\rangle - \left\|a_1 \bar{a}_1 e_x \bar{e}_y\right\rangle$
	${}^1A_1$			$\|a_1 \bar{a}_1 e_x \bar{e}_x\rangle + \left\|a_1 \bar{a}_1 e_y \bar{e}_y\right\rangle$
$a_1^1 e^3$	${}^3E$	x	$m_s = 0$	$\left\|a_1 \bar{e}_x e_y \bar{e}_y\right\rangle + \left\|\bar{a}_1 e_x e_y \bar{e}_y\right\rangle$
			$m_s = 1$	$\left\|a_1 e_x e_y \bar{e}_y\right\rangle$
			$m_s = -1$	$\left\|\bar{a}_1 \bar{e}_x e_y \bar{e}_y\right\rangle$
		y	$m_s = 0$	$\left\|a_1 e_x \bar{e}_x \bar{e}_y\right\rangle + \left\|\bar{a}_1 e_x \bar{e}_x e_y\right\rangle$
			$m_s = 1$	$\left\|a_1 e_x \bar{e}_x e_y\right\rangle$
			$m_s = -1$	$\left\|\bar{a}_1 e_x \bar{e}_x \bar{e}_y\right\rangle$

A.2 GROUND STATE OF NV CENTER

The full Hamiltonian of NV center ground state without external field can be written as,

$$\hat{H}_{gs} = \frac{1}{\hbar}\left\{ D\left[\hat{S}_z^2 - \frac{S(S+1)}{3}\right] + A_{\parallel}\hat{S}_z\hat{I}_z + A_{\perp}\left(\hat{S}_x\hat{I}_x + \hat{S}_y\hat{I}_y\right) + P\left[\hat{I}_z^2 - \frac{I(I+1)}{3}\right]\right\} \qquad (A.2)$$

where $D = 2.87$ GHz under room temperature is the fine structure splitting, $A_\parallel$ and $A_\perp$ are the axial and non-axial magnetic hyperfine parameters, and P is the nuclear electric quadrupole parameter. $A_\parallel$, $A_\perp$ and P are in MHz [18].

The influence of static electric field $\vec{E}$, static magnetic field $\vec{B}$, and strain field $\vec{\delta}$ on the ground state Hamiltonian can be written as,

$$\hat{V}_{gs} = \frac{1}{\hbar}\left\{\mu_B g_\parallel \hat{S}_z B_z + \mu_B g_\perp\left(\hat{S}_x B_x + \hat{S}_y B_y\right) + \mu_N g_N \hat{\vec{I}} \cdot \vec{B}\right\}$$
$$+\frac{1}{\hbar^2}\left\{d_\parallel (E_z + \delta_z)\left[\hat{S}_z^2 - \frac{S(S+1)}{3}\right] + d_\perp (E_x + \delta_x)\left(\hat{S}_y^2 - \hat{S}_x^2\right) + d_\perp\left(E_y + \delta_y\right)\left(\hat{S}_x \hat{S}_y + \hat{S}_y \hat{S}_x\right)\right\} \quad (A.3)$$

where μ_B is Bohr magneton, μ_N in nuclear magnetic dipole moment, $d_\parallel$ and $d_\perp$ are the axial and non-axial components of electric dipole moment. The electric dipole moment is in $10^{-1}\frac{1}{\hbar}$ Hz/(V/m) [18]. The anisotropy in g-factor is negligible for NV centers. The first two terms are from the electron Zeeman effect and the third term is from nuclear Zeeman effect.

Since our Rabi frequency of microwave driving field is in the order of 10 MHz, neglecting all terms in MHz or smaller, the Hamiltonian can be written as,

$$\hat{H}_{gs} = \frac{1}{\hbar}\left(DS_z^2 + \mu_B g \hat{\vec{S}} \cdot \vec{B}\right) \quad (A.4)$$

When the external magnetic field is aligned with the $N - V$ axis, the Hamiltonian of NV center ground state becomes the form in section 2.4.1.

A.3 ROTATING FRAME

The rotating frame is widely used in nuclear magnetic resonance (NMR) techniques and other spin dynamics. The time-dependent Hamiltonian of a rotating magnetic field is transformed into a static effective Hamiltonian in the rotating frame. Assume the quantum system is in state $|\psi(t)\rangle$, the definition of rotating frame is the transform to the interaction picture such that

$$\left|\tilde{\psi}(t)\right\rangle = R_z\left(-\omega_{ref} t\right)|\psi(t)\rangle \quad (3.25, A.5)$$

$$|\psi(t)\rangle = R_z\left(\omega_{ref} t\right)\left|\tilde{\psi}(t)\right\rangle \quad (A.6)$$

where the R_z refers to the rotation operator along the z axis, defined as

$$R_z(\phi) = e^{-i\phi S_z/\hbar} \tag{A.7}$$

The time-evolution of the state $|\tilde{\psi}(t)\rangle$ in the rotating frame can be derived by applying the transform in equation A.6, $|\psi(t)\rangle = R_z(\omega_{ref}t)|\tilde{\psi}(t)\rangle$, to the Schrödinger equation in the lab frame,

$$H|\psi(t)\rangle = i\hbar\frac{\partial}{\partial t}|\psi(t)\rangle \tag{A.8}$$

As a result, we have the time-evolution of the state $|\tilde{\psi}(t)\rangle$ in the rotating frame as

$$i\hbar\frac{\partial}{\partial t}|\tilde{\psi}(t)\rangle = -\omega_{ref}S_z|\tilde{\psi}(t)\rangle + R_z(-\omega_{ref}t)HR_z(\omega_{ref}t)|\tilde{\psi}(t)\rangle \tag{A.9}$$

Define the effective Hamiltonian in the rotating frame as

$$\tilde{H} = -\omega_{ref}S_z + R_z(-\omega_{ref}t)HR_z(\omega_{ref}t) \tag{A.10}$$

then we have the same Schrödinger equation for the time-evolution of state as in the lab frame

$$\tilde{H}|\tilde{\psi}(t)\rangle = i\hbar\frac{\partial}{\partial t}|\tilde{\psi}(t)\rangle \tag{A.11}$$

Any results based on the Schrödinger equation in the lab frame can be applied to the state in rotating frame with the effective Hamiltonian in rotating frame, including the Berry phase in chapter 3.

The rotating frame is used to transform an oscillating Hamiltonian in the lab frame into a static effective Hamiltonian in the rotating frame. Consider a spin in a longitudinal static magnetic field and an oscillating transverse magnetic field with frequency ω. The oscillating transverse field is divided into two circularly polarized transverse fields

$$\begin{aligned}\vec{B}_\perp(t) = &\frac{B_\perp}{2}\left[\cos(\omega t + \phi)\,\vec{e}_x + \sin(\omega t + \phi)\,\vec{e}_y\right] \\ &+ \frac{B_\perp}{2}\left[\cos(-\omega t - \phi)\,\vec{e}_x + \sin(-\omega t - \phi)\,\vec{e}_y\right]\end{aligned} \tag{A.12}$$

According to rotating wave approximation [71], only the first term is resonant and important. By neglecting the anti-rotating term, the Hamiltonian of the system in the lab frame can be written as

$$H(t) = -\gamma B_z S_z - \gamma\frac{B_\perp}{2}\left[R_z(\omega t + \phi)S_x R_z(-\omega t - \phi)\right] \tag{A.13}$$

Now we choose a rotating frame where $\omega_{ref} = \omega$, meaning the rotating frame is rotating at the same angular velocity as the transverse magnetic field. The effective Hamiltonian in this rotating frame can be written as

$$\tilde{H} = -\omega_{ref} S_z - \gamma B_z S_z - \gamma \frac{B_\perp}{2} R_z(-\omega_{ref} t) R_z(\omega t + \phi) S_x R_z(-\omega t - \phi) R_z(\omega_{ref} t)$$

$$\tilde{H} = (\omega_L - \omega) S_z + \Omega_\perp R_z(\phi) S_x R_z(-\phi) \qquad (A.14)$$

where ω_L is the Larmor frequency of the system and $\Omega_\perp$ is the Rabi frequency of the transverse field. This effective Hamiltonian is time-independent and easy to deal with.

A.4 CONTINUOUS WAVE ODMR

In continuous wave optically detected magnetic resonance (CW ODMR) experiments, both green light illumination and microwave driving field are delivered to the single NV center.

As shown in Figure A.2, a two-level model is used to infer the behavior of CW ODMR experiments [127]. The green light illumination provides a pumping rate Γ_P from $|1\rangle$ to $|0\rangle$, the microwave driving field drives the system coherently with Rabi frequency Ω_R and detuning Δ, while the longitudinal and transverse relaxation rate, γ_1 and γ_2 respectively, are mixing the two states.

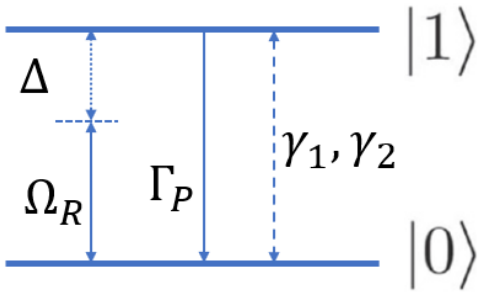

Figure A.2 Schematic drawing of two-level model for continuous wave ODMR experiments.

The time evolution of the density matrix of the two-level system can be solved from the equation of motion (Bloch equations). The Bloch equations are

$$\begin{cases} \dot{\rho}_{00} = -\frac{i\Omega_R}{2}(\rho_{01} - \rho_{10}) - \frac{\gamma_1}{2}(\rho_{00} - \rho_{11}) + \Gamma_P \rho_{11} \\ \dot{\rho}_{11} = \frac{i\Omega_R}{2}(\rho_{01} - \rho_{10}) + \frac{\gamma_1}{2}(\rho_{00} - \rho_{11}) - \Gamma_P \rho_{11} \\ \dot{\rho}_{01} = -\left(\gamma_2 + \frac{\Gamma_P}{2} - i\Delta\right)\rho_{01} - \frac{i\Omega_R}{2}(\rho_{00} - \rho_{11}) \\ \dot{\rho}_{10} = -\left(\gamma_2 + \frac{\Gamma_P}{2} + i\Delta\right)\rho_{10} + \frac{i\Omega_R}{2}(\rho_{00} - \rho_{11}) \end{cases} \qquad (A.15)$$

Assuming the CW ODMR signal can be written as $S(\Delta) = \alpha\rho_{00} + \beta\rho_{11}$, where α and β are phenomenological parameters to account for the difference in fluorescence intensities between $|0\rangle$ and $|1\rangle$ states, the CW ODMR signal will have the form

$$S(\Delta) = S(\infty)\left[1 - \frac{C\Delta\nu^2}{\Delta^2 + \Delta\nu^2}\right] \quad (A.16)$$

where the linewidth $\Delta\nu$ can be calculated as

$$\Delta\nu = \sqrt{\left(\gamma_2 + \frac{\Gamma_P}{2}\right)^2 + \Omega_R^2 \frac{\gamma_2 + \frac{\Gamma_P}{2}}{\gamma_1 + \Gamma_P}} \quad (A.17)$$

and the contrast C as

$$C = \Theta \cdot \frac{\Gamma_P}{\Gamma_P + \gamma_1(1-\Theta)} \cdot \frac{\Omega_R^2}{\Omega_R^2 + \left(\gamma_2 + \frac{\Gamma_P}{2}\right)(\gamma_1 + \Gamma_P)} \quad (A.18)$$

where $\Theta = (\alpha - \beta)/(2\alpha)$. Taking inhomogeneous broadening into account, the total linewidth $\Delta\nu_{tot}$ is

$$\Delta\nu_{tot} = \Delta\nu_{inh} + \Delta\nu \quad (A.19)$$

where $\Delta\nu_{inh} = \gamma_2 = \frac{1}{T_2^*}$ is the inhomogeneous broadening.

To ensure high fluorescence photon count rate from single NV center, the green light illumination is kept at high intensity. Noting that the saturation power for the optical cycle of NV center is related to the lifetime of the first excited state ${}^3E$, ~13 ns, while the saturation power for the optical pumping is related to the lifetime of metastable state ${}^1E$, ~300 ns. As a result, the optical pumping rate Γ_P is saturated to a fixed value for single NV center CW ODMR experiments. For a reasonable contrast C, the Rabi frequency of the microwave driving field is at least a few MHz, leading to power broadening of the CW ODMR linewidth of a few MHz. The overall linewidth of CW ODMR experiment of single NV centers is close to 10 MHz.

A.5 LINE SHAPE OF PULSED ODMR

The experimental sequence of pulsed ODMR is shown in Figure 2.12. As mentioned in section 2.3.2, the pulse length of the microwave pulse is set to the value so that the microwave pulse is

close to a π pulse. Strictly speaking, this is true only when the frequency of the microwave hits the resonance of the NV center during a frequency scan. When the frequency is off-resonance, the pulse is no longer close to the π pulse.

Assume we set our pulse length so that the on-resonance microwave pulse is a perfect π pulse,

$$t_p = \frac{\pi}{\Omega}$$

where the Ω is the Rabi frequency of the microwave driving field defined in section 2.4. When the microwave pulse is off-resonance, as discussed in section 2.4.1, the effective Hamiltonian as in equation 2.7 is

$$\tilde{H}_{eff} = -\Omega \cos\phi \, S_x - \Omega \sin\phi \, S_y - \Delta S_z$$

Given the initial state as $|0\rangle$, the probability of transition from $|0\rangle$ to $|1\rangle$ after the microwave driving pulse can be calculated as

$$P = \frac{\Omega^2}{\Omega^2 + \Delta^2} \sin^2 \frac{\pi\sqrt{\Omega^2 + \Delta^2}}{2\Omega} \qquad (A.20)$$

where the detuning Δ is defined as the difference between the microwave frequency and the frequency of the NV center. The resulting line shape is shown in Figure A.3.

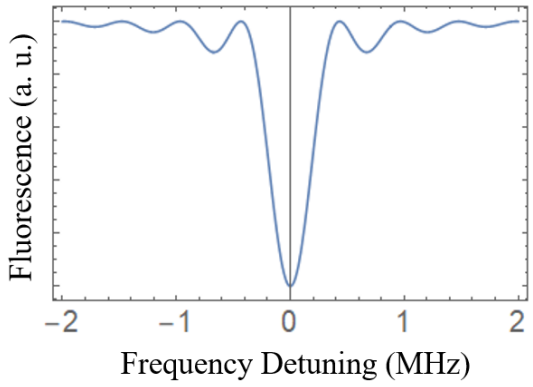

Figure A.3 Theoretical prediction of line shape of pulsed ODMR spectrum with a perfect π pulse.

A.6 DEPHASING OF RAMSEY EXPERIMENT

As discussed in section 2.4.3, the expected probability in $|0\rangle$ after the Ramsey sequence is given by

$$Pr(|0\rangle) = \frac{1 - \cos(|\gamma_e|B_1 t)}{2}$$

This probability is indirectly measured by measuring the fluorescence intensity. Since we do not have single shot measurement of spin state, the measured fluorescence signal is an ensemble average over many repetitions. Now we consider the inhomogeneous dephasing by adding a random fluctuation in the external magnetic field B_1,

$$B_1 \to B_1 + \delta B$$

where the random fluctuation δB follows normal distribution $\delta B \sim \mathcal{N}(0, \sigma_B^2)$. The measured fluorescence signal should be an ensemble average over δB,

$$Pr(|0\rangle) = \langle \frac{1 - \cos[|\gamma_e|(B_1 + \delta B)t]}{2} \rangle_{\delta B} = \frac{1}{2} - \frac{1}{2} \langle \cos[|\gamma_e|(B_1 + \delta B)t] \rangle_{\delta B} \qquad (A.21)$$

The probability density function of the normally distributed random variable δB is

$$p(\delta B) = \frac{1}{\sqrt{2\pi\sigma_B^2}} e^{-\frac{\delta B^2}{2\sigma_B^2}} \qquad (A.22)$$

Using the formula

$$\langle f(x) \rangle_x = \int_{-\infty}^{\infty} f(x) p(x) dx \qquad (A.23)$$

The expected probability in $|0\rangle$ can be calculated as

$$\begin{aligned} Pr(|0\rangle) &= \frac{1}{2} - \frac{1}{2} \int_{-\infty}^{\infty} \cos[|\gamma_e|(B_1 + \delta B)t] \frac{1}{\sqrt{2\pi\sigma_B^2}} e^{-\frac{\delta B^2}{2\sigma_B^2}} d(\delta B) \\ &= \frac{1}{2} - \frac{1}{2} \cos(|\gamma_e|B_1 t)\, e^{-\frac{|\gamma_e|^2 \sigma_B^2 t^2}{2}} \end{aligned} \qquad (A.24)$$

Defining the inhomogeneous dephasing time $T_2^* = \frac{\sqrt{2}}{|\gamma_e|\sigma_B}$, the Ramsey oscillation with decay could be expressed by

$$Pr(|0\rangle) = \tfrac{1}{2} - \tfrac{1}{2} \cos(|\gamma_e|B_1 t)\, e^{-\frac{t^2}{T_2^{*2}}} \qquad (2.11, A.25)$$

The above discussion is based on the model of a random error on the external magnetic field. Other sources of error that leads to Ramsey decay, for example, the fluctuation in resonant frequency of NV center due to temperature fluctuation, can be treated as an effective fluctuation in external magnetic field as well.

A.7 ADIABATIC APPROXIMATION AND BERRY PHASE

For general time-dependent Hamiltonian $H(t)$, the eigenvalues and their corresponding eigenstates are also time-dependent,

$$H(t)\left|\psi_{n,t}\right\rangle = E_{n,t}\left|\psi_{n,t}\right\rangle \tag{A.26}$$

where $E_{n,t}$ is the nth eigenvalue of the instantaneous Hamiltonian and $\left|\psi_{n,t}\right\rangle$ is the corresponding eigenstate. The time-dependent wave function of a quantum system $|\psi(t)\rangle$ can be expressed as linear combination of the instantaneous basis $\{\left|\psi_{n,t}\right\rangle\}$,

$$|\psi(t)\rangle = \sum_n c_{n,t}\left|\psi_{n,t}\right\rangle \tag{A.27}$$

where $c_{n,t}$ is the complex coefficient. Plug this into the time-dependent Schrödinger equation for the wave function,

$$H(t)|\psi(t)\rangle = i\hbar\frac{\partial}{\partial t}|\psi(t)\rangle$$

we have

$$\sum_n c_{n,t}H(t)\left|\psi_{n,t}\right\rangle = \sum_n i\hbar\frac{\partial c_{n,t}}{\partial t}\left|\psi_{n,t}\right\rangle + \sum_n i\hbar c_{n,t}\frac{\partial}{\partial t}\left|\psi_{n,t}\right\rangle$$

Multiply the equation by ket state $\left\langle\psi_{m,t}\right|$, and use the orthonormality of the basis, the equation becomes

$$c_{m,t}E_{m,t} = i\hbar\frac{\partial c_{m,t}}{\partial t} + \sum_n i\hbar c_{n,t}\left\langle\psi_{m,t}\right|\frac{\partial}{\partial t}\left|\psi_{n,t}\right\rangle$$

$$c_{m,t}E_{m,t} = i\hbar\frac{\partial c_{m,t}}{\partial t} + i\hbar c_{m,t}\left\langle\psi_{m,t}\right|\frac{\partial}{\partial t}\left|\psi_{m,t}\right\rangle + \sum_{n\neq m} i\hbar c_{n,t}\left\langle\psi_{m,t}\right|\frac{\partial}{\partial t}\left|\psi_{n,t}\right\rangle \tag{A.28}$$

In order to calculate $\left\langle\psi_{m,t}\right|\frac{\partial}{\partial t}\left|\psi_{n,t}\right\rangle$, we take the time derivative of the eigenvalue equation $H(t)\left|\psi_{n,t}\right\rangle = E_{n,t}\left|\psi_{n,t}\right\rangle$,

$$\frac{\partial H}{\partial t}\left|\psi_{n,t}\right\rangle + H(t)\frac{\partial}{\partial t}\left|\psi_{n,t}\right\rangle = \frac{\partial E_{n,t}}{\partial t}\left|\psi_{n,t}\right\rangle + E_{n,t}\frac{\partial}{\partial t}\left|\psi_{n,t}\right\rangle$$

and multiply it by ket state $\left\langle\psi_{m,t}\right|$. When $n \neq m$, we have

$$\langle\psi_{m,t}|\frac{\partial H}{\partial t}|\psi_{n,t}\rangle + E_{m,t}\langle\psi_{m,t}|\frac{\partial}{\partial t}|\psi_{n,t}\rangle = E_{n,t}\,\langle\psi_{m,t}|\frac{\partial}{\partial t}|\psi_{n,t}\rangle$$

Consider non-degenerate systems only,

$$\langle\psi_{m,t}|\frac{\partial}{\partial t}|\psi_{n,t}\rangle = \frac{1}{E_{n,t} - E_{m,t}}\langle\psi_{m,t}|\frac{\partial H}{\partial t}|\psi_{n,t}\rangle \qquad (A.29)$$

When the Hamiltonian of the quantum system $H(t)$ varies slowly in time, $\frac{\partial H}{\partial t} \to 0$, all terms $\langle\psi_{m,t}|\frac{\partial}{\partial t}|\psi_{n,t}\rangle$ with $n \neq m$ can be neglected. This is the *adiabatic approximation*.

When we apply the adiabatic approximation, the formula of the coefficient simplifies to

$$c_{m,t}E_{m,t} = i\hbar\frac{\partial c_{m,t}}{\partial t} + i\hbar c_{m,t}\,\langle\psi_{m,t}|\frac{\partial}{\partial t}|\psi_{m,t}\rangle \qquad (A.30)$$

The solution of this differential equation can be written as

$$c_{m,t} = e^{i\beta_D}\cdot e^{i\beta_G}\cdot c_{m,t_0} \qquad (A.31)$$

where

$$\beta_D = -\frac{1}{\hbar}\int_{t_0}^{t} E_{m,t}dt \qquad (3.23, A.32)$$

$$\beta_G = i\int_{t_0}^{t}\langle\psi_{m,t}|\frac{\partial}{\partial t}|\psi_{m,t}\rangle dt \qquad (A.33)$$

It can be easily proved that β_G is real.

As we can see from the solution, under the adiabatic approximation, the probability that the system is at the mth eigenstate, $|c_{m,t}|^2$, does not change during the whole process. The phase β_D is referred to as dynamic phase, which is trivial and arise from the instantaneous eigenvalue of the Hamiltonian.

The time-dependent Hamiltonian can be treated as a function of multiple time-dependent parameters,

$$H(t) = H\big(R_1(t), R_2(t), \cdots R_N(t)\big) = H\left(\vec{R}(t)\right) \qquad (A.34)$$

where $\vec{R}(t)$ is a time-dependent vector in a N-dimensional parameter space. As a result, the instantaneous eigenstates can also be written as functions of $\vec{R}(t)$,

$$|\psi_{m,t}\rangle = |\psi_m\big(R_1(t), R_2(t), \cdots R_N(t)\big)\rangle = |\psi_m\big(\vec{R}\big)\rangle \qquad (A.35)$$

and the time derivative of eigenstates can be written as

$$\frac{\partial}{\partial t}|\psi_{m,t}\rangle = \frac{\partial}{\partial R_1}|\psi_m(\vec{R})\rangle \cdot \frac{dR_1}{dt} + \frac{\partial}{\partial R_2}|\psi_m(\vec{R})\rangle \cdot \frac{dR_2}{dt} \cdots + \frac{\partial}{\partial R_N}|\psi_m(\vec{R})\rangle \cdot \frac{dR_N}{dt}$$

$$= \nabla_{\vec{R}}|\psi_m(\vec{R})\rangle \cdot \frac{d\vec{R}}{dt}$$

The phase β_G can be calculated as

$$\beta_G = i\int_{\vec{R}(t_0)}^{\vec{R}(t)} \langle\psi_m(\vec{R})|\nabla_{\vec{R}}|\psi_m(\vec{R})\rangle \cdot d\vec{R} \qquad (A.36)$$

This expression of the phase β_G implies that β_G does not depend on details of time dependence of parameter $\vec{R}(t)$, but depends on the geometric path which $\vec{R}(t)$ traces out in the parameter space. Because of this reason, the phase β_G is referred to as geometric phase. For the special case when $\vec{R}(t)$ traces a closed loop in the parameter space, $\vec{R}(t) = \vec{R}(t_0)$,

$$\beta_G = i\oint_C \langle\psi_m(\vec{R})|\nabla_{\vec{R}}|\psi_m(\vec{R})\rangle \cdot d\vec{R} \qquad (3.24, A.37)$$

This is the expression Berry uses in his original publication in 1984 [82].

Consider a special case of a spin-$\frac{1}{2}$ system under a time-dependent magnetic field. The Hamiltonian of the system is

$$H(t) = -\vec{\mu} \cdot \vec{B}(t)$$

The time-dependent magnetic field varies slowly in time in such a way that the magnitude and polar angle stay fixed, while the azimuthal angle increases linearly in time.

$$\vec{B}(t) = B\sin\theta\cos\varphi\,\vec{e}_x + B\sin\theta\sin\varphi\,\vec{e}_y + B\cos\theta\,\vec{e}_z$$

where $\varphi = \varphi(t) = \alpha t$. The Hamiltonian can be written as the matrix form

$$H(t) = \frac{\hbar\omega_L}{2}\begin{pmatrix} \cos\theta & e^{-i\varphi}\sin\theta \\ e^{i\varphi}\sin\theta & -\cos\theta \end{pmatrix}$$

where ω_L is the Larmor frequency of the spin-$\frac{1}{2}$ system. As the magnitude of the magnetic field is fixed, ω_L is a constant. The instantaneous eigenvalues are constants as well,

$$E_{\pm} = \pm\frac{\hbar\omega_L}{2}$$

and the corresponding eigenstates for the instantaneous Hamiltonian are

$$|\psi_{+,t}\rangle = |\psi_+(\varphi)\rangle = \begin{pmatrix} \cos\frac{\theta}{2} \\ e^{i\varphi}\sin\frac{\theta}{2} \end{pmatrix}$$

$$|\psi_{-,t}\rangle = |\psi_{-}(\varphi)\rangle = \begin{pmatrix} \sin\frac{\theta}{2} \\ -e^{i\varphi}\cos\frac{\theta}{2} \end{pmatrix}$$

The $|\psi_{+,t}\rangle$ eigenstate is the state when the spin oriented in the opposite direction of the magnetic field and $|\psi_{-,t}\rangle$ is the state when the spin aligned with the magnetic field. To calculate the geometric phase in the parameter space, we define

$$\vec{V}_{+}(\vec{B}) = i\langle\psi_{+}(\varphi)|\nabla_{\vec{B}}|\psi_{+}(\varphi)\rangle = -\frac{\sin^2\frac{\theta}{2}}{B\sin\theta}\vec{e}_{\varphi}$$

Plug in the expression of geometric phase, and use the Stokes Theorem, the geometric phase can be calculated as

$$\beta_G = \oint_C \vec{V}_{+}(\vec{B})\cdot d\vec{B} = \int_S \nabla_{\vec{B}}\times\vec{V}_{+}(\vec{B})d\vec{S} = -\frac{1}{2}\Omega_C$$

where the Ω_C is the solid angle of the contour in the parameter space. Similarly, for the situation when the spin aligned with the magnetic field,

$$\beta_G = +\frac{1}{2}\Omega_C$$

A.8 GOODNESS OF SPECTRUM FIT USING EASYSPIN SIMULATION

In section 5.4.3, EasySpin simulation with fit parameters B and θ are compared with our observed resonances. To get confidence intervals for B and θ, we use the χ^2 parameter, which is the sum of variance-weighted squared distance between each observed resonance and its closest peak in simulation,

$$\chi^2(B,\theta) = \sum_{i=1}^{3}\frac{\left[f_i - f_{i,sim}(B,\theta)\right]^2}{\sigma_i^2} \qquad (A.38)$$

where our observed resonance frequencies f_1, f_2 and f_3 are $486.5\,\text{MHz}$, $810.7\,\text{MHz}$ and $1104.6\,\text{MHz}$, respectively. We use our observed linewidth, $2\,\text{MHz}$, $3\,\text{MHz}$ and $3\,\text{MHz}$, respectively, as the standard deviation of each resonance frequencies σ_1, σ_2 and σ_3.

Since the $f_{i,sim}(B,\theta)$ does not have analytical expression, we cannot use the maximum likelihood estimation method as it needs the derivative of the χ^2 function. The contour plot of the change in χ^2 values for different parameter (B,θ) is shown in Figure A.4. The confidence intervals of B and θ are defined, according to $\Delta\chi^2 = 1$ where the green region in Figure A.4, as ± 0.5 G and ± 0.7 ° for the first minimum, and ± 0.5 G and ± 0.25 ° for the second minimum, respectively.

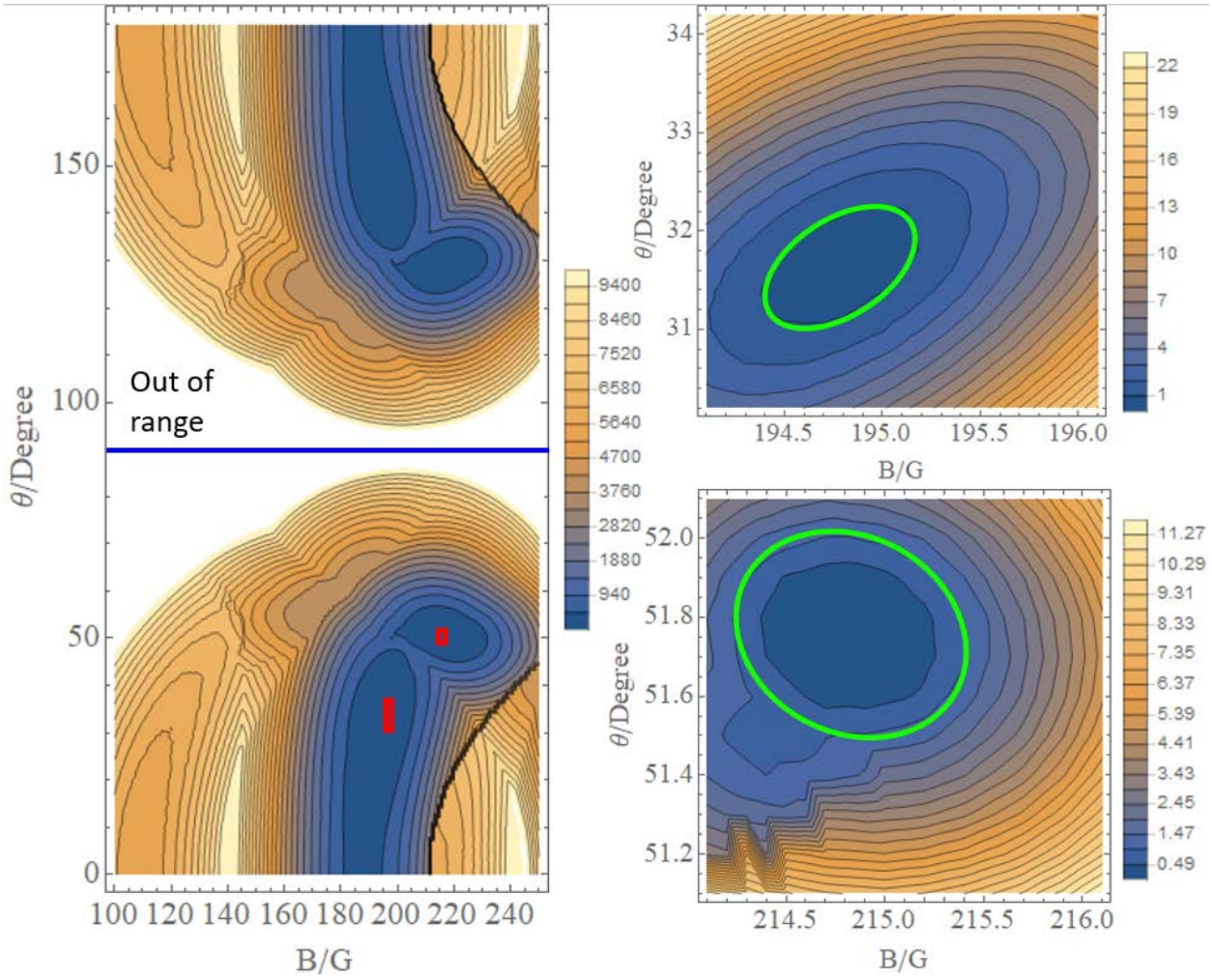

Figure A.4 The change in χ^2 values at different (B,θ). There are two local minima of χ^2 showing reasonably good fits. The regions in the red rectangles are zoomed in and shown at the right. The regions in the green loops are defined as the confidence regions of our parameters.

A.9 COMPUTATION CODES

A.9.1 Fitting Both x and y Spin Vector in chapter 3 (Mathematica)

```
SolidAngle := 2 * Pi * (1 - Δ / Sqrt[Δ^2 + Ω^2]);
NDephasing := 1 / (Sqrt[2] * Pi * SolidAngleError);
FitBerryNXFunc := bkg + ((amp * Cos[n * SolidAngle]) + 0) * Exp[- (n / NDephasing) ^2];
FitBerryNYFunc := bkg + ((amp * Cos[n * SolidAngle + Pi / 2]) + 0) * Exp[- (n / NDephasing) ^2]; D
allProbabilityMean = Join[Table[Join[{0}, NScanD20X[[i]]], {i, Length[NScanD20X]}],
   Table[Join[{1}, NScanD20Y[[j]]], {j, Length[NScanD20Y]}]];
allProbabilityStdDev = Join[NScanD20XErr, NScanD20YErr];
FitAllBerryNScanFunc[channel_, A_] :=
 KroneckerDelta[channel] * FitBerryNXFunc + KroneckerDelta[channel - 1] * FitBerryNYFunc;
(*channel 0: x. channel 1: y*)
fitAllModel = NonlinearModelFit[allProbabilityMean, FitAllBerryNScanFunc[channel, A],
  {{bkg, 0.5}, {amp, 0.5}, {Ω, c}, {SolidAngleError, 0.01}}, {channel, n},
  Weights → 1 / allProbabilityStdDev^2];
fitAllModelPlot = Plot[{fitAllModel[0, x], fitAllModel[1, x]}, {x, 0, 20},
   PlotStyle → {{Red, Thick}, {Red, Thick}}];
fitAllModel["ParameterConfidenceIntervalTable"]
```

A.9.2 Probability Integral of DEER Rabi in chapter 5 (Mathematica)

```
intMod[delta_, omega_, t_, prefac_] := Module[{ϕs, zs, S, axis, rotate, ϑ, φ, sig, Δ, Ω, const, avgSig},
  const = prefac;
  Ω = omega;
  Δ = delta;
  ϑ = 2 Pi Sqrt[Ω^2 + Δ^2] t;
  S := {Sqrt[1 - zs^2] * Cos[ϕs], Sqrt[1 - zs^2] * Sin[ϕs], zs};
  axis = Normalize[{Ω , 0, Δ}];
  rotate = RotationMatrix[ϑ, axis];
  φ = const * ((rotate.S - S).{0, 0, 1});
  sig = Cos[φ];
  avgSig = NIntegrate[sig, {ϕs, 0, 2 Pi}, {zs, -1, 1}] / 4 / Pi;
  avgSig
 ]

f[t_] := intMod[0, 5, t, 10];
ListPlot[Table[{t, f[t]}, {t, 0, 0.2, 0.005}], PlotRange → All]
```

A.9.3 EasySpin Solid-State Spectrum Simulation in chapter 5 (Matlab)

```
% basic frequency-swept EPR spectrum
Save file to synchronize breakpoints.==========================================================
clear, clf

% set up spin system
SysCu.g = [2.0835 2.415];
SysCu.Nucs = 'Cu';
SysCu.A = [30 339]; % for 63Cu (most abundant isotope), MHz

% For frequency sweeps, the convolutional width should be given in MHz.
SysCu.lwpp = 2; % MHz

% Frequency-sweep experiment
%-------------------------------------------------------------
Exp1.Field = 19.5;         % static magnetic field, mT
Exp1.mwRange = [0 1.2];  % frequency range, GHz

Exp1.CrystalSymmetry = 164;        % space group #164
Exp1.MolFrame = [0 0 0]*pi/180;       % molecular frame aligned with crystal frame
Exp1.CrystalOrientation = [0 32 0]*pi/180; % crystal frame tilted against lab frame

% Simulate and plot frequency-sweep spectrum
%pepper(SysCu,Exp1);
[x,S]=pepper(SysCu,Exp1);
data=[x(:) S(:)];
save('myfile.txt','data','-ascii');
```

APPENDIX B

SUPPLEMENTARY MATERIALS IN TECHNIQUES

B.1 ILLUMINATION LIGHT PULSING

As mentioned in section 2.3.2, in all pulsed ODMR experiments, we need pulsed illumination light. The measurement window for highest fluorescence contrast is within the first $300ns$ of illumination, which requires the rise time of our illumination light in nanoseconds.

We use 532 nm green laser as our illumination light source. Using a laser instead of a thermal light source provides us stability in illumination intensity, which is necessary in our pulsed experiments. The built-in TTL modulation of the laser is not fast enough for our experiments. The way we generate fast light pulses is by using acousto-optic modulator (AOM).

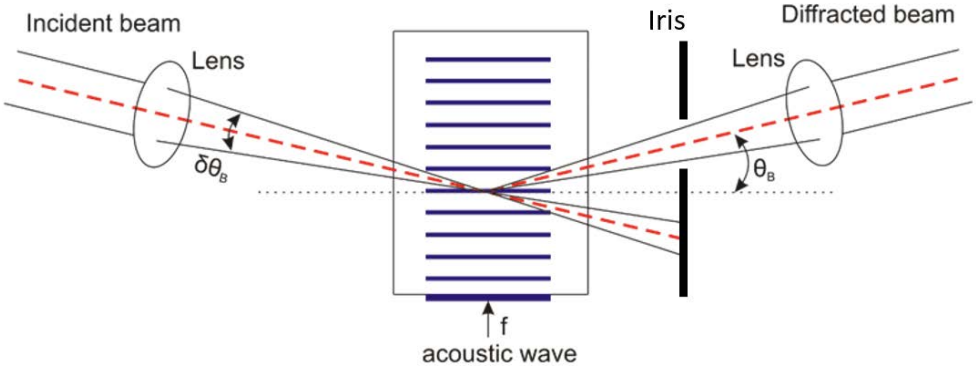

Figure B.1 Schematic drawing of acousto-optic modulator.

An AOM uses the acousto-optic effect to diffract the incident beam with sound waves. As shown in Figure B.1, as the acoustic wave passes through the crystal, the periodic change in refractive index of the crystal forms an optical grating and diffracts the incident beam. By

modulating the acoustic vibrator, the diffracted beam can be switched on and off in a short timescale. The sound speed in our acousto-optic material (tellurium dioxide, TeO_2) is 4×10^3 m/s. Our laser beam can be easily focused to a Gaussian spot with beam waist of $\sim$50 μm with a lens. The rise time of illumination pulse from our AOM is the time it takes for the acoustic wavefront passing the beam waist, which is $\sim$10 ns.

B.2 OPTIMIZING CONFOCAL MICROSCOPE

The confocal microscope is the used for isolation of single NV centers from the environment. The optimization of confocal microscope is the key step to improve the experiment efficiency. As mentioned in section 2.2.2, the key feature of a confocal microscope is to illuminate only a small volume which coincide with the photon collection volume by a focused illumination light. This requires our green illumination laser to be aligned perfectly with our collection path.

To achieve the optical alignment of our confocal microscope, we shoot a 670 nm red laser inversely through our collection path, as shown in Figure B.2. After the dichroic beam splitter, the green and red laser are combined into one beam. The irises are used for fine adjustment of this alignment of the two lasers. The sample objective is chosen to be apochromatic, which minimizes the color aberration of the focus point.

After the coarse alignment described above, it is usually sufficient to get a confocal image out of the microscope. Further adjustment tricks include back coupling of red laser and scattering image of green laser.

The back coupling of red laser is shown in Figure B.3. By placing a mirror at the focus of sample objective, the incident beam of red laser is reflected at the same path and coupled into the collection fiber. Once the back coupling is successful, a red laser spot will show up on the back coupling screen in the red laser box.

The scattering image from green laser is acquired by removing the 532 nm notch filter, connect the collection path to an SPCM (single photon counting module) and place a target sample (for instance, a resolution target) at the focus of sample objective. If we can get a reasonably clear scattering image from our confocal microscope, only tiny amount of color aberration adjustment is needed in the collection path to optimize the fluorescence image of NV centers.

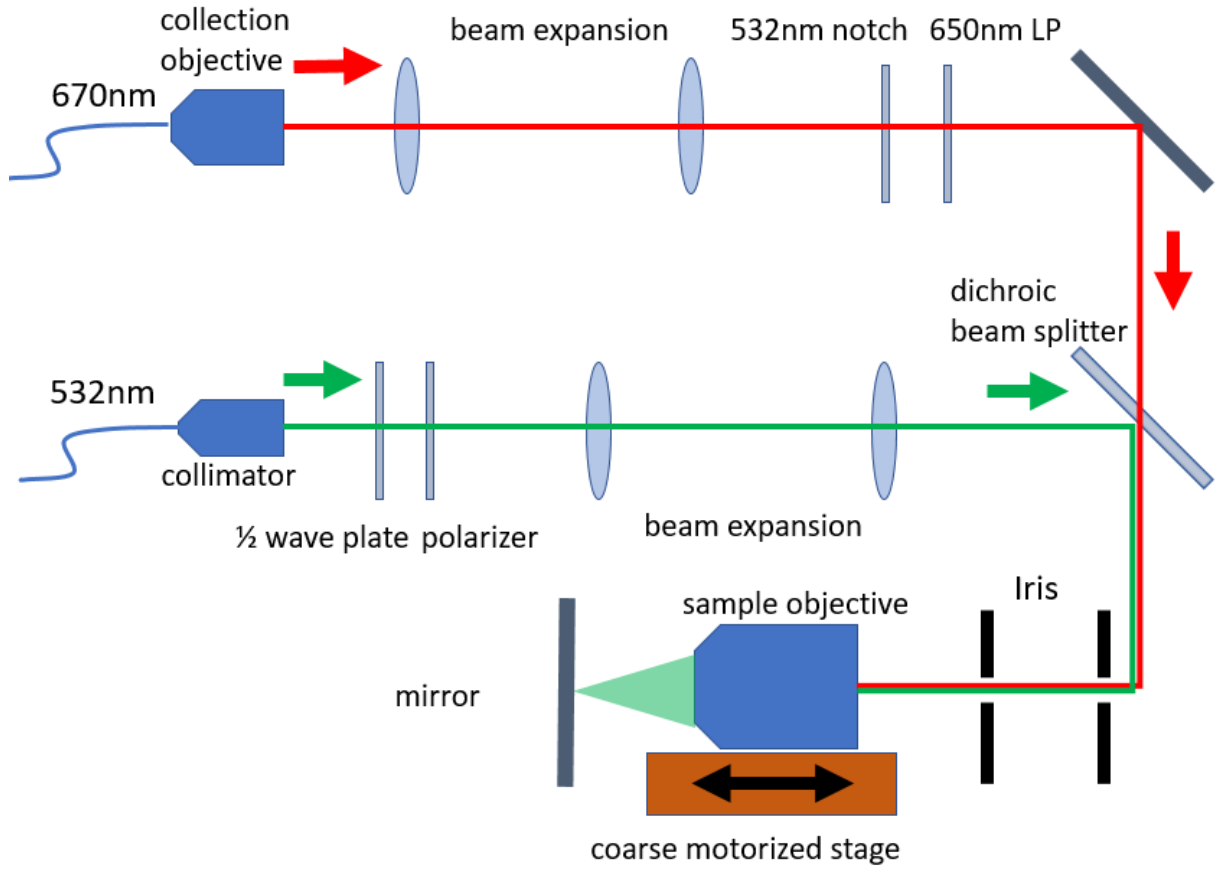

Figure B.2 Schematic drawing of confocal microscope alignment.

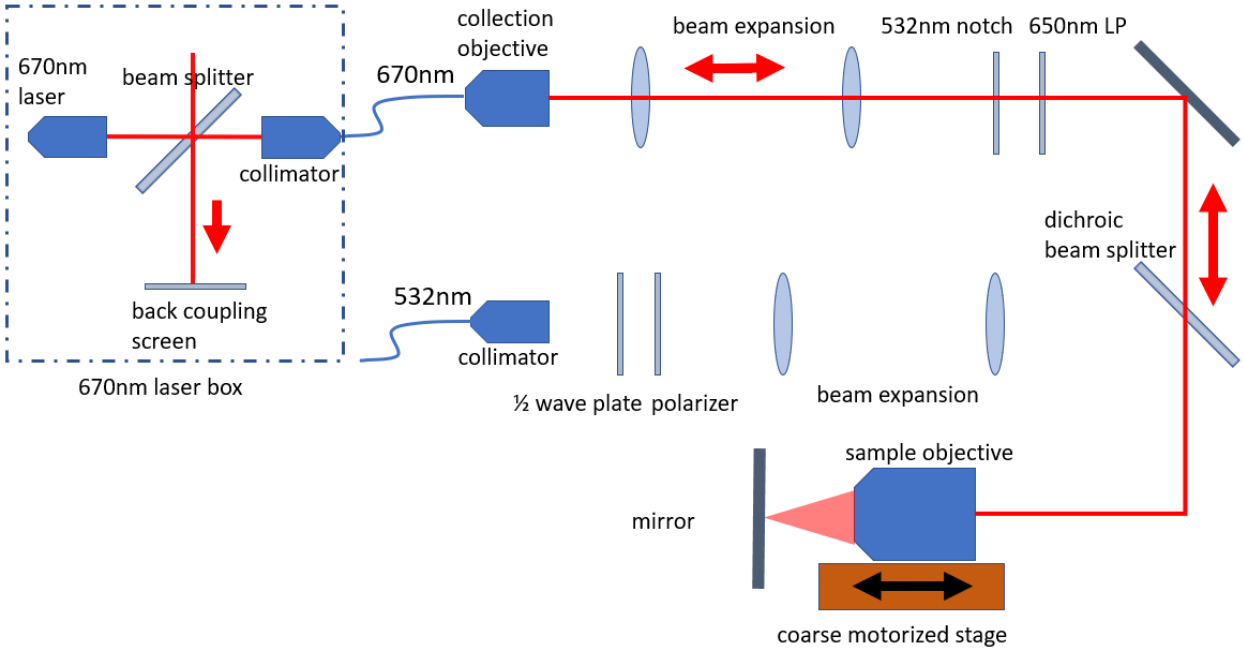

Figure B.3 Schematic drawing of back coupling technique for confocal alignment.

B.3 OPTICALLY INDUCED NUCLEAR SPIN POLARIZATION

As mentioned in section 2.4.3, the 2.2 MHz hyperfine splitting of NV centers will cause complex beating behavior in Ramsey experiment. In fact, the hyperfine splitting of NV centers will influence all of our coherent manipulations of NV if the microwave driving power is not sufficient and the Rabi frequency is not much larger than 2.2 MHz. However, the hyperfine splitting can be eliminated by polarizing the nuclear spin of nitrogen atom.

The excited state of the NV center, ^3E state, has a zero-field splitting $D_e = 1.42$ GHz between the $|m_s = 0\rangle$ and $|m_s = \pm 1\rangle$ spin states, similar to the ground state of NV center. When the external magnetic field along the $\mathrm{N-V}$ axis is close to 5×10^2 G, the $|m_s = 0\rangle$ and $|m_s = -1\rangle$ spin states become close to degenerate. Under the influence of non-axial components of hyperfine interaction $\frac{1}{2} A_\perp (\hat{S}_+ \hat{I}_- + \hat{S}_- \hat{I}_+)$ and the optical initialization of NV center, the nuclear spin of nitrogen atom is polarized. This is called dynamic nuclear polarization [128].

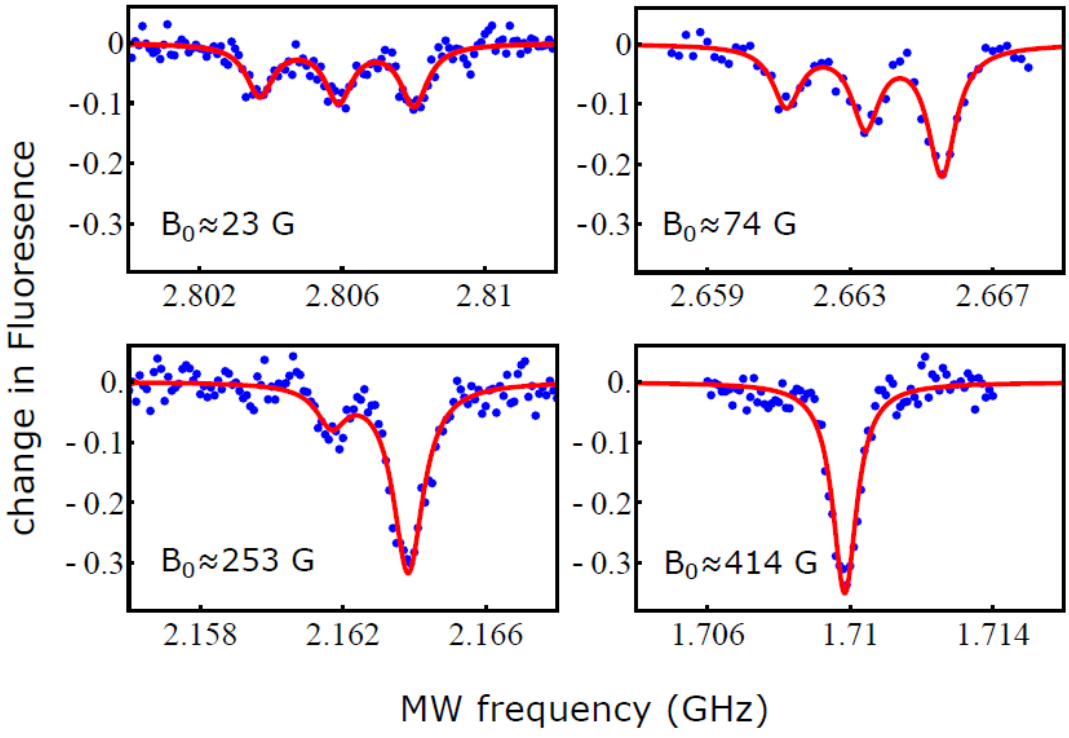

Figure B.4 Reproduced with permission from [59]. Pulsed ODMR at different magnetic field demonstrating dynamic nuclear polarization of ^{14}N nuclear spin at high magnetic field.

As shown in Figure B.4, the hyperfine splitting of ^{14}N triplet become unequal as the bias magnetic field increases. When the bias field larger than 400 G, the ^{14}N nuclear spin is polarized and only one resonance is left.

B.4 PHOTON ANTI-BUNCHING

Photon anti-bunching, or second order correlation measurement of the fluorescence photons, is used for checking whether the fluorescent spot on our confocal image is a single photon emitter (single NV center).

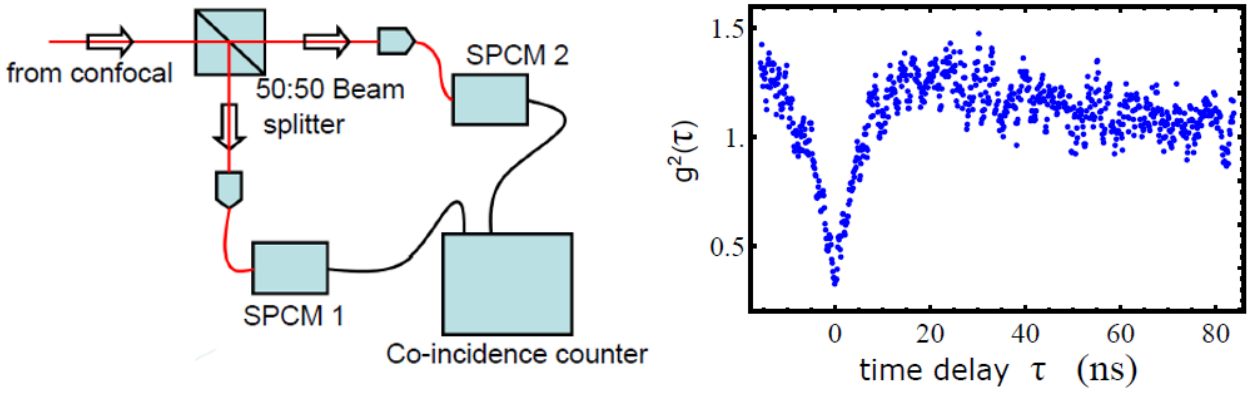

Figure B.5 Reproduced with permission from [59]. Photon anti-bunching observation setup and experimental data of a single NV center.

The principal of photon anti-bunching can be explained in a fairly easy way. As shown in Figure B.5, the fluorescence from a bright spot on our confocal image passes through a beam splitter. Two individual SPCMs (single photon counting module) are used to detect the fluorescence photons in each arm. If the fluorescence photons are from a single photon emitter, there will be only one photon at a time and thus the two SPCMs will never be triggered simultaneously. This corresponds to a dip of the correlation function from both SPCMs, as shown in Figure B.5 at right. A rigorous proof that the second order correlation drops as $g^2(0) = 1 - \frac{1}{n}$, where n is the number of photon emitters, can be found in quantum optics textbooks. Given that the $g^2(0) = 0.5$ for double NV centers, we validate all spots with $g^2(0) < 0.5$ as single NV centers.

B.5 ACID CLEANING OF DIAMOND SAMPLES

Acid cleaning of diamond samples are used to get rid of most of organic and inorganic contaminants on the diamond surface. It is necessary after nanoscale fabrications, annealing and ion implantation. It is also used to remove chemical residual on diamond surface in chapter 5.

During acid cleaning, the diamond sample is placed into a flask with round bottom. A 1:1:1 mixture of sulfuric acid, nitric acid and perchloric acid of ~20 mL is carefully poured into the flask and heated to boiling with a heating mantle. A condenser with flowing coolant water is connected to condense the acid vapor and prevent the vapor from getting out to our fume hood. The acid cleaning setup is shown in Figure B.6. I always keep the acid boiling for more than one hour before unplugging the heating mantle.

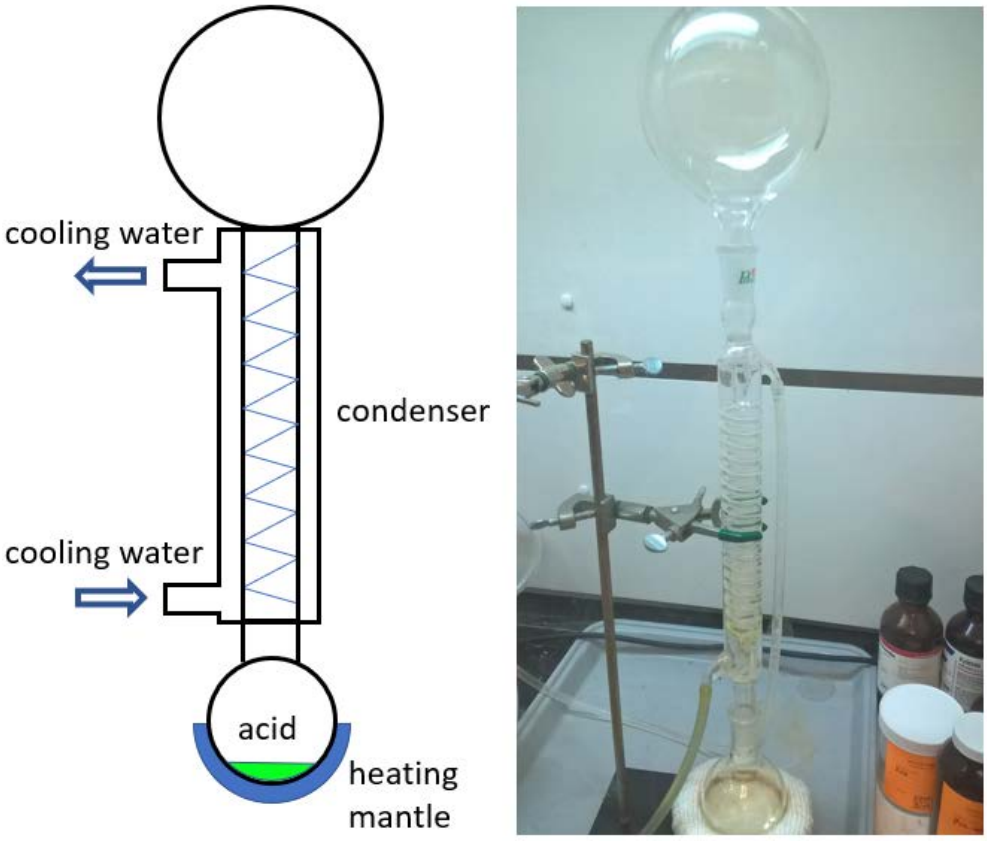

Figure B.6 Schematic drawing and photo of acid cleaning setup.

B.6 FABRICATION OF COPLANAR WAVEGUIDE

In chapter 5, the microwave driving field is delivered to the single NV center through a fabricated coplanar waveguide on a glass coverslip. The fabrication of coplanar waveguide is done in a lift-off process in photolithography.

The design of coplanar waveguide is shown in Figure B.7. The electromagnetic field is limited in the gaps between the central conductor and the ground plates. The waveguide is tapered to the working area with small gap width (~20 μm). The transmitted electromagnetic energy is then focused within the narrow gaps and provides large amplitude of transverse microwave driving field to drive the NV center. The total length of the tapered region is 3 mm, much less than the wavelength of our microwave (0.1 m~0.6 m for our frequency 0.5~3 GHz). Therefore, the exact impedance matching of tapering shape is not so important.

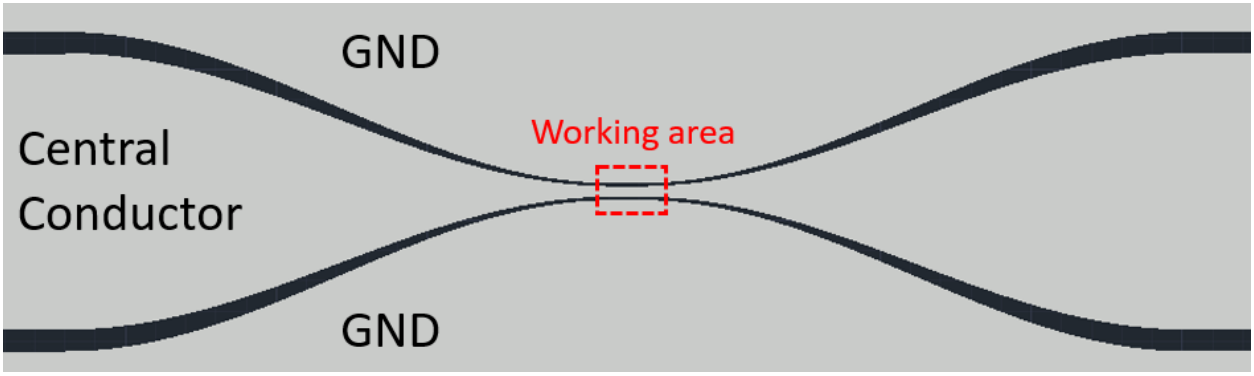

Figure B.7 Design of coplanar waveguide. The EM field is limited in the gaps between the central conductor and ground plates and has maximum peak value in the working area.

The coplanar waveguide is fabricated on a 22×22 mm^2 coverslip. Since the dimension of the coverslip is also much less than the wavelength of our microwave (0.1 m~0.6 m), the impedance matching of the non-tapered section of our coplanar waveguide is not important. However, to minimize the microwave power loss as much as we can, the non-tapered section of our coplanar waveguide is designed to have a characteristic impedance of 50 Ω. According to [129] where the original analytical expression dated back to [130], the characteristic impedance of a coplanar waveguide can be calculated as:

$$Z = \frac{30\pi}{\sqrt{\varepsilon_{eff}}} \cdot \frac{K'(k_1)}{K(k_1)}$$

$$\varepsilon_{eff} = 1 + \frac{\varepsilon_d - 1}{2} \cdot \frac{K(k_2)}{K'(k_2)} \cdot \frac{K'(k_1)}{K(k_1)}$$

where ε_d is the dielectric constant of the glass coverslip. $K(k)$ and $K'(k)$ are the complete elliptical integral of the first kind and its complement $K'(k) = K\left(\sqrt{1-k^2}\right)$. And k_1, k_2 and k_3 are defined as:

$$k_1 = \frac{w}{w + 2s}$$

$$k_2 = \frac{\sinh\left(\frac{\pi w}{4h}\right)}{\sinh\left(\frac{\pi(w+2s)}{4h}\right)}$$

where w is the width of the center conductor, s is the width of the gaps and h is the thickness of our coverslip. Online calculators programmed according to the above formula can also be used to calculate the characteristic impedance of the coplanar waveguide based on its geometry. With the thickness of glass coverslip fixed to $h = 0.17$ mm, and the width of center conductor large enough ($w = 3$ mm) so that the soldering is easy, the width of the gaps is designed to be 0.23 mm to maintain a characteristic impedance of $50\ \Omega$.

Numerical simulation of microwave transmission through the coplanar waveguide was done with Ansys Electronics Desktop, in order to understand the magnetic field distribution of the microwave. As shown in Figure B.8, the amplitude of the transverse magnetic field perpendicular to NV axis is amplified where the microwave is limited to the narrow gaps near the working area.

The lift-off process of photolithography is explained in Figure B.9. Positive photoresist AZ4210 is spin coated on our coverslip substrate and form a 3 μm layer of resist after prebake. Then the resist is exposed under 365 nm i-line ultraviolet light. During development, the exposed area of photoresist is dissolved in developer while the masked area remains attached. A 300 nm silver layer is deposited on top of the sample in a e-beam evaporator. And finally the unexposed photoresist is dissolved in remover and lifting off the metal layer on top.

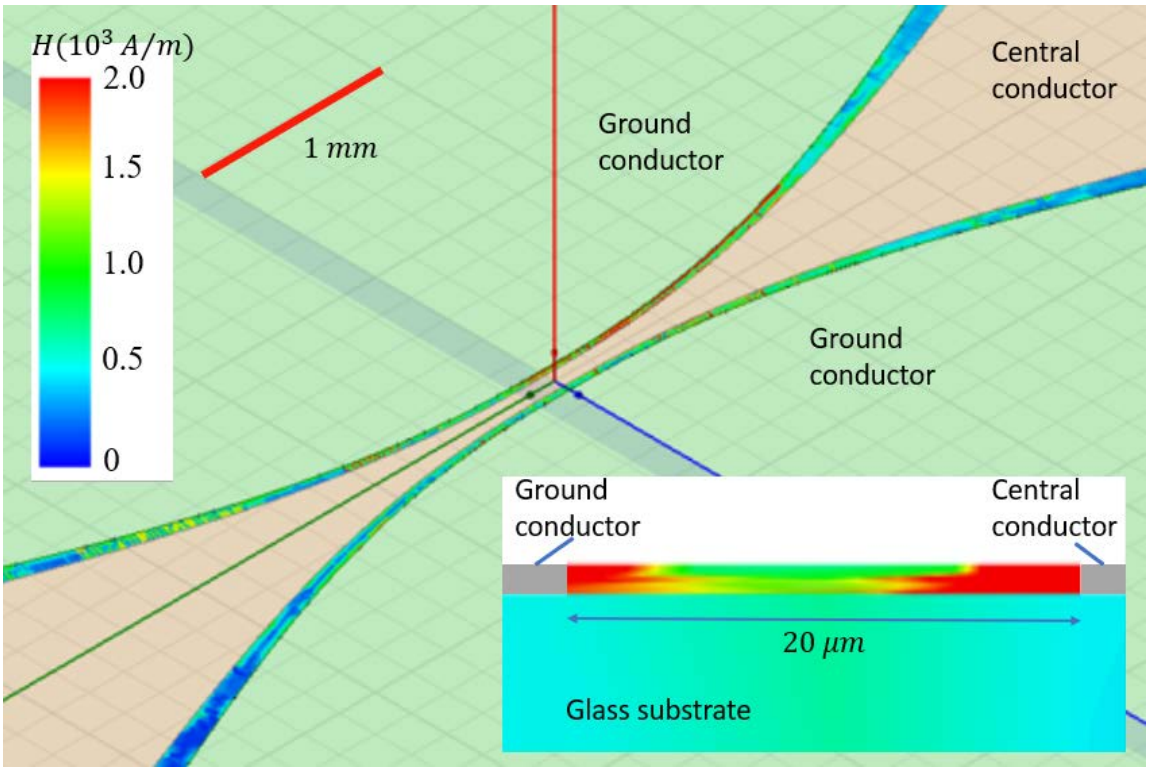

Figure B.8 Simulation of the distribution of transverse microwave field perpendicular to NV axis in the coplanar waveguide. The cross section of microwave field distribution within the gap in the working area is shown in the inset. The simulation is carried out using Ansys Electronics Desktop, with 1 W input microwave power and 2.87 GHz frequency. The NV axis in our diamond sample is assumed to be aligned with the (1,1,1) direction in the waveguide coordinate system. The number of mesh nodes in the gap at the working area is 10000.

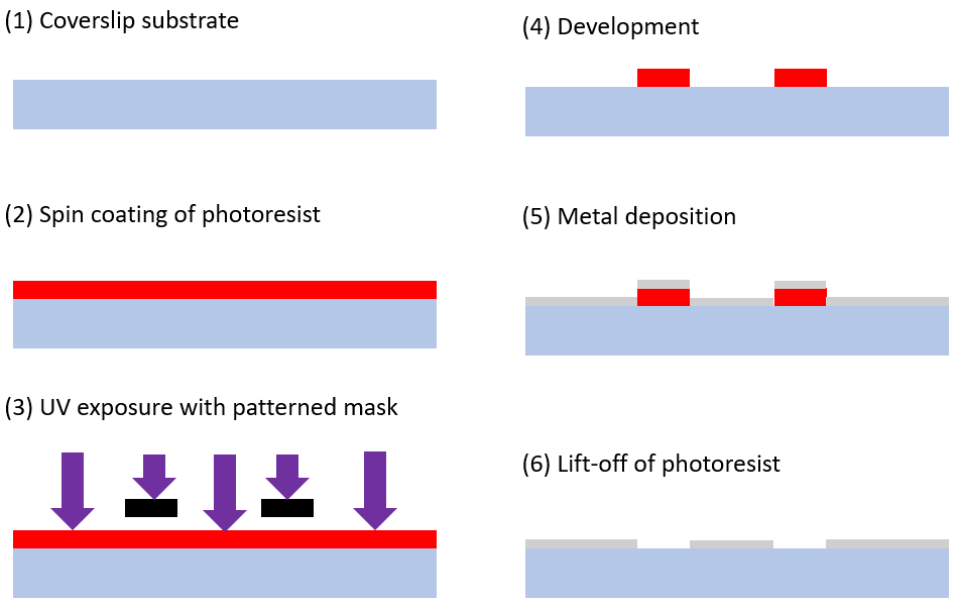

Figure B.9 Schematic drawing of lift-off process in photolithography.

APPENDIX C

SUPPLEMENTARY MATERIALS IN TEST EXPERIMENTS & CALIBRATION EXPERIMENTS

C.1 OUR RESULTS OF EXPERIMENTS IN CHAPTER 2

C.1.1 Continuous Wave ODMR

Figure C.1 shows our CW ODMR data without magnetic field. Our data is clearer and better in quality compared to the data shown in Figure 2.11, but we haven't taken CW ODMR data under many different small external magnetic fields. Figure C.2 shows the CW ODMR data with an external magnetic field of ~23 G. However, these two sets of data are taken at different single NV centers with different microwave driving power. Lacking of independent measurement of external magnetic field, the ~23 G value is estimated with the Zeeman splitting of our NV center.

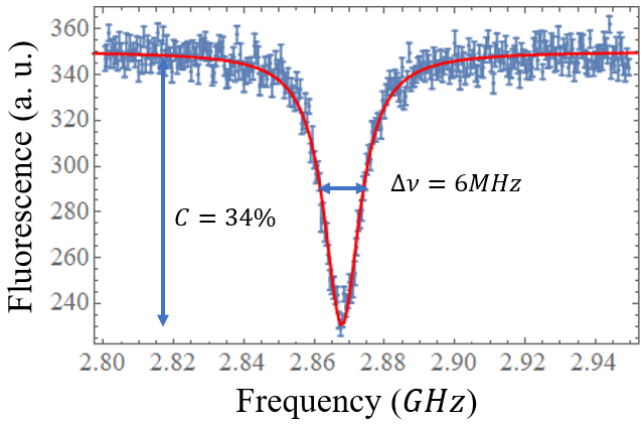

Figure C.1 CW ODMR without external magnetic field. Fluorescence photon counts are recorded as the microwave frequency is scanned. The data is fitted to a Lorentzian dip function (red curve).

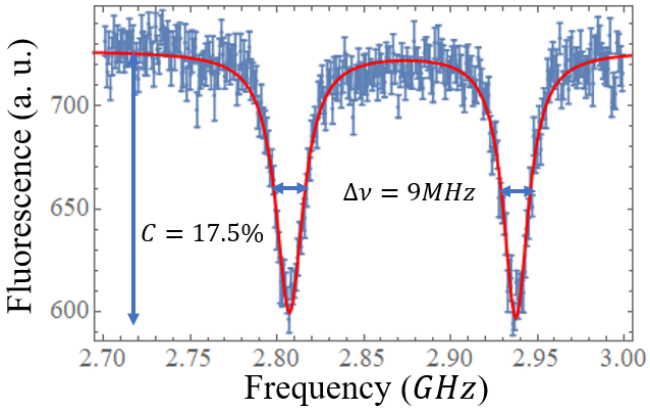

Figure C.2 CW ODMR with external axial magnetic field of ~23 G. Fluorescence photon counts are recorded as the microwave frequency is scanned. The data is fitted to a Lorentzian double-dips function (red curve).

C.1.2 Rabi Oscillation

The Rabi oscillation observed using the experimental setup in chapter 5 is shown in Figure C.3. The fluorescence in arbitrary unit is defined as the ratio between the fluorescence counts from the signal measurement window and counts from the reference measurement window. Compared to Figure 2.14, the Rabi frequency of our microwave driving field is much larger. This is due to the improved microwave efficiency with fabricated coplanar waveguide.

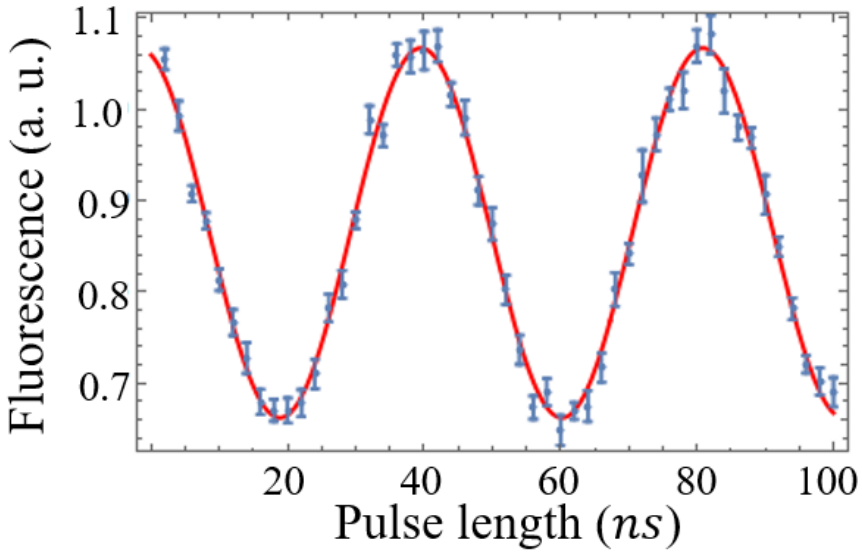

Figure C.3 Rabi oscillation with Rabi frequency of 25 MHz. The experimental sequence of Rabi oscillation is explained in section 2.4.2. The data is fitted to a sinusoidal function (red curve).

C.1.3 Spin Echo Experiment

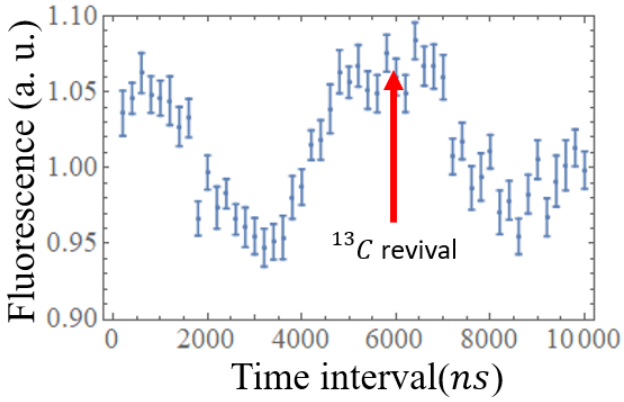

Figure C.4 Spin echo experiment on $NV2$ in chapter 5. Unlike the spin echo experiment introduced in section 2.4.4, the measured fluorescence is not mapped to probability in $|0\rangle$ state but shown directly on the y axis, as a convention in DEER research. The first ^{13}C revival shows up at time interval of 6 μs.

Figure C.4 shows the spin echo data on $NV2$ in chapter 5. We didn't take data at longer time intervals to see the decay of signal. The first ^{13}C revival can be seen at 6 μs.

C.2 CALIBRATION OF FLUORESCENCE LEVELS

In many experiments mentioned in chapter 3, the spin state of NV center qubit is inferred by the measurement of fluorescence photon counts. Therefore, the fluorescence level standards of state $|0\rangle$ and $|1\rangle$ need to be calibrated before we talk about the measured spin state of NV center. The typical calibration of fluorescence standards is via Rabi oscillation. For example, as shown in Figure C.3, the fit function (red curve) shows that the fluorescence is oscillating between 0.66 and 1.07, thus the fluorescence standards for $|0\rangle$ and $|1\rangle$ would be defined as 0.66 and 1.07 respectively. Note that even for the same single NV center, the fluorescence standards for $|0\rangle$ and $|1\rangle$ could change slightly over time due to imperfections in our experimental setup. The fluorescence level standards are calibrated everyday with Rabi oscillation.

Adiabatic passage is another way of calibrating fluorescence levels, and is used to check our Rabi oscillation calibration. By modulating both the amplitude and frequency of the

microwave driving field, an effective magnetic field adiabatically varying from $+z$ direction to $-z$ direction is created, as shown in Figure C.5 left. The detuned microwave driving field starts ramping up at $t = t_0$ while modulating its frequency, and then ramps back down to 0 with an opposite detuning at $t = t_f$. The magnitude of the effective magnetic field is 12.5 MHz.

From the data shown in Figure C.5 right, the fitted function (red curve) at $t < t_0$ and $t > t_f$ gives the fluorescence standards for $|0\rangle$ and $|1\rangle$ respectively. They all fall in the confidence interval (shown in Figure C.5 right) from our Rabi oscillation calibration, meaning our fluorescence level calibration is accurate.

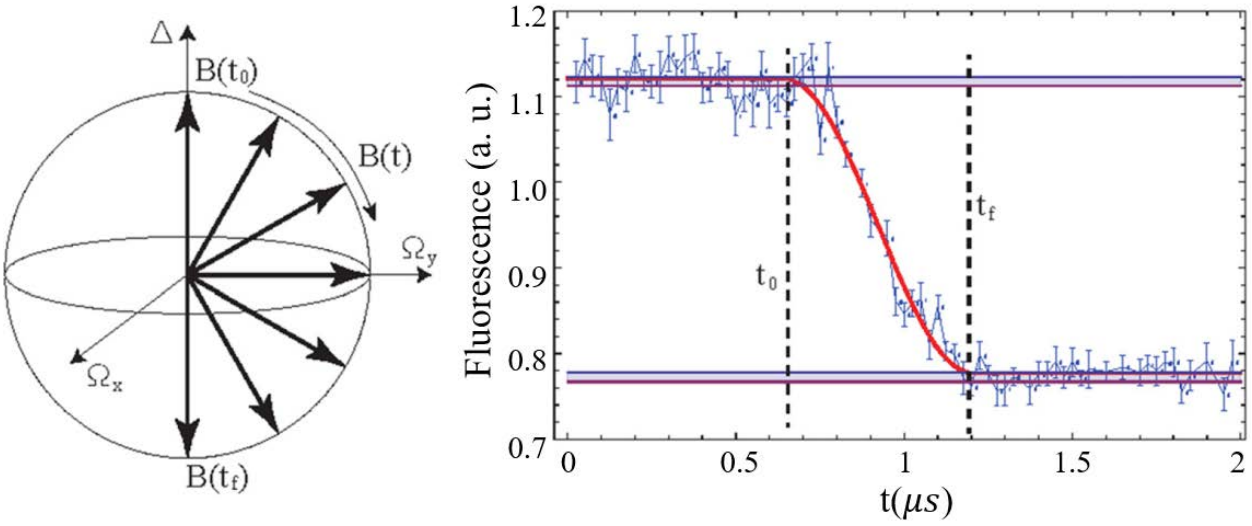

Figure C.5 Calibration of fluorescence levels with adiabatic passage. Using phase modulation of our microwave drive field with an IQ modulator, the effective magnetic field adiabatically varies from $\vec{B}(t_0)$ to $\vec{B}(t_f)$, shown on the left. The fluorescence level at different time is recorded and shown on the right. The fitted values of fluorescence levels for $|0\rangle$ and $|1\rangle$ states fall into the confidence interval of fitted values from our Rabi oscillation.

C.3 CALIBRATION OF PHASE DIFFERENCE IN XY PULSES

As mentioned in chapter 3, the state tomography is accomplished by applying the last $\frac{\pi}{2}$ pulse in either x or y direction. The 90° phase shift of microwave driving field is achieved by phase modulation with another IQ modulator. The IQ modulator provides us fine adjustment on the phase shift compared to a nonadjustable phase shifter.

To calibrate the 90° phase shift, I came up with the test sequence as shown in Figure C.6. Following a $\frac{\pi}{2}$ pulse in x channel, a pulse in y channel with scanned pulse length is applied to the NV center. If the first $\frac{\pi}{2}$ pulse is perfect and the second pulse is perfectly 90 ° phase shifted, the NV center is rotated to the $-y$ axis and the second pulse would not change the spin state. This is also called spin locking in NMR (nuclear magnetic resonance) techniques. Nevertheless, oscillation would be observed if the first $\frac{\pi}{2}$ pulse is not perfectly $\frac{\pi}{2}$ and/or the phase difference between the two pulses is not 90 °. The error is the pulse length of first $\frac{\pi}{2}$ pulse would result in a cosine function, and the phase error would result in a sine function, as shown in Figure C.7 left. By adjusting the phase in y channel with IQ modulator, the phase error is minimized when the fit function becomes close to a cosine function, as shown in Figure C.7 right, when the dominant error is from the pulse length of first $\frac{\pi}{2}$ pulse.

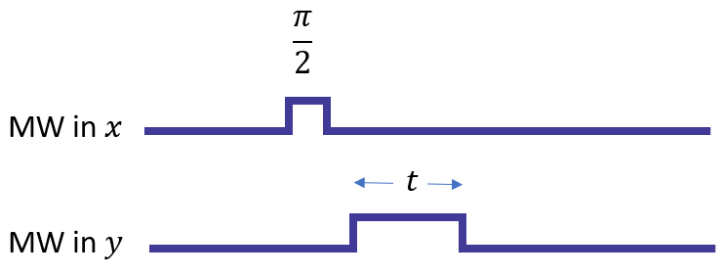

Figure C.6 Schematic drawing of experimental sequence for calibration of 90 ° phase shift.

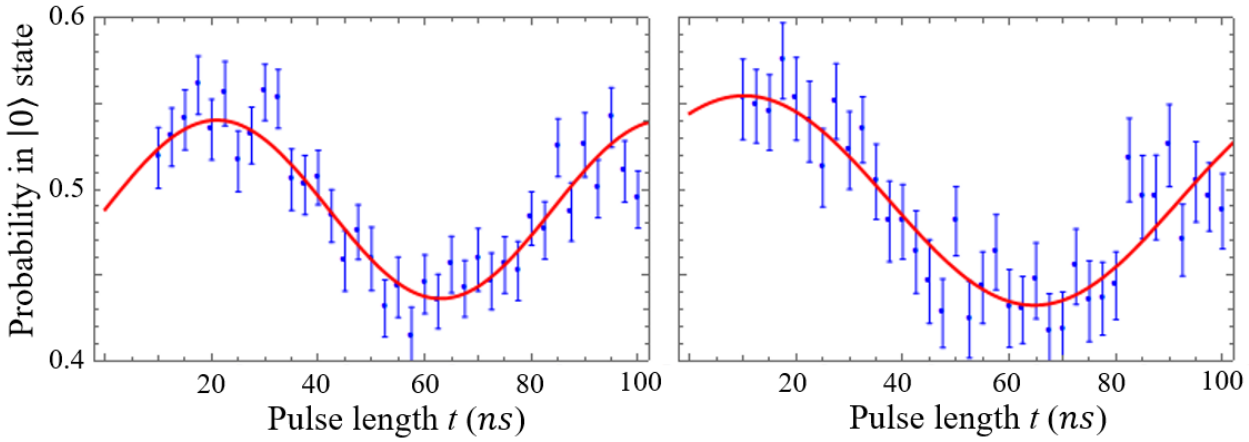

Figure C.7 Experimental data of phase shift calibration. The experimental sequence is shown in Figure C.6. The data is fitted to a sinusoidal function whose initial phase is a fit parameter. As shown on the left, phase shift error leads to a sine function. And the pulse length error in first pulse leads to a cosine function as shown on the right.

C.4 BERRY PHASE AS FUNCTION OF MICROWAVE FREQUENCY

Figure C.8 shows the measured S_x and S_y as function of frequency detuning Δ when Rabi frequency is fixed to $\Omega = 12.5$ MHz. The dashed lines in Figure C.8 are theoretical calculations. For very small detuning values the condition on adiabaticity for adiabatic process is broken so the smallest detuning value in our experiment is chosen to be 5 MHz.

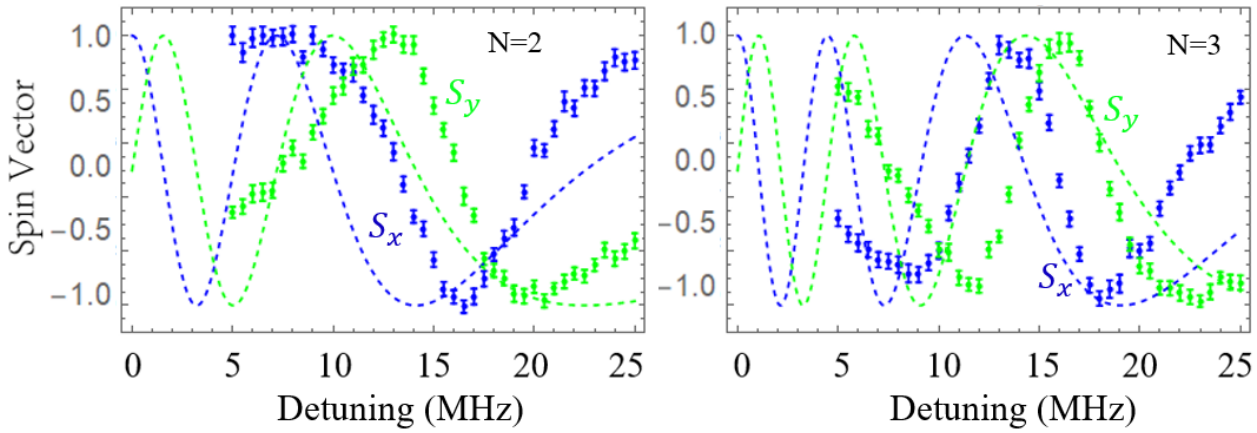

Figure C.8 Measured S_x and S_y as function of frequency detuning at $\Omega = 12.5$ MHz. See section 3.2.1 for experimental sequence. The dashed line is theoretical calculation for comparison.

The same as section 3.3.1, the measured phase is extracted from S_x and S_y values and plotted as functions of calculated solid angle for both $N = 2$ and $N = 3$. As shown in Figure C.9, the deviation of measured phase is frequency-dependent. At small (large solid angle) and large frequency detuning (small solid angle), the measured phase is smaller than expected. At median frequency detuning (about 7~14 MHz) the measured phase is larger.

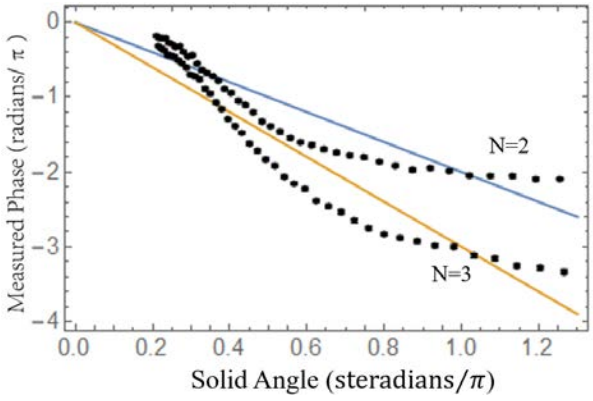

Figure C.9 Plot of the measured phase against the calculated solid angle based on varying detuning, for different values of N. Straight lines with slope -2, -3 are theoretical predictions as the net phase proportional to solid angle.

C.5 HYPERFINE SPLITTING AND COHERENCE TIME OF $NV1$, $NV2$

As mentioned in section 5.3, we observed DEER signal from two single NV centers, $NV1$ and $NV2$. The hyperfine splitting of each NV center is observed with pulsed ODMR spectrum and the coherence time is measured with spin echo experiment.

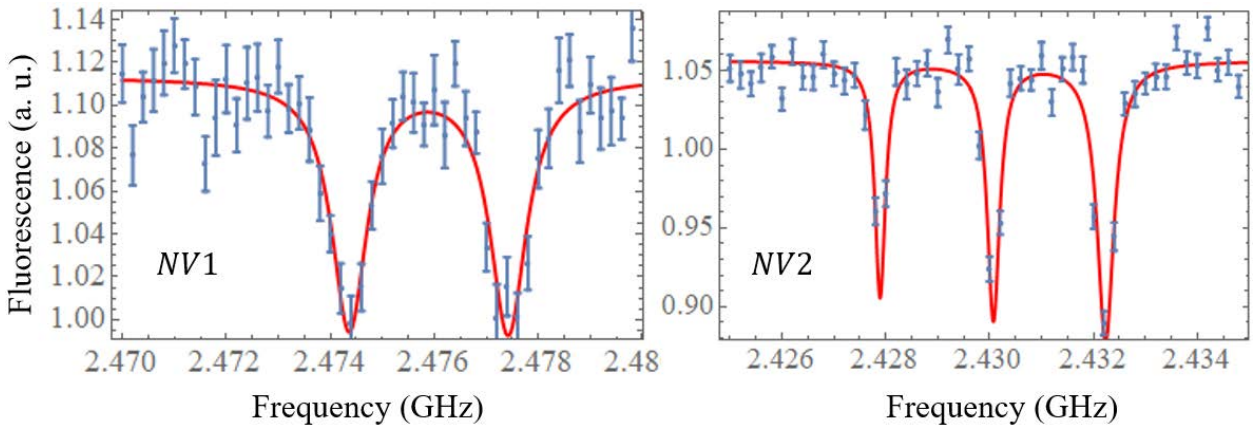

Figure C.10 Pulse ODMR spectrum from $NV1$ and $NV2$. The $NV2$ data is also shown in Figure 2.13 as example of pulsed ODMR.

Figure C.10 shows the pulsed ODMR of $NV1$ and $NV2$. For $NV1$, a doublet splitting is observed. This is due to the ^{15}N hyperfine splitting. The frequency spacing between the two resonances is 3.0 MHz, which confirms that it is the ^{15}N hyperfine splitting [18, 131-133]. On the other hand, $NV2$ shows a triplet splitting due to the typical ^{14}N hyperfine splitting with frequency spacing of 2.2 MHz.

Although the pulsed ODMR spectrums are taken with the same 2 μs π pulse, the spectrum of $NV1$ has a much larger linewidth (0.4 MHz) than $NV2$ (0.15 MHz). This is very likely due to a larger inhomogeneous broadening in $NV1$, inferring a noisy environment of $NV1$. Unlike $NV2$, the two resonances of $NV1$ have similar depth and show no evidence of optically induced nuclear spin polarization, as introduced in appendix B.3.

The spin echo experiment on $NV1$ is shown in Figure C.11. The ^{13}C revival decay implies the coherence time T_2 of $NV1$ is $\sim$10 μs.

Figure C.4 and Figure C.12 show spin echo experiments on $NV2$. Unlike the data shown in Figure C.11, the spin echo on $NV2$ shows reasonable contrast at ^{13}C revivals at 59 μs, implies a much larger T_2 of $NV2$. Our DEER measurement is using spin echo sequence at 6 μs, well within the coherence time.

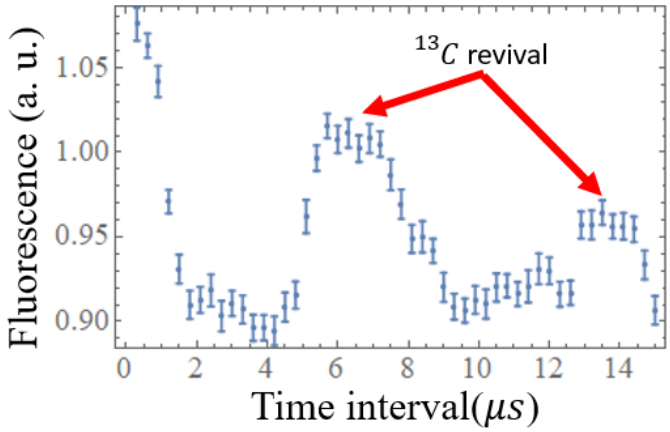

Figure C.11 Spin echo experiment on $NV1$. The ^{13}C revivals show significant decay ($1/e$ in revival heights) in ~13 μs. See section 2.4.4 for experimental sequence of spin echo.

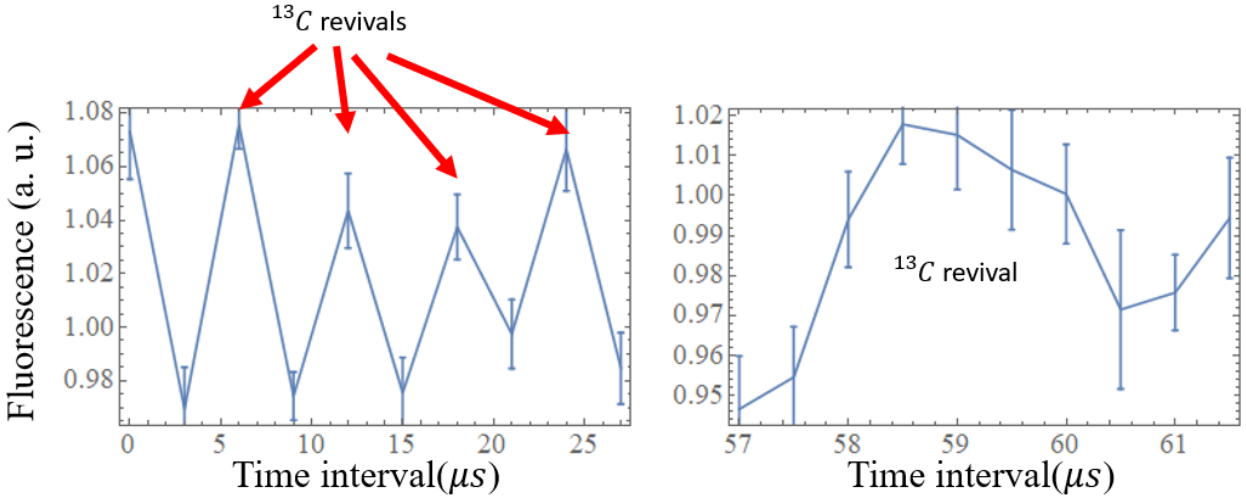

Figure C.12 Spin echo experiments on $NV2$. The 10th ^{13}C revival is zoomed in on the right. The relatively long coherence time (in regards of $NV1$) implies that the $NV2$ is likely a deep NV. See section 2.4.4 for experimental sequence of spin echo.

C.6 SINGLE PULSE DEER

As mentioned in section 5.3.1, using the DEER sequence in Figure 5.1 results in a large decrease in contrast of spin readout. Our DEER experiments use the sequence shown in Figure 5.11 instead. The comparison is shown in Figure C.13.

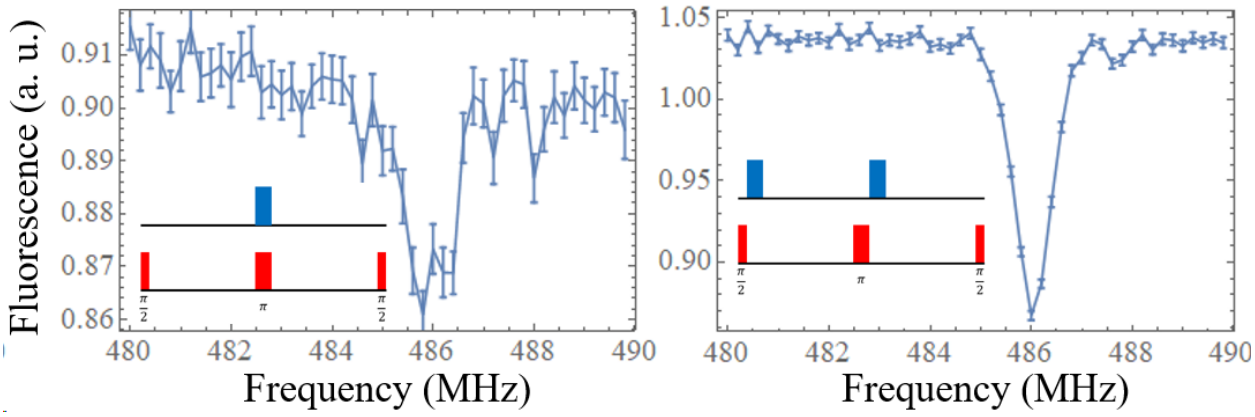

Figure C.13 Comparison between single pulse DEER (left, sequence shown in the inset and in Figure 5.1) and balanced DEER (right, sequence shown in the inset and in Figure 5.11). The readout contrast is much lower in single pulse DEER than in balanced DEER. Parameters of microwave drive field is the same as in Figure 5.13.

APPENDIX D

LIST OF EQUIPMENT

D.1 LIST OF EQUIPMENT IN EXPERIMENTAL SETUP IN CHAPTER 3

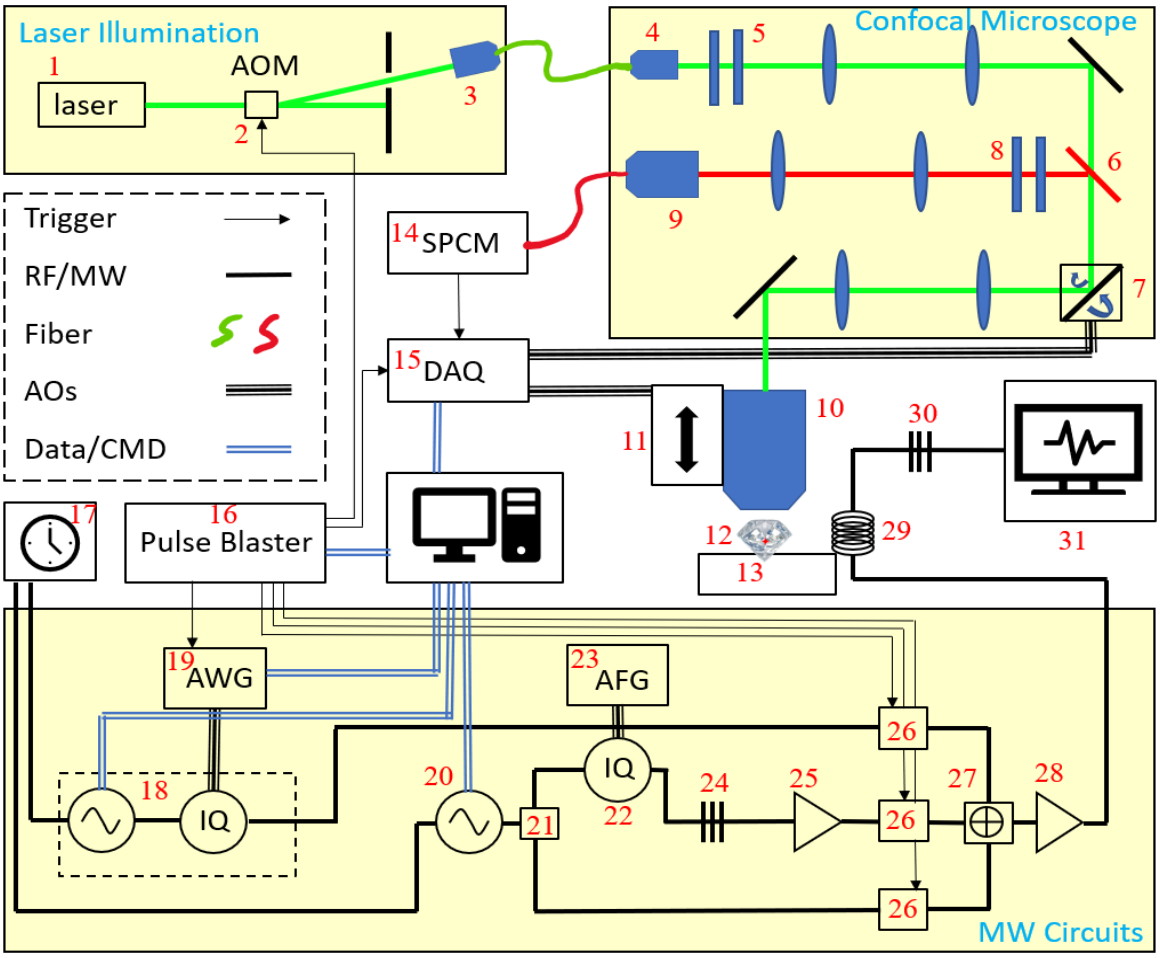

Figure D.1 Experimental apparatus in chapter 3.

Table D.1 List of instruments in chapter 3

#	Instruments	Notes
1	LASERGLOW LLS-0532-CFM	Nd:Yag doubled, 532 nm, IIIb
2	NEOS 15210 AOM	Driver Model 21210-1DM
3	THORLABS F240APC-A	fiber coupler, 0.51 NA
4	THORLABS F240APC-A	fiber coupler, 0.51 NA
5	Half wave plate + Linear polarizer	Fine control of excitation power
6	SEMROCK LPD01-532RS-25	RazorEdge Dichroic BS
7	CAMBRIDGE TECH. 6215H Optical Scanner	MicroMax 673 Driver Board
8	SEMROCK LPD01-532RS-25	StopLine Notch Filter
	THORLABS FELH0650	Premium Long Pass
	THORLABS FES0800	Short Pass
9	OLYMPUS Plan N Achromat 10X	0.25 NA, 10.6 mm WD
10	OLYMPUS MPLAPON 50X	0.95 NA, 0.35 mm WD
11	MADCITYLABS Nano-F100	Piezo, 100-micron range, open-loop
12	SUMITOMO single crystal diamond	Type IIa, <1 1 1> cut, double polished
13	Newport M-562-xyz	3-axes manual stage
14	PERKIN-ELMER SPCM-AQR-14-FC	Dark counts 53, pulse width 17 ns, dead time 30 ns
15	NI PCI-6229 DAQMx	Analogue outputs, counters etc.
	NI PCI-6601	Counter board
16	SPINCORE PulseBlaster ESR-Pro	400 MHz, 2.5 ns time resolution
17	SRS FS725 Rubedium Frequency Standard	5 MHz, 10 MHz reference clock
18	ROHDE&SCHWARZ SMIQ03B	Signal Generator with built-in IQ mode
19	Tektronix AWG520	Arbitrary Waveform Generator 1GS/s
20	PTS 3200	Signal Generator with Arduino control
21	MINICIRCUITS ZAPDJ-2-S	Power splitter 1-2GHz
22	Marki IQ 1545	IQ modulator
23	Tektronix AFG3102	Arbitrary Function Generator (DC output)

#	Instruments	Notes
24		Fixed attenuator
25		Amplifier
26	CMC CMCS0947A MW Switches	switching speed 3 ns
27	MINICIRCUITS ZN4PD1-50-S+	Power Combiner
28	OPHIR 58003084-28 MW Amp.	0.5-3 GHz, 50 W
29	GOODFELLOW CU005171 Cu wire	20-micron diameter, 99.99 % purity
30		Attenuator
31	AGILENT 8596E Spectrum Analyzer	9 kHz-12.8 GHz

D.2 LIST OF EQUIPMENT IN EXPERIMENTAL SETUP IN CHAPTER 5

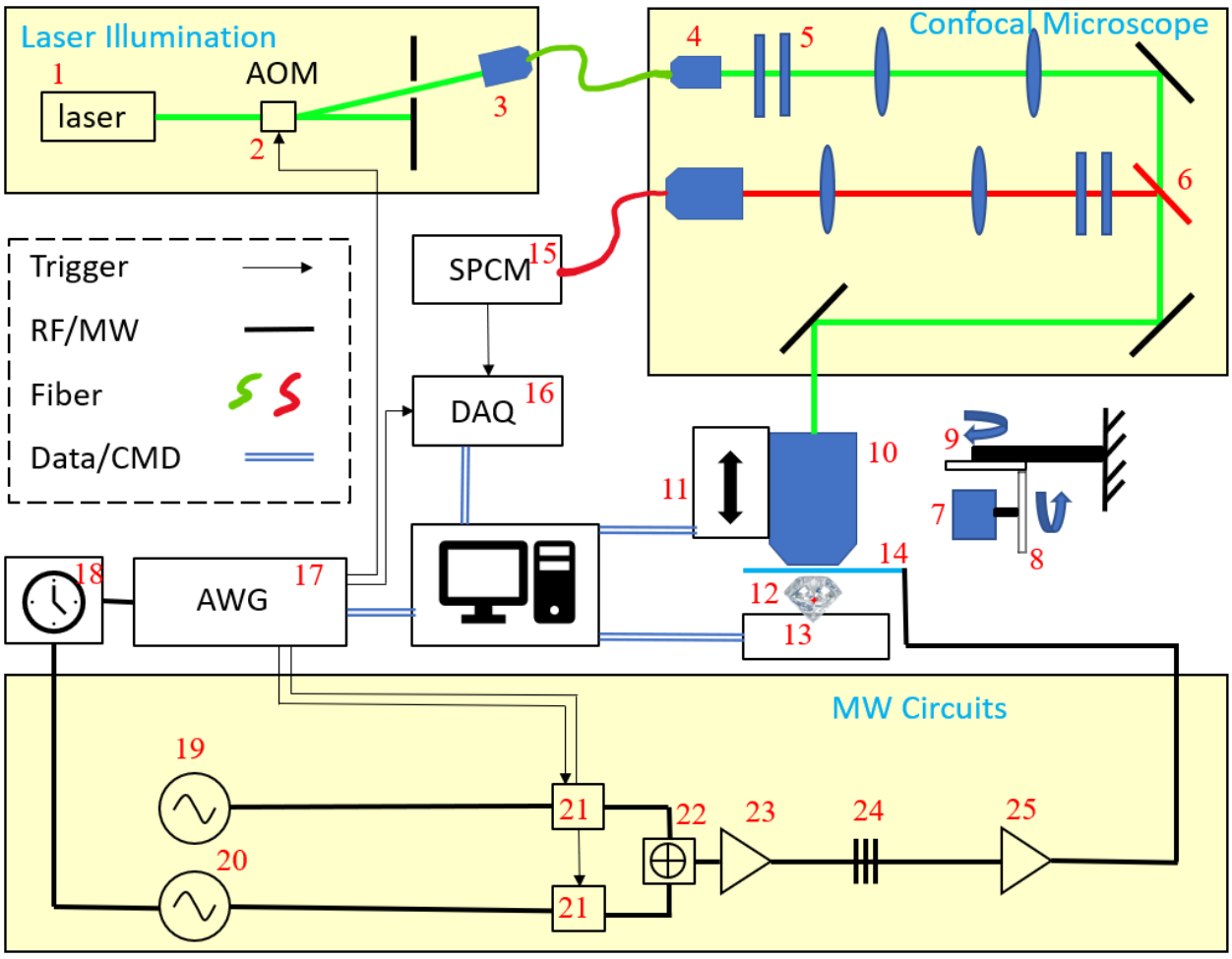

Figure D.2 Experimental apparatus in chapter 5.

Table D.2 List of instruments in chapter 5.

#	Instruments	Notes
1	LASERGLOW LLS-0532-CFM	Nd:Yag doubled, 532 nm, IIIb
2	Gooch&Housego 15210 AOM	Driver Model 21210-1DM
3	THORLABS FiberPort Coupler	0.2 NA
4	THORLABS F240APC-A	fiber coupler, 0.51 NA
5	Half wave plate + Linear polarizer	Fine control of excitation power
6	SEMROCK LPD01-532RS-25	RazorEdge Dichroic BS
7	K&J Magnet	Permanent magnet
8	THORLABS RSP1	Manual rotation mount
9	THORLABS RP01	Manual rotation stage
10	Olympus UPLFLN100XO2 objective	1.3 NA, 0.2 WD, coverslip corrected
11	THORLABS MTS25-Z8	Motorized stage
12	Element6 Electronic grade implanted	<1 0 0>cut, 200-micron slice
13	MadCityLabs Nano-LP100	3-axes nano stage, 100-micron range
14	Coplanar waveguide	Fabricated on coverslip
15	PicoQuant	Dark counts 23, pulse width 20 ns
16	ADwin-Gold II	Counter, event trigger input
17	Tektronix AWG 520	Arbitrary Waveform Generator
18	SRS FS725 Rubedium Frequency Standard	5 MHz, 10 MHz reference clock
19	WindFreakTech SynthUSBII	Synthesizer
20	PTS 3200	Signal Generator with Arduino control
21	MINICIRCUITS	Rise time 6ns
22	MINICIRCUITS	
23	WindFreakTech AmpNV	Adjustable broadband amplifier
24	MINICIRCUITS	Fixed attenuator
25	OPHIR 58003084-28 MW Amp.	0.5-3 GHz, 50 W

BIBLIOGRAPHY

1. Davies, G. and H.M. F., *Optical studies of the 1.945 eV vibronic band in diamond.* Proceedings of the Royal Society of London. A. Mathematical and Physical Sciences, 1976. **348**(1653): p. 285-298.
2. Gruber, A., et al., *Scanning Confocal Optical Microscopy and Magnetic Resonance on Single Defect Centers.* Science, 1997. **276**(5321): p. 2012-2014.
3. Dutt, M.V.G., et al., *Quantum Register Based on Individual Electronic and Nuclear Spin Qubits in Diamond.* Science, 2007. **316**(5829): p. 1312-1316.
4. Jelezko, F., et al., *Observation of Coherent Oscillation of a Single Nuclear Spin and Realization of a Two-Qubit Conditional Quantum Gate.* Physical Review Letters, 2004. **93**(13): p. 130501.
5. Cramer, J., et al., *Repeated quantum error correction on a continuously encoded qubit by real-time feedback.* Nature Communications, 2016. **7**: p. 11526.
6. Brouri, R., et al., *Photon antibunching in the fluorescence of individual color centers in diamond.* Optics Letters, 2000. **25**(17): p. 1294-1296.
7. Dräbenstedt, A., et al., *Low-temperature microscopy and spectroscopy on single defect centers in diamond.* Physical Review B, 1999. **60**(16): p. 11503-11508.
8. Kurtsiefer, C., et al., *Stable Solid-State Source of Single Photons.* Physical Review Letters, 2000. **85**(2): p. 290-293.
9. Santori, C., et al., *Nanophotonics for quantum optics using nitrogen-vacancy centers in diamond.* Nanotechnology, 2010. **21**(27): p. 274008.
10. Li, P.-B., et al., *Hybrid Quantum Device with Nitrogen-Vacancy Centers in Diamond Coupled to Carbon Nanotubes.* Physical Review Letters, 2016. **117**(1): p. 015502.
11. Ali Momenzadeh, S., et al., *Thin Circular Diamond Membrane with Embedded Nitrogen-Vacancy Centers for Hybrid Spin-Mechanical Quantum Systems.* Physical Review Applied, 2016. **6**(2): p. 024026.
12. Bernien, H., et al., *Heralded entanglement between solid-state qubits separated by three metres.* Nature, 2013. **497**: p. 86.
13. Hensen, B., et al., *Loophole-free Bell inequality violation using electron spins separated by 1.3 kilometres.* Nature, 2015. **526**: p. 682.
14. Kalb, N., et al., *Experimental creation of quantum Zeno subspaces by repeated multi-spin projections in diamond.* Nature Communications, 2016. **7**: p. 13111.
15. Balasubramanian, G., et al., *Nanoscale imaging magnetometry with diamond spins under ambient conditions.* Nature, 2008. **455**: p. 648.
16. Plakhotnik, T., *Diamonds for quantum nano sensing.* Current Opinion in Solid State & Materials Science, 2017. **21**(1): p. 25-34.

17. Rondin, L., et al., *Magnetometry with nitrogen-vacancy defects in diamond.* Reports on Progress in Physics, 2014. **77**(5): p. 056503.
18. Doherty, M.W., et al., *The nitrogen-vacancy colour centre in diamond.* Physics Reports-Review Section of Physics Letters, 2013. **528**(1): p. 1-45.
19. Balasubramanian, G., et al., *Ultralong spin coherence time in isotopically engineered diamond.* Nature Materials, 2009. **8**: p. 383.
20. Ph, T., et al., *Spin-flip and spin-conserving optical transitions of the nitrogen-vacancy centre in diamond.* New Journal of Physics, 2008. **10**(4): p. 045004.
21. Neumann, P., et al., *High-Precision Nanoscale Temperature Sensing Using Single Defects in Diamond.* Nano Letters, 2013. **13**(6): p. 2738-2742.
22. Toyli, D.M., et al., *Fluorescence thermometry enhanced by the quantum coherence of single spins in diamond.* Proceedings of the National Academy of Sciences, 2013. **110**(21): p. 8417-8421.
23. Kucsko, G., et al., *Nanometre-scale thermometry in a living cell.* Nature, 2013. **500**: p. 54.
24. Degen, C., *Microscopy with single spins.* Nature Nanotechnology, 2008. **3**: p. 643.
25. Wrachtrup, J. and A. Finkler, *Single spin magnetic resonance.* Journal of Magnetic Resonance, 2016. **269**: p. 225-236.
26. Freeman, M.R. and B.C. Choi, *Advances in Magnetic Microscopy.* Science, 2001. **294**(5546): p. 1484-1488.
27. de Lange, G., et al., *Single-Spin Magnetometry with Multipulse Sensing Sequences.* Physical Review Letters, 2011. **106**(8): p. 080802.
28. de Lange, G., et al., *Universal Dynamical Decoupling of a Single Solid-State Spin from a Spin Bath.* Science, 2010. **330**(6000): p. 60-63.
29. Taylor, J.M., et al., *High-sensitivity diamond magnetometer with nanoscale resolution.* Nature Physics, 2008. **4**: p. 810.
30. Ishikawa, T., et al., *Optical and Spin Coherence Properties of Nitrogen-Vacancy Centers Placed in a 100 nm Thick Isotopically Purified Diamond Layer.* Nano Letters, 2012. **12**(4): p. 2083-2087.
31. Babinec, T.M., et al., *A diamond nanowire single-photon source.* Nature Nanotechnology, 2010. **5**: p. 195.
32. Hadden, J.P., et al., *Strongly enhanced photon collection from diamond defect centers under microfabricated integrated solid immersion lenses.* Applied Physics Letters, 2010. **97**(24): p. 241901.
33. Hausmann, B.J.M., et al., *Integrated High-Quality Factor Optical Resonators in Diamond.* Nano Letters, 2013. **13**(5): p. 1898-1902.
34. Le Sage, D., et al., *Efficient photon detection from color centers in a diamond optical waveguide.* Physical Review B, 2012. **85**(12): p. 121202.
35. Siyushev, P., et al., *Monolithic diamond optics for single photon detection.* Applied Physics Letters, 2010. **97**(24): p. 241902.
36. Pham, L.M., et al., *Magnetic field imaging with nitrogen-vacancy ensembles.* New Journal of Physics, 2011. **13**(4): p. 045021.
37. Steinert, S., et al., *High sensitivity magnetic imaging using an array of spins in diamond.* Review of Scientific Instruments, 2010. **81**(4): p. 043705.
38. McGuinness, L.P., et al., *Quantum measurement and orientation tracking of fluorescent nanodiamonds inside living cells.* Nature Nanotechnology, 2011. **6**: p. 358.

39. Sheng, D., et al., *Subfemtotesla Scalar Atomic Magnetometry Using Multipass Cells.* Physical Review Letters, 2013. **110**(16): p. 160802.
40. Dang, H.B., A.C. Maloof, and M.V. Romalis, *Ultrahigh sensitivity magnetic field and magnetization measurements with an atomic magnetometer*. Applied Physics Letters, 2010. **97**(15): p. 151110.
41. Rondin, L., et al., *Nanoscale magnetic field mapping with a single spin scanning probe magnetometer.* Applied Physics Letters, 2012. **100**(15): p. 153118.
42. Grinolds, M.S., et al., *Quantum control of proximal spins using nanoscale magnetic resonance imaging.* Nature Physics, 2011. **7**: p. 687.
43. Maletinsky, P., et al., *A robust scanning diamond sensor for nanoscale imaging with single nitrogen-vacancy centres.* Nature Nanotechnology, 2012. **7**: p. 320.
44. Ciobanu, L., D.A. Seeber, and C.H. Pennington, *3D MR microscopy with resolution 3.7μm by 3.3μm by 3.3μm.* Journal of Magnetic Resonance, 2002. **158**(1): p. 178-182.
45. Degen, C.L., et al., *Nanoscale magnetic resonance imaging.* Proceedings of the National Academy of Sciences, 2009. **106**(5): p. 1313-1317.
46. Vasyukov, D., et al., *A scanning superconducting quantum interference device with single electron spin sensitivity.* Nature Nanotechnology, 2013. **8**: p. 639.
47. Ledbetter, M.P., et al., *Zero-field remote detection of NMR with a microfabricated atomic magnetometer*. Proceedings of the National Academy of Sciences, 2008. **105**(7): p. 2286-2290.
48. Sushkov, A.O., et al., *Magnetic Resonance Detection of Individual Proton Spins Using Quantum Reporters.* Physical Review Letters, 2014. **113**(19).
49. Schweiger, A. and G. Jeschke, *Principles of Pulse Electron Paramagnetic Resonance*. 2001: Oxford University Press.
50. Kalish, R., et al., *Nitrogen doping of diamond by ion implantation.* Diamond and Related Materials, 1997. **6**(2): p. 516-520.
51. Santori, C., et al., *Vertical distribution of nitrogen-vacancy centers in diamond formed by ion implantation and annealing.* Physical Review B, 2009. **79**(12): p. 125313.
52. Ziegler, J.F., J.P. Biersack, and M.D. Ziegler, *SRIM, the Stopping and Range of Ions in Matter*. 2008: SRIM Company.
53. Pezzagna, S., et al., *Creation efficiency of nitrogen-vacancy centres in diamond.* New Journal of Physics, 2010. **12**(6): p. 065017.
54. Mamin, H.J., M.H. Sherwood, and D. Rugar, *Detecting external electron spins using nitrogen-vacancy centers.* Physical Review B, 2012. **86**(19): p. 195422.
55. Ohno, K., et al., *Engineering shallow spins in diamond with nitrogen delta-doping.* Applied Physics Letters, 2012. **101**(8): p. 082413.
56. Naydenov, B., et al., *Increasing the coherence time of single electron spins in diamond by high temperature annealing.* Applied Physics Letters, 2010. **97**(24): p. 242511.
57. Yamamoto, T., et al., *Extending spin coherence times of diamond qubits by high-temperature annealing.* Physical Review B, 2013. **88**(7): p. 075206.
58. Acosta, V.M., et al., *Temperature Dependence of the Nitrogen-Vacancy Magnetic Resonance in Diamond.* Physical Review Letters, 2010. **104**(7): p. 070801.
59. Nusran, N., *Doctoral Dissertation: Application of phase estimation algorithms to improve diamond spin magnetometry*. 2014.

60. Oort, E.v., N.B. Manson, and M. Glasbeek, *Optically detected spin coherence of the diamond N-V centre in its triplet ground state.* Journal of Physics C: Solid State Physics, 1988. **21**(23): p. 4385.
61. Manson, N.B. and J.P. Harrison, *Photo-ionization of the nitrogen-vacancy center in diamond.* Diamond and Related Materials, 2005. **14**(10): p. 1705-1710.
62. Hauf, M.V., et al., *Chemical control of the charge state of nitrogen-vacancy centers in diamond.* Physical Review B, 2011. **83**(8): p. 081304.
63. Aslam, N., et al., *Photo-induced ionization dynamics of the nitrogen vacancy defect in diamond investigated by single-shot charge state detection.* New Journal of Physics, 2013. **15**(1): p. 013064.
64. Dhomkar, S., et al., *Long-term data storage in diamond.* Science Advances, 2016. **2**(10): p. e1600911.
65. He, X.-F., N.B. Manson, and P.T.H. Fisk, *Paramagnetic resonance of photoexcited N-V defects in diamond. II. Hyperfine interaction with the $^{14}\mathrm{N}$ nucleus.* Physical Review B, 1993. **47**(14): p. 8816-8822.
66. Doherty, M.W., et al., *The negatively charged nitrogen-vacancy centre in diamond: the electronic solution.* New Journal of Physics, 2011. **13**(2): p. 025019.
67. Ji, P., *Doctoral Dissertation: Towards Quantum Nanomechanics with a Trapped Diamond Crystal Coupled to an Electronic Spin Qubit*. 2018.
68. Robert, H.W., *Confocal optical microscopy.* Reports on Progress in Physics, 1996. **59**(3): p. 427.
69. Robledo, L., et al., *High-fidelity projective read-out of a solid-state spin quantum register.* Nature, 2011. **477**(7366): p. 574-8.
70. Dréau, A., et al., *Avoiding power broadening in optically detected magnetic resonance of single NV defects for enhanced dc magnetic field sensitivity.* Physical Review B, 2011. **84**(19): p. 195204.
71. Levitt, M.H., *Spin Dynamics: Basics of Nuclear Magnetic Resonance*. 2008: Wiley.
72. Zhang, K., et al., *Experimental limits on the fidelity of adiabatic geometric phase gates in a single solid-state spin qubit.* New Journal of Physics, 2016. **18**: p. 053029.
73. Zanardi, P. and M. Rasetti, *Holonomic quantum computation.* Physics Letters A, 1999. **264**(2): p. 94-99.
74. Jones, J.A., et al., *Geometric quantum computation using nuclear magnetic resonance.* Nature, 2000. **403**: p. 869.
75. Zhu, S.L. and Z.D. Wang, *Implementation of universal quantum gates based on nonadiabatic geometric phases.* Physical Review Letters, 2002. **89**(9): p. 097902.
76. Leek, P.J., et al., *Observation of Berry's phase in a solid-state qubit.* Science, 2007. **318**(5858): p. 1889-1892.
77. Sjöqvist, E., et al., *Non-adiabatic holonomic quantum computation.* New Journal of Physics, 2012. **14**: p. 103035.
78. Abdumalikov, A.A., et al., *Experimental realization of non-Abelian non-adiabatic geometric gates.* Nature, 2013. **496**(7446): p. 482-485.
79. Arroyo-Camejo, S., et al., *Room temperature high-fidelity holonomic single-qubit gate on a solid-state spin.* Nature Communications, 2014. **5**: p. 4870.
80. Zu, C., et al., *Experimental realization of universal geometric quantum gates with solid-state spins.* Nature, 2014. **514**(7520): p. 72-75.
81. Anandan, J., *The Geometric Phase.* Nature, 1992. **360**(6402): p. 307-313.

82. Berry, M.V., *Quantal phase factors accompanying adiabatic changes.* Proceedings of the Royal Society of London. A. Mathematical and Physical Sciences, 1984. **392**(1802): p. 45-57.
83. Aharonov, Y. and J. Anandan, *Phase change during a cyclic quantum evolution.* Physical Review Letters, 1987. **58**(16): p. 1593-1596.
84. Duan, L.-M., J.I. Cirac, and P. Zoller, *Geometric Manipulation of Trapped Ions for Quantum Computation.* Science, 2001. **292**(5522): p. 1695-1697.
85. Childress, L., et al., *Coherent dynamics of coupled electron and nuclear spin qubits in diamond.* Science, 2006. **314**(5797): p. 281-285.
86. Ledbetter, M.P., et al., *Gyroscopes based on nitrogen-vacancy centers in diamond.* Physical Review A, 2012. **86**(5): p. 052116.
87. Yale, C.G., et al., *Optical manipulation of the Berry phase in a solid-state spin qubit.* Nature Photonics, 2016. **10**(3): p. 184-189.
88. Samuel, J. and R. Bhandari, *General Setting for Berry's Phase.* Physical Review Letters, 1988. **60**(23): p. 2339-2342.
89. De Chiara, G. and G.M. Palma, *Berry phase for a spin 1/2 particle in a classical fluctuating field.* Physical Review Letters, 2003. **91**(9): p. 090404.
90. Massar, S. and S. Popescu, *Optimal Extraction of Information from Finite Quantum Ensembles.* Physical Review Letters, 1995. **74**(8): p. 1259-1263.
91. J W Zwanziger, a. M Koenig, and A. Pines, *Berry's Phase.* Annual Review of Physical Chemistry, 1990. **41**(1): p. 601-646.
92. Anandan, J., *Non-Adiabatic Non-Abelian Geometric Phase.* Physics Letters A, 1988. **133**(4-5): p. 171-175.
93. Pancharatnam, S., *Generalized theory of interference, and its applications.* Proceedings of the Indian Academy of Sciences - Section A, 1956. **44**(5): p. 247-262.
94. Xiao, D., M.C. Chang, and Q. Niu, *Berry phase effects on electronic properties.* Reviews of Modern Physics, 2010. **82**(3): p. 1959-2007.
95. Berger, S., et al., *Geometric phases in superconducting qubits beyond the two-level approximation.* Physical Review B, 2012. **85**(22): p. 220502.
96. Berger, S., et al., *Exploring the effect of noise on the Berry phase.* Physical Review A, 2013. **87**(6): p. 060303.
97. Johansson, M., et al., *Robustness of nonadiabatic holonomic gates.* Physical Review A, 2012. **86**(6): p. 062322.
98. Xing, R., et al., *Enhanced phase estimation by implementing dynamical decoupling in a multi-pass quantum metrology protocol.* EPL (Europhysics Letters), 2011. **95**(6): p. 60005.
99. Chernobrod, B.M. and G.P. Berman, *Spin microscope based on optically detected magnetic resonance.* Journal of Applied Physics, 2005. **97**(1): p. 014903.
100. Grinolds, M.S., et al., *Nanoscale magnetic imaging of a single electron spin under ambient conditions.* Nature Physics, 2013. **9**: p. 215.
101. Pelliccione, M., et al., *Scanned probe imaging of nanoscale magnetism at cryogenic temperatures with a single-spin quantum sensor.* Nature Nanotechnology, 2016. **11**: p. 700.
102. Appel, P., et al., *Fabrication of all diamond scanning probes for nanoscale magnetometry.* Review of Scientific Instruments, 2016. **87**(6): p. 063703.
103. Edwards, H., et al., *Fast, high-resolution atomic force microscopy using a quartz tuning fork as actuator and sensor.* Journal of Applied Physics, 1997. **82**(3): p. 980-984.

104. Hong, S., *Unpublished material: Fabrication of scanning diamond nanopillar devices.* 2014.
105. Zhou, T.X., R.J. Stöhr, and A. Yacoby, *Scanning diamond NV center probes compatible with conventional AFM technology.* Applied Physics Letters, 2017. **111**(16): p. 163106.
106. Hausmann, B.J.M., et al., *Fabrication of diamond nanowires for quantum information processing applications.* Diamond and Related Materials, 2010. **19**(5): p. 621-629.
107. *MadPLL Manual v4*, in *User Manual from Mad City Labs Inc.*
108. Akiyama, T., et al., *Symmetrically arranged quartz tuning fork with soft cantilever for intermittent contact mode atomic force microscopy.* Review of Scientific Instruments, 2003. **74**(1): p. 112-117.
109. Friedt, J.-M. and É. Carry, *Introduction to the quartz tuning fork.* American Journal of Physics, 2007. **75**(5): p. 415-422.
110. Maze, J.R., et al., *Nanoscale magnetic sensing with an individual electronic spin in diamond.* Nature, 2008. **455**(7213): p. 644-647.
111. Stacey, A., et al., *Depletion of nitrogen-vacancy color centers in diamond via hydrogen passivation.* Applied Physics Letters, 2012. **100**(7): p. 071902.
112. Suter, D. and G.A. Álvarez, *Colloquium: Protecting quantum information against environmental noise.* Reviews of Modern Physics, 2016. **88**(4): p. 041001.
113. Loretz, M., et al., *Nanoscale nuclear magnetic resonance with a 1.9-nm-deep nitrogen-vacancy sensor.* Applied Physics Letters, 2014. **104**(3): p. 033102.
114. Staudacher, T., et al., *Nuclear Magnetic Resonance Spectroscopy on a (5-Nanometer)(3) Sample Volume.* Science, 2013. **339**(6119): p. 561-563.
115. Lovchinsky, I., et al., *Magnetic resonance spectroscopy of an atomically thin material using a single-spin qubit.* Science, 2017. **355**(6324): p. 503-507.
116. Haberle, T., et al., *Nanoscale nuclear magnetic imaging with chemical contrast.* Nature Nanotechnology, 2015. **10**(2): p. 125-128.
117. Grotz, B., et al., *Sensing external spins with nitrogen-vacancy diamond.* New Journal of Physics, 2011. **13**(5): p. 055004.
118. Grinolds, M.S., et al., *Subnanometre resolution in three-dimensional magnetic resonance imaging of individual dark spins.* Nature Nanotechnology, 2014. **9**(4): p. 279-284.
119. Shi, F.Z., et al., *Single-protein spin resonance spectroscopy under ambient conditions.* Science, 2015. **347**(6226): p. 1135-1138.
120. Mamin, H.J., et al., *Nanoscale Nuclear Magnetic Resonance with a Nitrogen-Vacancy Spin Sensor.* Science, 2013. **339**(6119): p. 557-560.
121. Lovchinsky, I., et al., *APPLIED PHYSICS Nuclear magnetic resonance detection and spectroscopy of single proteins using quantum logic.* Science, 2016. **351**(6275): p. 836-841.
122. Ohashi, K., et al., *Negatively Charged Nitrogen-Vacancy Centers in a 5 nm Thin 12C Diamond Film.* Nano Letters, 2013. **13**(10): p. 4733-4738.
123. Yang, Z., et al., *Chapter Seventeen - Cu2+ as an ESR Probe of Protein Structure and Function*, in *Methods in Enzymology*, P.Z. Qin and K. Warncke, Editors. 2015, Academic Press. p. 459-481.
124. Cunningham, T.F., et al., *The Double-Histidine Cu2+-Binding Motif: A Highly Rigid, Site-Specific Spin Probe for Electron Spin Resonance Distance Measurements.* Angewandte Chemie International Edition, 2015. **54**(21): p. 6330-6334.

125. Ji, M., S. Ruthstein, and S. Saxena, *Paramagnetic Metal Ions in Pulsed ESR Distance Distribution Measurements.* Accounts of Chemical Research, 2014. **47**(2): p. 688-695.
126. Stoll, S. and A. Schweiger, *EasySpin, a comprehensive software package for spectral simulation and analysis in EPR.* Journal of Magnetic Resonance, 2006. **178**(1): p. 42-55.
127. Jensen, K., et al., *Light narrowing of magnetic resonances in ensembles of nitrogen-vacancy centers in diamond.* Physical Review B, 2013. **87**(1): p. 014115.
128. Jacques, V., et al., *Dynamic Polarization of Single Nuclear Spins by Optical Pumping of Nitrogen-Vacancy Color Centers in Diamond at Room Temperature.* Physical Review Letters, 2009. **102**(5): p. 057403.
129. Lee, T.H., *Planar Microwave Engineering: A Practical Guide to Theory, Measurement, and Circuits*. 2004: Cambridge University Press.
130. Veyres, C. and V. Fouad Hanna, *Extension of the application of conformal mapping techniques to coplanar lines with finite dimensions.* International Journal of Electronics, 1980. **48**(1): p. 47-56.
131. Rabeau, J.R., et al., *Implantation of labelled single nitrogen vacancy centers in diamond using N15.* Applied Physics Letters, 2006. **88**(2): p. 023113.
132. Fuchs, G.D., et al., *Excited-State Spectroscopy Using Single Spin Manipulation in Diamond.* Physical Review Letters, 2008. **101**(11): p. 117601.
133. Felton, S., et al., *Hyperfine interaction in the ground state of the negatively charged nitrogen vacancy center in diamond.* Physical Review B, 2009. **79**(7): p. 075203.